Alma Mater Studiorum
Università di Bologna
in coparticipation with
Universidad de Buenos Aires

Doctor of Philosophy

Scuola di dottorato in Ingegneria Industriale

MECCANICA E SCIENZE AVANZATE DELL'INGEGNERIA:
PROG N.4 "MECCANICA DEI MATERIALI E PROCESSI TECNOLOGICI"

Ciclo XXV

Settore Concorsuale di Afferenza: 09/A3

Settore Scientifico Disciplinare: ING/ING 14

COMPOSITE MATERIALS DESIGN, MANUFACTURE AND EVALUATION

Candidate:
Ezequiel Poodts

Tutor:
Prof. Giangiacomo Minak

Co-tutors:
Prof. Anibal Cofone
Prof. Analía Vazquez

Final Exam Year 2013

...dedicated to my family and friends
Special thanks to the unofficial co-tutors Gianluca Monti from Studio Pedrini s.r.l. and Enrico Dolcini from Riba Composites s.r.l. and to my co-authors and colleagues Riccardo Pancciroli, Roberto Palazzetti, Daniele Ghelli, Andrea Zucchelli, Loris Giorgini, Laura Mazzocchetti, Lorenzo Donati, Cesar Belinco, German Kokubu and the rest of the people who helped me during these three years...

The more you look, the more you see

Contents

List of Figures

List of Tables

Abstract

Fibre reinforced plastic are composite materials composed by thin fibres with high mechanical properties, made to work together with a cohesive plastic matrix. The huge advantages of fibre reinforced plastics over traditional materials are their high specific mechanical properties i.e. high stiffness and strength to weight ratios. This kind of composite materials is the most disruptive innovation in the structural materials field seen in recent years and the areas of potential application are still many.
However, there are few aspects which limit their growth: on the one hand the information available about their properties and long term behaviour is still scarce, especially if compared with traditional materials for which there has been developed an extended database through years of use and research.
On the other hand, the technologies of production are still not as developed as the ones available to form plastics, metals and other traditional materials.
A third aspect is that the new properties presented by these materials e.g. their anisotropy, difficult the design of components.
This thesis will provide several case-studies with advancements regarding the three limitations mentioned.
In particular, the long term mechanical properties have been studied through an experimental analysis of the impact of seawater on GFRP. Regarding production methods, the pre-impregnated cured in autoclave process was considered: a rapid tooling method to produce moulds will be presented, and a study about the production of thick components. Also, two liquid composite moulding methods will be presented, with a case-study regarding a large component with sandwich structure that was produced with the Vacuum-Assisted-Resin-Infusion method, and a case-study regarding a thick con-rod beam that was produced with the Resin-Transfer-Moulding process. The final case-study will analyse the loads acting during the use of a particular

sportive component, made with FRP layers and a sandwich structure, practical design rules will be provided.
The main results of this thesis are:

- A detailed analysis of the degradation that sea-water causes on the fatigue and quasi-static properties of GFRP with two different resins i.e. Polyester and Vinylester.
- A method based on a simple linear regression to obtain the parameters of the Kamal-Sourour model of the Cure-Kinetics of thermosetting resin.
- A rapid-tooling method to produce moulds apt for autoclave forming of prepregs.
- A detailed analysis of the differences in terms of ageing and cure kinetics of two prepregs made with the same resin but different production method i.e. solvent impregnation and hot melt.
- A procedure to obtain the permeability curve as a function of the fibre volume ($K - V_f$) with a reduced number of tests.
- A method to deal with sandwich structures where perforated cores are used in a FE analysis of the filling process in a LCM process such as VARI.
- A method to reduce porosity in composite parts produced with the RTM process.
- An analysis of the impact that different tackifier products used on LCM method can produce on the mechanical properties of composite parts.
- Practical formulas for the damage-tolerant design of sandwich structured wakeboards.

Sommario

Le plastiche fibrorinforzate (FRP) sono una categoria di materiali compositi nei quali fibre con alte proprietà meccaniche sono unite ad una matrice plastica coesiva che ha lo scopo di trasferire i carichi meccanici alle fibre stesse.
Il grande vantaggio dei FRP sui materiali tradizionali consiste nelle le sue alte proprietà meccaniche specifiche, ovvero alto rapporti rigidezza-peso e resistenza-peso. Questa gamma di materiali compositi è l'innovazione più importante vista negli ultimi anni nel campo dei materiali strutturali e le aree di potenziale applicazione sono ancora vaste.
Tuttavia ci sono alcuni fattori che limitano la sua diffusione: da una parte le informazioni disponibili riguardo alle proprietà meccaniche ed al comportamento a lungo termine sono ancora scarse, specialmente se si li paragona ai materiali tradizionali dove esiste una base di dati sviluppata attraverso anni di utilizzo e ricerca.
Dall'altra, le tecnologie produttive non sono ancora abbastanza sviluppate come quelle disponibili per la plastica, i metalli e altri materiali tradizionali.
Un terzo fattore è che le nuove proprietà che questi materiali presentano per esempio la loro anisotropia, rendono complesso il processo di progettazione di componenti. In questa tesi verranno mostrati vari casi di studio con avanzamenti riguardo ai tre aspetti menzionati.
In particolare, le proprietà a lungo termine sono state studiate attraverso un analisi sperimentale sull'impatto dell'acqua di mare nei compositi rinforzati mediante fibra di vetro. Riguardo ai metodi produttivi, è stato considerato il processo di formatura in autoclave di pre-impregnati: si presenterà un metodo per produrre gli stampi in maniera veloce e uno studio della produzione di parti a forte spessore. Inoltre, due metodi di stampaggio liquido dei compositi (LCM) saranno presentati con un caso di studio riguardo alla produzione di un componente nautico di grandi dimensioni con il metodo d'infusione

(VARI) e un altro caso di studio dove si analizzeranno diversi aspetti della produzione di una biella con il metodo di stampaggio per trasferimento di resina (RTM). L'ultimo caso di studio che sarà presentato analizzerà gli sforzi presenti durante l'utilizzo di un componente sportivo fatto con lamine di FRP e una struttura sandwich, per la quale si daranno regole pratiche di progettazione. I risultati principali di questa tesi sono:

- Un' analisi dettagliata della degradazione che l'acqua di mare causa nelle proprietà meccaniche quasi-statiche e di fatica dei compositi rinforzati mediante fibra di vetro con due resine diverse, poliestere e vinilestere.
- Un metodo per ottener i valori caratteristici del modello Kamal-Sourour di cinetica di cura di resine termoindurenti, basato su una regressione lineare semplice.
- Un metodo per la produzione in maniera veloce di stampi adatti formatura di compositi in autoclave
- Un'analisi dettagliata delle differenze in termini di invecchiamento e cinetica di cura di due materiali pre-impregnati fatti con la stessa resina però attraverso due processi di produzione diversi, ovvero impregnazione con calore (hot melt) e impregnazione con solventi.
- Un processo per l'ottenimento della curva di permeabilità in funzione del volume di fibra ($K - V_f$) attraverso un numero ridotto di prove sperimentali.
- Un metodo per risolvere strutture sandwich con anima perforata in un'analisi ad elementi finiti del processo di riempimento nel metodo di produzione di infusione (VARI).
- Un metodo per ridurre la porosità dei compositi prodotti con il processo di stampaggio per trasferimento di resina (RTM).
- Un'analisi del impatto che diversi prodotti normalmente utilizzati durante i processi di stampaggio liquido di compositi (LCM) possono avere sulle proprietà meccaniche dei pezzi finiti.
- Formule pratiche per la progettazione di wakeboard con strutture sandwich

Resumen

Los plásticos reforzados con fibra (FRP) son una categoría de materiales compuestos en los cuales fibras con altas propiedades mecánicas son unidas a una matriz plástica cohesiva que tiene como función transferir las cargas mecánicas a las fibras mismas. Las grandes ventajas de los FRP sobre los materiales tradicionales son sus altas propiedades mecánicas específicas: altos ratios de rigidez-peso y resistencia-peso. Esta clase de materiales compuestos es la innovación más importante que se ha visto en los últimos años en el campo de los materiales estructurales, y las áreas de aplicación potencial son aún vastas.

Sin embargo hay algunos factores que limitan su difusión: por un lado la información disponible acerca de sus propiedades mecánicas y a su comportamiento a largo plazo es todavía escarza, especialmente si se los compara con los materiales tradicionales en donde existe una base de datos desarrollada a partir de años de utilizo e investigación.

Por otro lado, las tecnologías de producción no están aun suficientemente desarrolladas como las disponibles para plásticos, metales y otros materiales tradicionales. Un tercer aspecto es que las nuevas propiedades que presentan los materiales compuestos, por ejemplo su anisotropía, dificultan el proceso de diseño de componentes.

En esta tesis se mostrarán varios casos de estudio con avances respecto a los tres aspectos mencionados.

En particular, las propiedades a largo plazo fueron estudiadas a través de un análisis experimental acerca del impacto del agua de mar en compuestos a base de fibra de vidrio. Respecto a los métodos productivos, el proceso de preimpregnado curado en autoclave fue considerado: se presentará un método para producir moldes de manera rápida y un estudio de la producción de partes con grande espesor. Además, dos métodos de moldeo líquido de com-

puestos (LCM) serán presentados con un caso de estudio enfocado en la producción de un componte náutico de grandes dimensiones con el método de infusión (VARI) y otro caso de estudio donde se estudiará la producción de una biela con el método de moldeo por transferencia de resina (RTM). El último caso de estudio que será presentado analizará los esfuerzos presentes durante el uso de un componente deportivo hecho con láminas FRP y una estructura sándwich, para el cual se darán reglas prácticas de diseño.
Los resultados principales de esta tesis son:

- Un análisis detallado de la degradación que el agua de mar causa en las propiedades mecánicas cuasi-estáticas y de fatiga de compuestos a base de fibra de vidrio con dos resinas distintas, polyester y vinylester.
- Un método para obtener los valores característicos del modelo Kamal-Souror de cinética de cura de resinas termoestables, basado en una regresión linear simple.
- Un método de producción rápida de herramental apto para realizar moldes para fabricar compuestos en autoclave.
- Un análisis detallado de las diferencias en términos de envejecimiento y cinética de cura de dos materiales pre-impregnados hechos con la misma resina pero a través de dos procesos de producción distintos: impregnación con calor (Hot melt) e impregnación con solventes.
- Un procedimiento para la obtención de la curva de permeabilidad en función del volumen de fibra ($K - V_f$) a través de un número reducido de ensayos experimentales.
- Un método para resolver estructuras sándwich con alma perforada en un análisis a elementos finitos del proceso de llenado en el método productivo de infusión (VARI).
- Un método para reducir la porosidad de las partes producidas con el proceso productivo de moldeo por transferencia de resina (RTM).
- Un análisis del impacto que diferentes productos normalmente usados durante los procesos de moldeo liquido de compuestos (LCM) puede tener en las propiedades mecánicas de los componentes finales.
- Formulas prácticas para el diseño de wakeboards con estructura sándwich

Introduction

Composite materials are those composed by at least two different constituent materials, which can be identified macroscopically in the final structure. The result of this combination is a new material with superior performance with respect to each of the composing ones taken separately.

Based on this definition, composite materials have existed for thousands of years: in this category it is possible to include ancient materials such as adobe (also known as Wattle and daub), a combination of mud and straw used by the native people in America and other parts of the world to construct their houses more than 6000 years ago. More recent, although more than one century old, is the reinforced concrete in which the steel bars, with good tensile resistance, are combined with concrete, which provides compression resistance, cohesion and corrosion protection to the steel.

The concept of composite materials can be found in nature itself; a combination of cellulose fibres, which play the role of reinforcement, and lignin, which is the matrix of the composite material used by nature to create structures that can reach hundreds of meters in height: the trees. This is possible through an optimization of the properties of the material: wood is anisotropic, it has the cellulose fibres oriented to reinforce the tree in the direction where it is more convenient, according to the loads it has to bear. The anisotropy allows an optimized resistance and this translates in weight savings, the situation is different for common materials which are isotropic i.e. the properties are equal in every direction.

The concept of wood, added to the development of new fibres and plastics, has given birth to a new category of composite materials: the Fibre Reinforce Plastic (FRP), including carbon, glass, aramid and other fibres as reinforcements, and a wide variety of plastics which can play the matrix part, such as epoxy, polyester, vinylester, BMI and others, including also thermoplastics.

These materials have been engineered and applied to make final products about 30 years ago and are in continuous growth.
The huge advantages of fibre reinforced plastics over traditional materials are their high specific mechanical properties i.e. High stiffness to weight ratio and high strength to weight ratio. Table 1 shows the properties of various types of FRP and metals, notice that metals show a barely constant value of specific stiffness, while the value for FRP can be considerably higher. Moreover they show other advantages such as high fatigue resistance, low coefficient of thermal expansion, corrosion resistance, transparent to X-rays, and others.
These materials were first used to make components where the performance is more important than the cost, such as aerospace (e.g. satellites) and competition (e.g. Formula 1 cars and America's cup sails) structures. The good results obtained allowed their use in other components such as sport goods (e.g. skis and golf shafts), transportation structures (e.g. high speed trains), parts for industrial applications (e.g. rollers or automatic machine parts) and new markets such as structures for the renewable energy production (e.g. wind blades).
Composite materials are the most disruptive innovation in the structural

Table 1: Comparison of properties for different materials

			Composite Materials									Metals			
	Symbol	Units	Std CF Fabric	HMCF Fabric	E glass Fabric	Kevlar Fabric	Std CF UD	HMCF UD	M55 UD	E glass UD	Kevlar UD	Steel S97	Aluminium 7075-T6	Titanium α/β alloy	Magnesium AM100A-T5
Young's Modulus 0°	E1	GPa	72,4	85	25	30	135	175	300	40	75	207	72	114	44
Young's Modulus 90°	E2	GPa	72,4	85	25	30	10	8	12	8	6	207	72	114	44
Ult. Tensile Strength 0°	Xt	MPa	600	350	440	480	1500	1000	1600	1000	1300	990	572	1060	150
Ult. Tensile Strength 90°	Yt	MPa	600	350	440	480	50	40	50	30	30	990	572	1060	150
Density	d	g/cc	1,6	1,6	1,9	1,4	1,6	1,6	1,65	1,9	1,4	8	2,8	4,54	1,74
Specific stiffness 0°	E1/d	Gpa/(g/cc)	45	53	13	21	84	109	182	21	54	26	26	25	25
Specific stiffness 90°	E2/d	Gpa/(g/cc)	45	53	13	21	6	5	7	4	4	26	26	25	25
Specific Strength 0°	Xt/d	Mpa/(g/cc)	375	219	232	343	938	625	970	526	929	124	204	233	86
Specific Strength 90°	Xt/d	Mpa/(g/cc)	375	219	232	343	31	25	30	16	21	124	204	233	86

Values obtained from http://www.matweb.com and http://www.performance-composites.com

materials field seen in recent years and the areas of potential application are still many. However, there are few aspects of these which limit their growth: on the one hand the information available about their properties and long term behaviour is still low comparing with the data developed through years

of experience and research focused on traditional materials. On the other hand the technologies of production are still not as developed as the ones available to form plastics, metals and other traditional materials. A third aspect is that the anisotropy of these materials makes the design of components more difficult with respect to traditional materials, which are isotropic. This requires specialized engineers with high technical background and experience on design and production with FRP.

The work done during the doctorate covers some various aspects of composites materials; this thesis will provide several studies with advancements regarding the three limitations mentioned.

The thesis starts with two sections where the properties of composite materials are studied: the first of these will study the degradation that seawater causes on the mechanical properties of Glass Fibre Reinforced Plastic (GFRP), with two common resin systems, i.e. Polyester and Vinylester. The section will report the results of quasi-static and vibration tests at different sea-water exposure times, and fatigue tests in dry and wet environments of unexposed specimens and specimens aged in sea water for 22-weeks. The second section will focus on the resin properties, specifically the cure kinetics, describing a case study which goes through the characterization process of an epoxy resin to construct the model first proposed by Kamal-Sourour and it presents a novel method to calculate the parameters. The method will be applied for the characterization of the resin used in studies presented later on this thesis.

The second and third chapters focus on technological aspects. Section one of chapter one will go through two works where the prepreg cured in autoclave method is involved. Prepreg cured in autoclave is the most reliable and widespread technology to produce composite materials; it is very flexible and versatile technology, where usually open composite moulds are used which are less expensive than closed metallic ones. The drawback of this method is the low potential to automation, the high requirements of manual work and the need of long production cycles. The first of the works presented in this section involves another disruptive technology: Rapid prototyping, and with this it empowers the advantages of the autoclave forming process. The work proposes a method to accelerate the time-to-market of composite products,

this is achieved by passing through the rapid prototyping technology to make the moulds, the method can be classified as an indirect rapid tooling technique. This method came much appreciated by two end markets of composite products: the race sector, specially motorcycle race because it has traditionally relied on prepreg cured in autoclave technology to produce composite parts, but many times it is intended to improve the design of the parts in a short time e.g. from one race to the other. Normal techniques make the fast-design-improvement difficult to achieve; and the mould production process is the bottleneck to arrive to the final part. With the proposed method it was possible to accelerate the process and get the parts done in time.
The second section of chapter two regards the production in autoclave of thick components, made by stacking several layers of preimpregnated fibres. The increased thickness provides new technological difficulties, not only because the production times are extended, but also because the polymerization of a big mass of resin has to be performed, and this reaction being exothermic can create overshooting temperature, which can cause the degradation of the resin and thus compromise the mechanical performance of the component. In the work presented the industrial production of a thick part ($\approx$ 35 mm) obtained by Hand-Lay-Up of two commercial prepregs and intended for primary structural application is considered. Prepregs are made of either unidirectionally aligned fibres, PP-UD, or 2x2 twill woven fabric, PP-T2. While the resin is exactly the same, the prepreg production technology is different, namely hot melt and solvent impregnation respectively. The study shows that prepregs age differently in the time span required for the process work up. Moreover, simulation of the independent curing process of each raw material, with reaction model of cure kinetics constructed with the methodology shown chapter one, shows unexpected differences both in the time scale (PP-UD reacts faster than PP-T2) and in the extent of reaction (PP-UD develops a higher amount of heat than PP-T2). The outlined differences require a particular care in the design of the curing cycle for production of thick composites where sequences of different prepregs alternate with no necessarily regular pattern, in order to reduce overheating, and to promote equal reaction of the two components without inducing too much residual stress between adjacent layers. The work shows that the experimental verification of raw materials and curing condi-

tions might help identifying unforeseen critical situations and avoiding the lack of performance in the final composite materials.
The third chapter focus on Liquid Composite Moulding (LCM) technologies, where dry fibres are used instead of the pre-impregnated ones. LCM processes include the draping of the fibres on the mould, the wetting of these by resin injection before starting with the curing stage, and the unmoulding of the part. These techniques show many advantages over other technologies. When compared to prepreg hand layup and autoclave curing process, the advantages are: direct economical savings because dry fabrics and raw resin are less expensive than prepreg, since an echelon in the supply chain is skipped. Logistic savings, because raw materials don't need to be stocked inside a low temperature cell, unlike prepregs. Productivity advantages since process times can be reduced, not only because there is no need of hand lay-up, but also because more reactive resins can be used. In general Prepreg cured in autoclave is considered a low scale technology ($10^1 - 10^2$ parts/year), while LCM can cover also the medium scale production ($10^2 - 10^5$ parts/year). Also improvements in terms of mechanical properties can be achieved, since with LCM it is possible to work with 3D woven preforms which can include fibres oriented in any direction. Instead, when using prepreg layup it is not possible to position fibres oriented in the perpendicular direction with respect to the stacking sequence.
The drawback of LCM technologies is that a new production variable needs to be considered: the optimization of the resin flow to properly wet all the fibres and avoid dry spots. For this purpose commercial packages were developed where numerical models were coded to predict the resin flow, such as PAM-RTM software which was used during the studies that lead to the present thesis.
The chapter presents two cases where two different LCM technologies are studied in each. The first of these (section one in chapter three) focus on the Vacuum Assisted Resin Infusion (VARI) process, which is a high performance and cost effective manufacturing technology, usually applied to produce large structures. In VARI an open mould is used, and the fibres are draped on top of it. A flexible membrane is then used to cover the whole, in order to create vacuum in the cavity containing the fibres, and then resin is injected at at-

mospheric pressure, the flow is driven by the pressure difference respect the points where the vacuum is applied. The study presented deals with the development and validation of the FE analysis of the injection process by means of the PAM-RTM code of a ship runway, through the definition of a standardized experiment for the characterization of the laminates to obtain reliable permeability data. Indeed the assessment of laminate permeability proprieties (K) during the process is the major concern for reliable FE application: a procedure to obtain these characteristic values with few experimental tests is presented starting initially with a classic characterization at constant fibre volume fraction (V_f) and then extending the approach for the construction of a $Pressure - V_f$ dependant curves. The tests were realized with carbon fibre fabrics, epoxy for infusion resin and perforated PVC core. Moreover the study provides an innovative approach for the computation of sandwich structures when perforated cores are used: the obtained data are finally applied with success for the validation of the simulation of the production phases of the ship runway characterized by the sandwich structure.
The second case study (section two in chapter three) deals with Resin Transfer Moulding (RTM) technology, in which a closed mould is used, thus more expensive respect VARI process in terms of initial expenses, although less disposable materials are needed which leads to reduced variable costs. Also, thanks to the use of a closed rigid mould, increased pressure difference between injection point and vents can be applied, and thus it is possible to design reduced production cycles. Moreover, the use of a closed mould allows controlling the surface quality for all the sides of the part, instead in VARI the quality for only one side of the part is under control.
The RTM section presents the case of a Carbon-fibre-reinforced-epoxy (CFRP) con-rod beam, to be used as part of a crane arm. Also in this case a thick composite part is considered (20 mm), as the second study of the second chapter, where it is explained that a normal autoclave curing cycle needs a redesign in order to avoid degradation of the mechanical properties of the finished component due to the heat generated during the polymerization of the plastic. The state of the art in these case would be to use a staged curing cycle, although this entails an increased production cost since a dedicated autoclave cycle is requiring.

The study will go through many aspects covering the design of a production method to use the RTM process, presenting the designed mould with incorporated heating mechanism, the simulation and real experience of both injection and curing phases, and mechanical and chemical tests of the final component and of specimens extracted from it, in comparison to the component made with the prepreg and autoclave method. As a result of this study the whole production cycle was substantially reduced in time and costs, to obtain a net shape con-rod beam which was compared with the one made in autoclave.
The fourth and last chapter will study the design of a particular component, made with FRP layers and a sandwich structure. It is the board used in a water sport named wakeboard. The objective of this work was to understand the failure mechanism and evaluate the maximum hydroelastic loads during the slamming phenomena of the wakeboard, in order to provide reliable design rules to follow during the design process. Several specimens were extracted from a real board and tested in three-point bending to investigate the major failure mechanisms. These data were later used in a parametric full-scale SPH numerical model investigation of the water-entry event.
The numerical results showed that, due to the fluid-structure interaction, there is a maximum deformation that the board cannot overreach even for very high impact energies. This limits the maximum impact stresses reached during the water entry of wakeboards. From these numerical results, mathematical relations between design variables are drawn by using analytical formulas based on classical sandwich theory. As result of this research, practical guidelines (formulas, tables and graphs) on the effects of total mass, initial impact velocity, board curvature and core and face strength and thickness are outlined to give reliable design rules.
In this way the thesis covers various aspects of FRP, with studies of its properties, of their production methods, and on the design aspects.

Chapter 1

Materiel Properties

1 DURABILITY OF COMPOSITES

IMPACT OF SEA-WATER ON THE QUASI STATIC AND FATIGUE FLEXURAL PROPERTIES OF GFRP

1.1 Introduction

Glass fibre reinforced plastic (GFRP) composite material is often utilized in marine applications for the construction of boats and ships [1, 2, 3, 4]. Over the years it has been replacing the use of wood and steel because of the advantages it provides in terms of mechanical properties, corrosion resistance, economicity and ease of processing [5]. In this application it is a usual procedure to protect the material with a layer of gel-coat [2], but contact between the structure and the water is continuous. In the search of understanding the long term properties of composite materials, it is important to understand the mechanisms and amount of degradation that water could cause on the mechanical properties of this material in order to consider them in the design phases, because the gel-coat could eventually break, leaving the GFRP directly exposed to the humid environment, and also because the material is used in other civil structures and applications where it is exposed to humidity (e.g. piping, trains, pedestrian bridges, storage vessels).

Many research studies have focused on the ageing and therefore degradation that a humid environment could cause on GFRP. It is a complex problem, since humidity could cause swelling or plasticisation of the matrix material, or degrade the fibre/matrix interface [2, 6, 7, 8]. All this may lead to a reduc-

tion of the mechanical properties. In the literature the problem is approached from different perspectives, e.g. focused on understanding the changes in the matrix material in terms of glass transition temperature (T_g)[9], or the storage modulus (E') and the damping properties ($Tan\ \delta$) [10, 11] or focused on improving the diffusion coefficient of the composite [5]. In structural applications it is essential to understand the changes in the material's strength that would be suffered by the composite during exposure to a humid environment [2, 3, 12].

Many studies can be found, which follow different experimental plans in terms of temperature and time of exposure and mechanical tests performed.

In reference [13], Glass polyester composite was immersed in distilled water at room temperature, leading to a 1% water uptake. Static and fatigue tests were performed and the authors reported a significant decrease in mechanical properties of conditioned specimens with respect to non-conditioned ones (almost 30% for flexural strength), but the number of specimens was low: fatigue lines were constructed with less than five points, which is definitively too few to give a conclusive result.

Reference [10] works with Glass fibre polyester specimens treated in seawater at $30°C$ for up to 120 days. The results showed an increase in $Tan\delta$ peak value of up to 29.6%, and a decrease in the Glass transition temperature ($134°C$ to $122°C$) and in tensile strength (up to 30%).

In reference [14] the authors worked with pipe shaped specimens of Glass/Polyester material. The immersion lasted up to 270 days in deionized water and at room temperature. They showed only slight differences in the stiffness of the pipes, and attributed this result to the small amount of water absorbed ($< 0.6\%$). This study also showed that water absorption was conditioned by the length of the tubes, meaning that the water was mainly absorbed through the cut edges.

In reference [8] the authors worked with Glass/polyester specimens fabricated by pultrusion technique; the conditioning was done at different temperatures, i.e. $20°C$, $60°C$, and inside an accelerated weathering apparatus that simulates weather conditions that include variations in temperature, humidity and UV light. They concluded that immersion and condensation environments affect the flexural properties of GFRP profiles (up to 20%),

and this effect is accelerated by increased temperatures. The degradation was explained to be mainly caused by physical phenomena such as plasticization of the polymeric matrix, since no appreciable chemical degradation was detected by the Fourier-transform infra-red analysis. This result is very important because it means that the degradation of the mechanical properties caused by water could be a reversible effect. The argument is addressed in reference [4], where creep, three point bending monotonic and fatigue tests were performed on many combinations of fibres and matrices, including E-Glass/Vinylester. The specimens were treated in three different conditions i.e. dry (non conditioned specimens), wet (treated for 120 hours in water at $95°C$) and Wet+Dry (treated like wet specimens and successively dehydrating them in air for 2 hours at $150°C$). E-Glass Vinylester specimens were saturated at 0.55% by-weight absorption. The results showed almost equal fatigue curves for dry and wet+dry for all the specimen families, different from the ones for wet specimens.

Glass and carbon as reinforcing materials, and polyester and vinylester resins as matrix systems were dealt with in reference [2]. The immersion was done in seawater at $30°C$ for over two years. The authors point out that polyester-based composites are less chemically stable in seawater than vinylester based composites; this is quite interesting because it shows that exposure to water can cause mass loss due to the susceptibility of the polyester resin to hydrolysis that resulted in the leaching out of ester species with hydroxyl end groups, and other low molecular weight organic species. Vinylester based composites show much lower chemical degradation than polyester matrix laminates. The maximum mass change in both species was close to 0.5%. Despite the superior chemical stability, the flexural properties of the vinylester based composites, obtained with quasi-static (Q-S) tests, were degraded to a similar extent to the properties of the polyester materials, about $10 - 20\%$, but it has to be pointed out that the data show high dispersion.

Reference [3] evaluated glass fiber reinforced plastic, with polyester, vinylester and phenolic resins as matrix systems. The specimens were immersed in $30°C$ seawater for up to 810 days, the immersion was done also with the specimens loaded under a set strain, although this changed the water uptake results only for the phenolic resin. The mass uptake always increased for all the

systems, reaching a maximum of 0.85% on Glass/polyester and 0.44% on Glass/vinylester specimens. The changes in the flexural modulus are limited, while differences greater than 15% are reported for flexural strength.
Many more references were found regarding composite materials with epoxy resin as the matrix system [9, 15, 16, 17, 18, 19]. On epoxy based composites the degradation mechanisms might be of the same nature, but the amount of water uptake and impact on mechanical properties could be quite different.
The present study provides data for Q-S, damping and fatigue tests of specimens at different sea-water exposure times. The main objective was to understand the degradation that sea-water causes on the fatigue properties of GFRP, the material used for the construction of boats. According to reference [20] the degradation of GFRP in sea-water on compressive, interlaminar and flexural strength is much more severe than in distilled water.
Specimens were manufactured by Stilplast s.r.l. using the vacuum assisted resin infusion (VARI) process. The laminate consisted of 8 layer E-Glass fibre (Mat 600 g/m^2) and two of the most common matrix materials used in boat applications, i.e. Vinylester and polyester resins [2]. The results showed degradation of the material in terms of ultimate stress in the case of Q-S loading, and no appreciable degradation on the fatigue loading case. Vibration testing demonstrated a stable flexural modulus during the water exposure period.

1.2 Methodology

In order to study ageing, fatigue tests were performed on non-conditioned and 22-week conditioned specimens. So as to have a deeper understanding of the material behaviour, fatigue tests were done in two different environments, i.e. water and air. Additionally, the water uptake of the materials was monitored by means of gravimetric technique. The elastic modulus was controlled by means of non-destructive vibration testing. Ultimate strength was tested every month by means of quasi-static loading tests, where the specimens were monitored for acoustic emission (AE), which also made it possible to detect the stress on the specimen when the first failure occurred during the test.

The sea water was artificially produced by adding specific quantitative of elements to distilled water according to reference [21] (Table 1.1). The temperature of the water was kept at $15°C$.

The specimens were cut from a panel made with the vacuum resin infusion

Table 1.1: Simplified artificial sea water composition

Species	Concentration (g/kg-soln)
Cl^- (Chloride)	19.4715
SO_4^{2-} (Sulfate)	2.7128
Na^+ (Sodium)	10.7848
Mg^{2+} (Magnesium)	1.2840
Ca^{2+} (Calcium)	0.4152
K^+ (Potassium)	0.3992

(VARI) technique, a method that will be studied on chapter 3. Two different types of resin were tested, Polyester (R.312 ISOFT-NPG) and Vinylester (R.912 VE), both provided by Leda Industrie S.r.l. A total of 100 specimens were obtained, 50 for each type of resin, the final dimensions of each test coupon were $80 \times 25 \times 4$ mm. Additionally, one larger specimen ($100 \times 300 \times 4$ mm) of each kind of resin was tested in a non-destructive test by making it vibrate; the vibration was monitored by means of two strain gauges that were attached to each panel and protected with silicon rubber.

Regarding the small specimens: twenty one of each type were kept outside water to obtain unaged reference data. From these; three were tested using the three-point bending (3PB) test on Q-S loading; nine were tested on fatigue loading while exposed to air with the same 3PB configuration; the other nine were also tested to fatigue with the same configuration, the difference was that these were tested while immersed in the artificial sea water. In this case the temperature of the water was not controlled at a constant value, room temperature was higher than $15°C$, thus it should have been more damaging for the material, further increasing the possible differences between treated and non-treated specimens.

The rest of the specimens were immersed in sea water and kept at $15°C$. 3PB Q-S tests were performed on two specimens after four, eight, twelve and twenty weeks of exposure, in order to monitor the evolution of the strength.

After completing twenty two weeks of exposure, the rest of the specimens were pulled out of the water and closed in individual sealed plastic bags to prevent them from drying before the start of the final fatigue testing campaign. Again, nine specimens were tested exposed to air and nine while immersed in artificial sea water. The last three specimens of each type of resin were tested at the end of the experimental campaign under Q-S loading.
On every test performed under Q-S loading, a sensor was applied to monitor the acoustic emissions; this technique made it easier to identify the moment at which the specimen suffers the first substantial damage. For this, the sentry function was constructed.
The sentry function is based on the idea that during the loading process a material is able to store strain energy and at the same time part of the stored energy can be released due to the internal failures. The AE events energy represents an important part of the released energy and can be used to weight the strain energy storing capability of the material. So the sentry function is used to compare the strain energy stored in the material (E_s) to the released energy in the form of acoustic energy (E_a) by their ratio (E_s/E_a). It has been proven that the best way to represent such a ratio is to consider its natural logarithm $Ln(E_s/E_a)$ [22, 23].
Depending on the material damaging process, the resulting sentry function can assume any combination of five trends [24]. An increasing trend of f represents the strain energy storing phases: the storing strain energy capability of the material overcame the released acoustic energy. When a significant internal material failure occurs, there is an instantaneous release of the stored energy that produces an AE event with high energy content. This fact is highlighted by the sudden drops of the sentry function. A constant behaviour of the sentry function is due to a progressive strain energy storing phase that is superimposed on an equivalent energy release due to material damage progression. A Bottom-Up trend indicates that a strengthening physical event induce an instantaneous energy storing capability into the material. Such a physical events can be related to phenomena like material hardening, crack-healing or crack bridging. The decreasing behaviour of the sentry function is related to the fact that the AE activity is greater than the material strain energy storing capability: the damage has reached a maximum limit and the

material has no more internal resources to sustain the external load.

Quasi-static tests with measure of Acoustic Emissions (AE)

The Q-S tests were performed by means of a universal machine with a 25 kN load cell on the 3PB configuration. The span between the fixed supports was 60 mm, the radius of each support was 7 mm. The loading nose had a radius of 10 mm and it was set to apply the load at 0.05 mm/sec.
Force-displacement was converted into Stress-strain to standardize the curves for all the specimens, this was done by applying Equations 1.1 and 1.2, where P is the force applied by the machine, L is the span, b and d are width and thickness of the specimen and D is the vertical deflection of the loading nose.

$$\sigma_f = \frac{3PL}{2bd^2} \tag{1.1}$$

$$\epsilon_f = \frac{6Dd}{L^2} \tag{1.2}$$

The tests were monitored for acoustic emissions, this permitted better interpretation of the stress-train curves. AEWin acoustic emission software and a Physical Acoustics Corporation (PAC) PCI-2 data acquisition system with a maximum sampling rate of 40 MHz were used to record AE events. A broadband, resonant-type, single-crystal piezoelectric transducer from PAC was used as the AE sensor. The sensor had a resonance frequency of 513.28 kHz and an optimum operating range of 100-750 kHz. The surface of the sensor was covered with grease in order to provide good acoustic coupling between the specimen and the sensor. The signal was detected by the sensor and enhanced by a 2/4/6-AST pre-amplifier. The gain selector of the pre-amplifier was set to 40 dB. The test sampling rate was 1MHz with 16 bits of resolution between 10 and 100 dB.
During the first tests, in order to clean the signal by the potential presence of noise coming from the tool and from the support system, two guardian

sensors had been applied respectively to the tool and to the frame of the specimen support (see Figure 1.1). Two main sources of noise can be generally identified during three point bending tests [25]: noise wave coming from the actuator (that in this case was connected to the tool) and noise produced during the sliding of two parts that can move one respect the other (such as the specimen that can have a small sliding at the cylindrical supports). The guardian sensor placed at the tool registered the noise coming from the actuator. The guardian sensor placed at the frame of the specimen support registered the noise eventually induced by the sliding of the specimen at the cylindrical support. The signals recorded by the sensor placed at the specimen had been cleaned by means of a time coordinating software that used the recording time of signals detected by the guardian sensors and the specimen sensor itself. Though it was seen that the cleaning process was not necessary for the current test configuration, the noise was negligible and the tests after the first three specimens were carried out with only the main AE sensor.
The sentry function was constructed for each specimen tested by evaluating Equation 1.3, where $E_s(x)$ is the cumulated strain energy and E_a is the cumulated acoustic energy released, both as a function of strain, as explained in reference [26]. This procedure made it possible to identify the exact point where the first significant failure occurred. An example can be seen in Figure 1.2.

$$f(\epsilon) = Ln\frac{E_s(\epsilon)}{E_a(\epsilon)} \tag{1.3}$$

As already mentioned, the tests were performed on three non-conditioned specimens, two specimens after four, eight, twelve and twenty weeks of exposure, and three specimens after the twenty two week exposure period.

Vibration tests

A non-destructive test was used in which the flexural modulus (E_f) of each material (Glass/Polyester and Glass/vinylester) was monitored indirectly by studying the free vibrational behaviour of one coupon for each kind of resin.

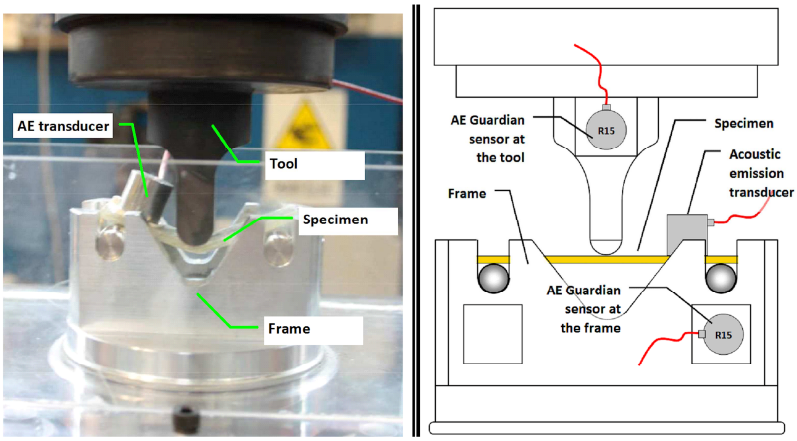

Figure 1.1: Three-point bending test configuration. On the left: Picture of the front side of the test set-up where the main AE transducer can be seen, positioned on the left side of the coupon and used on every Q-S test. On the right: Scheme of the back side of the complete set-up during the first tests, with the position of the AE guardian sensors used to clean the signal.

The specimens had dimensions of $100 \times 300 \times 4\ mm$. Since the cross section was constant and thin, it was possible to use the dynamic Euler-Bernoulli beam equation to analytically describe the vibrational behaviour of the samples. In accordance with this theory, resonance frequencies were calculated with Equation 1.4:

$$\omega_n = \left(\frac{R_n}{L}\right)^2 * \sqrt{\frac{E_f h^2}{12\rho}} \tag{1.4}$$

Where L, h, E_f and ρ are the length, thickness, flexural modulus and density of the panel; while R_n is a weighted frequency that depends on the boundary conditions of the set up. Consequently, since R_n is constant, and assuming that the changes due to the water exposure on the dimensions and density of the test samples were negligible, it was possible to monitor the change of the flexural modulus by measuring only one resonance frequency.
The dynamic behaviour of each specimen was measured by means of two strain gauges, that were sealed on the outside using silicon rubber in order

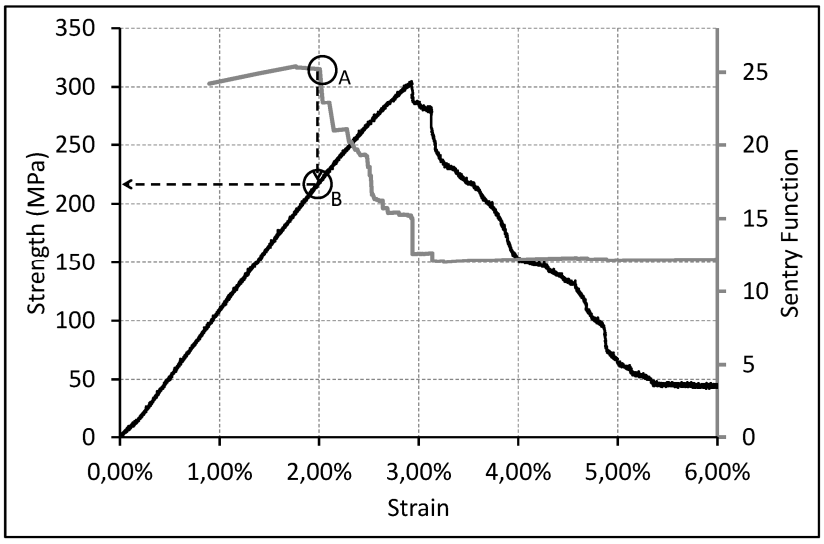

Figure 1.2: Example of stress-strain curve (black line, left axis) with sentry function (gray curve, right axis). Notice how the sentry function grows in the beginning until point A, where it falls almost vertically, showing the first significant failure. The stress at the first failure is then read from the stress-strain curve at the strain level of this drop (point B).

to protect them from the salt water. The specimens were positioned, clamped on one side on a cantilever beam configuration, preloaded on the opposite side and then quickly unloaded to allow them to vibrate freely. The signal generated by the gauges was converted by ADC and processed with the Fast Fourier Transform algorithm in MATLAB to register the first resonance frequency. This procedure was repeated for both types of resin every week for the first month of salt-water exposure, and then every four weeks over a total period of 24 weeks. The test configuration can be seen in Figure 1.3.

Fatigue tests

3PB fatigue tests were performed under load control by means of a universal machine (load cell of $25kN$) the load ratio was kept at $R = \frac{P_{min}}{P_{max}} = 0.1$. In

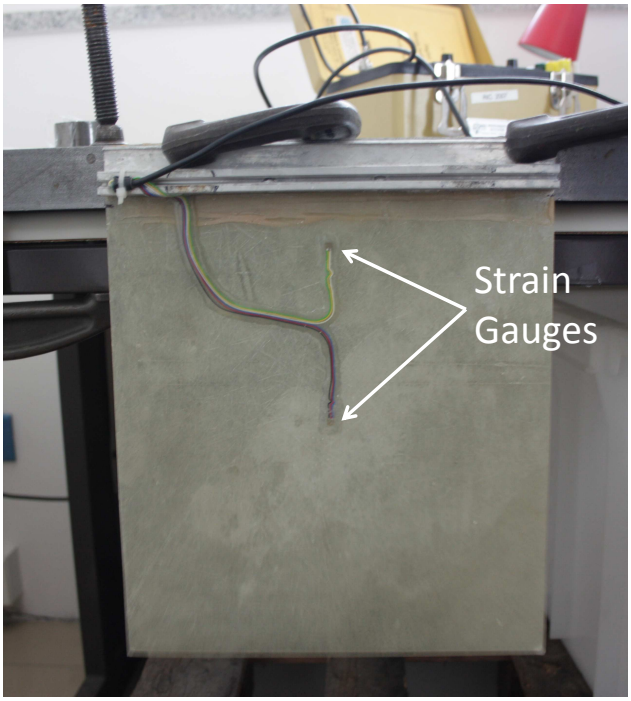

Figure 1.3: Dumping test configuration

this way the minimum load was kept slightly higher than zero in order to avoid the specimen motion, impact on the specimen and the change of the loaded point during the test. The 3PB configuration was the same used for the Q-S tests in terms of span and geometry of fulcrums. The machine was set to cycle at a frequency of $2Hz$.

Four batches of tests, nine specimens for each batch, were tested for both specimen configurations i.e. the matrix material being Polyester and Vinylester resins. At the beginning of the experimental plan, with non-conditioned specimens, nine specimens were tested while exposed to air, another nine were exposed to sea water at room temperature; the test configuration is shown in Figure 1.4.

The last two batches of tests were done with specimens that were exposed to artificial sea water at a temperature of $15°C$ for a period of twenty two weeks; in the same way as explained before for the non-treated specimens, one set of tests was done in a water environment and one with the specimens exposed to air.

A summary of the tests for each type of specimen is presented in Table 3.1.

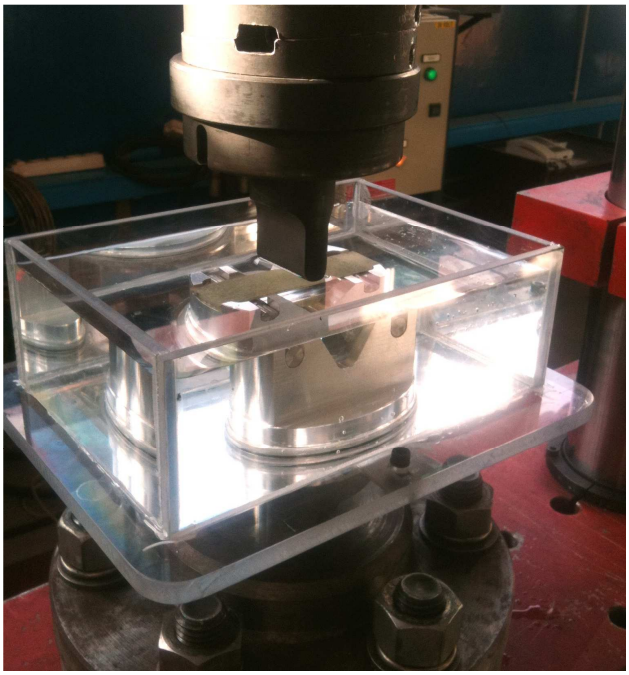

Figure 1.4: Shows the 3PB fatigue test configuration, in this case the specimen was immersed in artificial sea water at room temperature, other tests were done with the specimen exposed to air

1.3 Results

Water absorption

Water absorption was measured by means of gravimetric technique. Each week the specimens were pulled out of the water, their surface was dried using a paper tissue and they were then weighed before re-immersion in water. The average weight evolution for both type of specimens is shown in Figure 1.5. As can be seen, absorption slowed down, reaching saturation after the 22-week immersion period at about 0.35% of weight. This is a quite low absorption value compared to other studies and it could be a consequence of the low water temperature used.

A Fickian linear absorption was hypothesized [17, 19, 27, 28, 29] and a dif-

Table 1.2: Summary of tests

Specimens	Conditioning	Test	Tested in
1 to 9	No	3PB Fatigue	air
10 to 18	No	3PB Fatigue	water
19 to 21	No	3PB Q-S	air
22 and 23	4 weeks	3PB Q-S	air
24 and 25	8 weeks	3PB Q-S	air
26 and 27	12 weeks	3PB Q-S	air
28 and 29	20 weeks	3PB Q-S	air
30 to 38	22 weeks	3PB Fatigue	air
39 to 47	22 weeks	3PB Fatigue	water
48 to 50	22 weeks	3PB Q-S	air
Panel	0-22 weeks	Vibration	air

fusion coefficient was calculated for each family of specimens using Equation 1.5:

$$\frac{M(t)}{M_\infty} = 2\frac{\sqrt{Dt}}{s} \tag{1.5}$$

Where $M(t)$ is the mass at a given time, M_∞ is the saturation mass which was calculated as the average of the last two measures and was 0.343% for Glass/Vinylester and 0.368% for Glass/Ployester, D is the diffusion coefficient, t is the immersion time in seconds and s is the thickness of the specimens.

The diffusion coefficient is more clearly seen in Figures 1.6 and 1.7, where data for Glass/Vinylester in the first case and Glass/Polyester in the second one were plotted using the result of $2/s\sqrt{t}$ on the abscissas and $M(t)/M_\infty$ on the ordinates. The slope of the tendency line obtained is thus $\sqrt{D}$ and the diffusion coefficient D was equal to 8.2415 10^{-8} mm^2/s for Glass/Vinylester and 7.5199 10^{-8} mm^2/s for Glass/Polyester. The correlation value (R^2) of the linear estimations was 0.9564 for Glass/Vinylester data and 0.9805 for Glass/Polyester; this shows quite acceptable fitting for both cases.

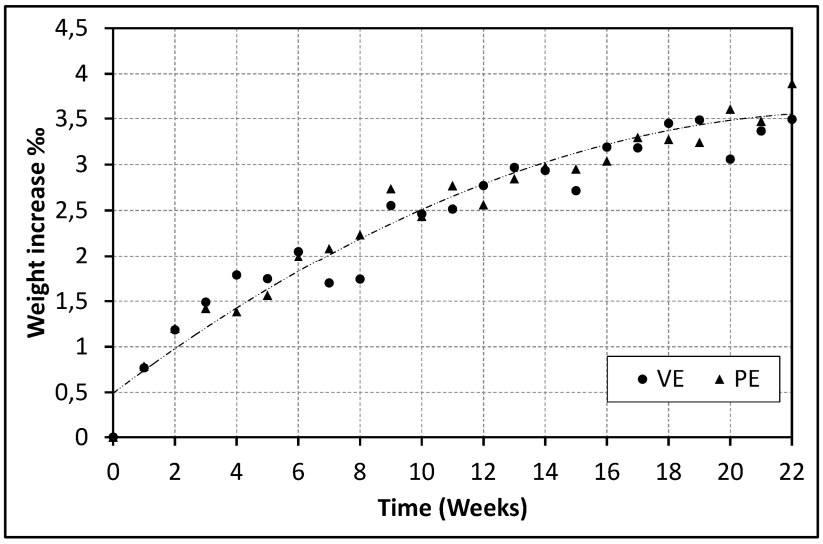

Figure 1.5: Weight increase over time for E-Glass Vinylester (VE) and E-Glass Polyester (PE) specimens. The dashed line is only to guide the eye.

Q-S tests

Following the objectives of the research, stress-strain curves were constructed to compare the data for the specimens; the interest is focused on the degradation of the mechanical properties that water uptake causes. Evolution of the resulting stress at first failure and ultimate strength are presented in Figures 1.8 and 1.9 respectively. The first figure shows very scattered data, while in the ultimate stress figure it is possible to see a net decrease of the values for the water-exposed specimens respect the unexposed ones.

The Student's t-test was performed using these data, assuming equal variance of all the specimens, since all the specimens were cut from the same panel and assuming that water exposure does not increase the variance; and considering only one-tail results, assuming that the water cannot improve the mechanical characteristics of the material, but only decrease them.

In the case of the data of stress at the proportional limit, the post-test alpha of the student's t-test, meaning the probability to have data showing a statistically significant difference to be able to affirm that the characteristics

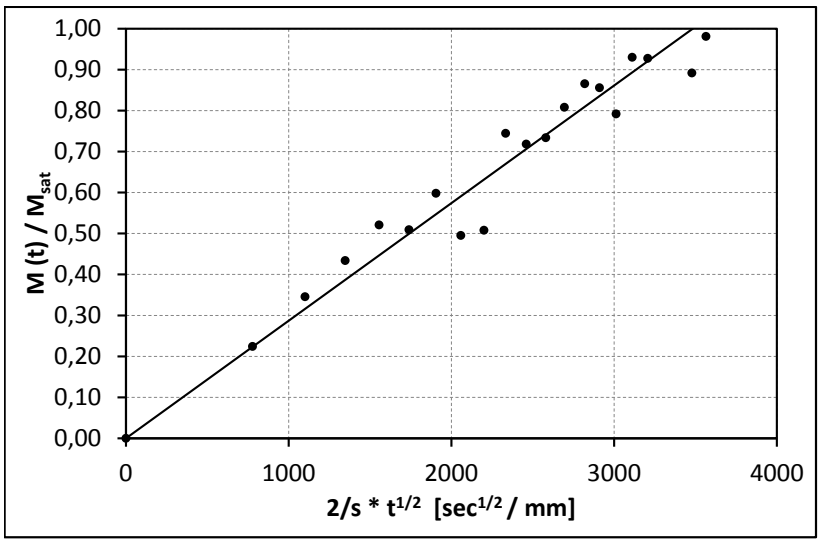

Figure 1.6: E-Glass Vinylester specimens. Fraction of the saturation concentration in terms of the square root of the exposure time divided by half of the specimen thickness. The slope of the tendency line is equal to the square root of the diffusion coefficient, the diffusion coefficient is thus $D = 8,2415.10^{-8} mm^2/sec$

of the material decreased with respect to the non-treated specimens, were for PE specimens: $\alpha_4^* = 93.4\%$; $\alpha_8^* = 72.0\%$; $\alpha_{12}^* = 55.2\%$; $\alpha_{20}^* = 98.9\%$; $\alpha_{22}^* = 99.6\%$. For VE specimens $\alpha_4^* = 97.3\%$; $\alpha_8^* = 88.1\%$; $\alpha_{12}^* = 72.1\%$; $\alpha_{20}^* = 97.7\%$; $\alpha_{22}^* = 99.0\%$. This shows no constant tendency, meaning that α^* goes up and down with no apparent trend (in the same way, the stress values also went up and down), and in some cases the confidence level is too weak. Based on this, it is not possible to conclude any effect of salt-water on the first failure stresses. This does not mean that water improves or degrades the material, it is just not possible to see this from the data obtained in this research. The variance of this property on composites made with fibres oriented randomly (using mat plies) is probably too high to allow sensitivity to changes due to water absorption.

In the case of the data of ultimate stress, the post-test alpha of the stu-

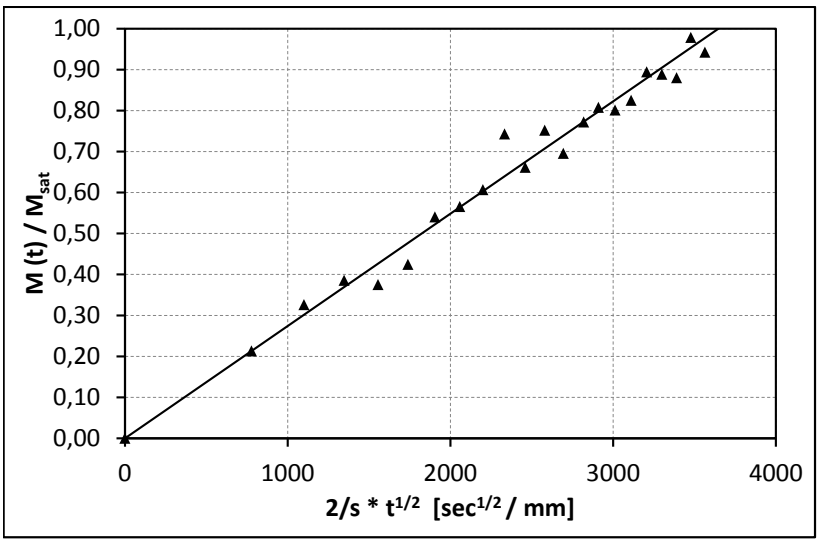

Figure 1.7: E-Glass Polyester specimens. Fraction of the saturation concentration in terms of the square root of the exposure time divided by half of the specimen thickness. The slope of the tendency line is equal to the square root of the diffusion coefficient, the diffusion coefficient is thus $D = 7,5199.10^{-8} mm^2/sec$

dent's t test was, for PE specimens: $\alpha_4^* = 99.4\%$; $\alpha_8^* = 99.3\%$; $\alpha_{12}^* = 95.7\%$; $\alpha_{20}^* = 98.2\%$; $\alpha_{22}^* = 98.7\%$, and for VE specimens $\alpha_4^* = 93.6\%$; $\alpha_8^* = 95.0\%$; $\alpha_{12}^* = 96.9\%$; $\alpha_{20}^* = 97.8\%$; $\alpha_{22}^* = 98.3\%$. Notice that the α^* remains quite high for the specimens immersed in sea water, and fairly constant indifferently of exposure time. This means that the decrease of the mechanical properties happened during the first moments of exposure, which can be visually seen in Figure 1.9, probably because the diffusion rate is higher during the first moments of contact with the water. Assuming this hypothesis, the data were grouped into two categories, i.e. conditioned and non-conditioned specimens, in order to give a value for the water impact on the ultimate strength of the two materials. The decrease in ultimate strength, with a 95% confidence level, was 22 MPa for E-Glass Polyester and 21 MPa for E-Glass Vinylester.

The use of acoustic emission monitoring to compare water-exposed and un-

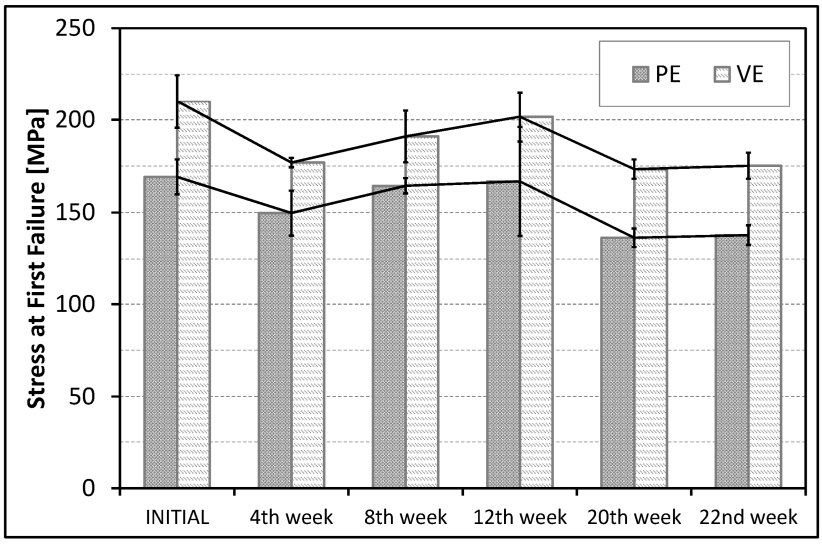

Figure 1.8: Evolution of the stress at the proportional limit for E-Glass Vinylester (VE) and E-Glass Polyester (PE) Specimens.

exposed composite materials was already addressed in references [7] and [30]; in the first, four-point bending tests are used, in the second, tensile tests instead. The results are opposite between these two references; while the first claims increased AE activity for treated specimens with respect to the untreated ones, the second concludes that specimens exposed to water show a drastic reduction in AE activity.

The results obtained in the present research agree with the ones presented in reference [7]: the AE activity was more intense for exposed specimens. This can be seen in Figure 1.10 for E-Glass/Polyester specimens and in Figure 1.11 for the E-Glass/Vinylester ones. The difference is more clear on the amplitude range from 50 to 60 dB.

The shape of the curves is not exactly the same as the one reported by the authors of reference [7], more evident for low amplitudes (40-45 dB), this could be due to many factors but it is important to remark that a higher AE activity for the exposed specimens was detected.

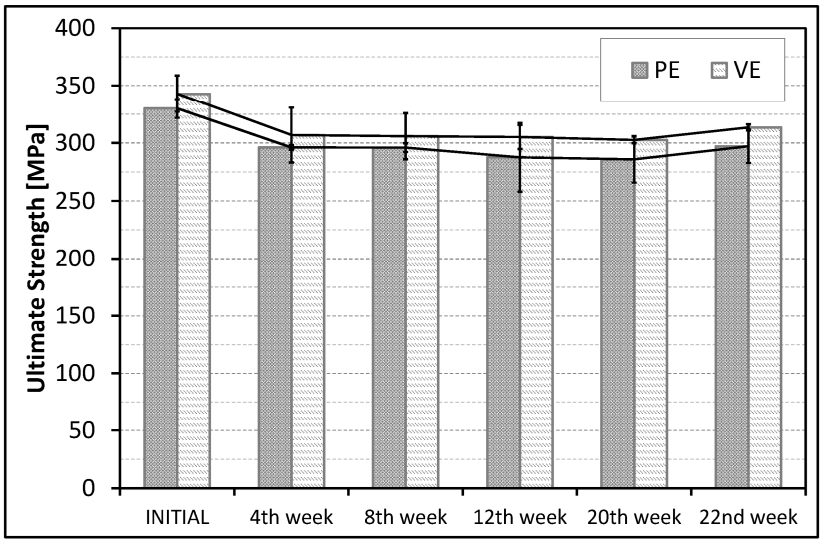

Figure 1.9: Evolution of the ultimate strength for E-Glass Vinylester (VE) and E-Glass Polyester (PE) Specimens.

Dumping tests

Figures 1.12 and 1.13 show the results of the evolution of the flexural modulus Glass-Polyester and Glass-Vinylester of specimens, in the form of $\frac{E}{E_0}$ versus time, where E was the measured value at time t and E_0 was the initial value. As can be seen, the value is quite constant for both kinds of specimens. This result is in agreement with reference [31], where a non changing modulus was reported for E-Glass-Vinyester specimens after 6 months of deionized water conditioning. Reference [14] also showed almost invariable modulus with water exposure.

In the literature different types of behaviour for the modulus have also been reported. Some references present very scattered data or variations inside the experimental uncertainty, like reference [2], which reported a decrease of 10% to 20% for E-glass/Polyester samples and about 30% for E-Glass/Vinylester samples after exposure to 30° C seawater for almost 20 days, but the scattering of the data is visibly high. The study [3] conducted where flexural tests on 4 mm laminates of E-glass reinforced with several resins showed that flexural

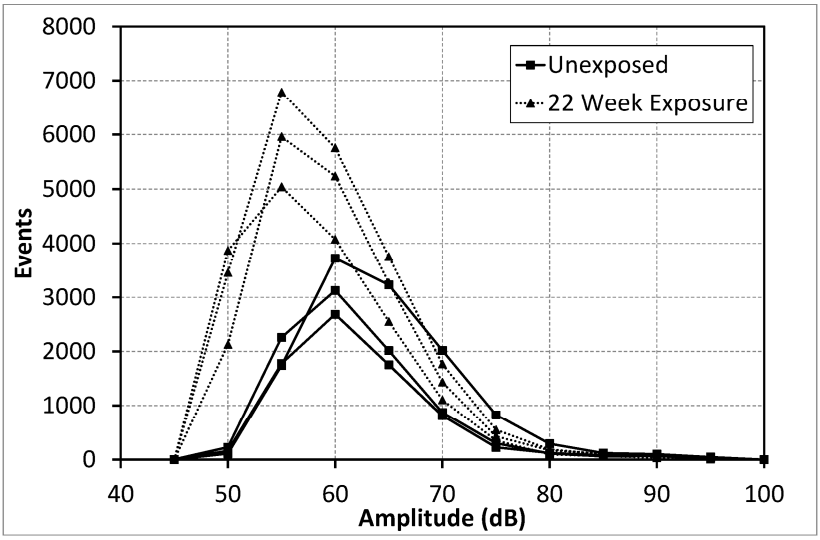

Figure 1.10: Acoustic Emission activity for 22-week-exposed and unexposed E-Glass-Polyester specimens.

modulus changed by −5% for glass Polyester and +2% for glass Vinylester, after five months of seawater exposure at 30° C, but the standard deviations of the values are larger or close to the differences found. Reference [32] also reported flexural modulus from flexural tests and showed that the modulus remained quite constant during the first 6 months of conditioning and then decreased for glass/polyester specimens, while specimens of Glass/vinylester showed an increase in the modulus. Reference [33] performed damping tests, a configuration that shows very good precision, where a single specimen was always used, which makes it possible to avoid the uncertainty that comes from specimen inhomogeneity. The authors showed that the storage modulus (E') changed 7% after 8 weeks of conditioning at 80° C and 90% of humidity. Specimens were made of glass reinforced epoxy and the moisture saturation was reached after about 1.5% of mass gain.
The differences could have been caused only by variations in the materials tested in each study, or it could be evidence of a possible interaction between humidity and temperature.

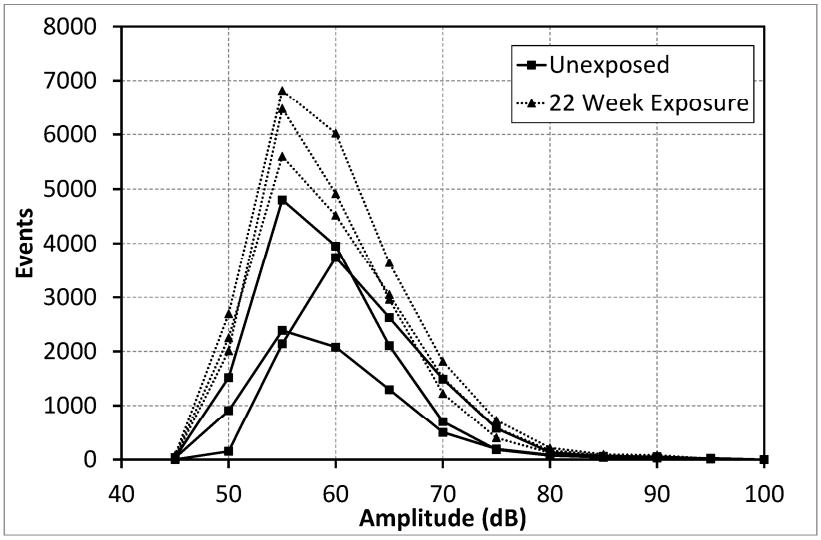

Figure 1.11: Acoustic Emission activity for 22-week-exposed and unexposed E-Glass-Vinylester specimens.

Fatigue tests

The analysis of fatigue data was performed as recommended in ASTM Standard E739 [34]. A model of the type $log(N) = A + B*(\frac{\sigma_{max}}{\sigma_{UTS}})$ was implemented with good results to fit the data and obtain characteristic lines for fatigue lives. Specimens that run for more than a million cycles were considered run-off's and not included in the analysis.

The results for E-Glass Polyester resin are shown in Figure 1.14; as can be seen there is no appreciable difference between dry and treated specimens. The obtained fatigue life line for specimens that were immersed in water for a twenty two week period falls in almost exact coincidence with the one for the non-conditioned specimens, and this is true for both dry and in-water tests. However, there is a difference between the fatigue life of specimens tested in each environment, the specimens showed a better performance when tested in water. It is necessary to remark that the lines for all four configurations

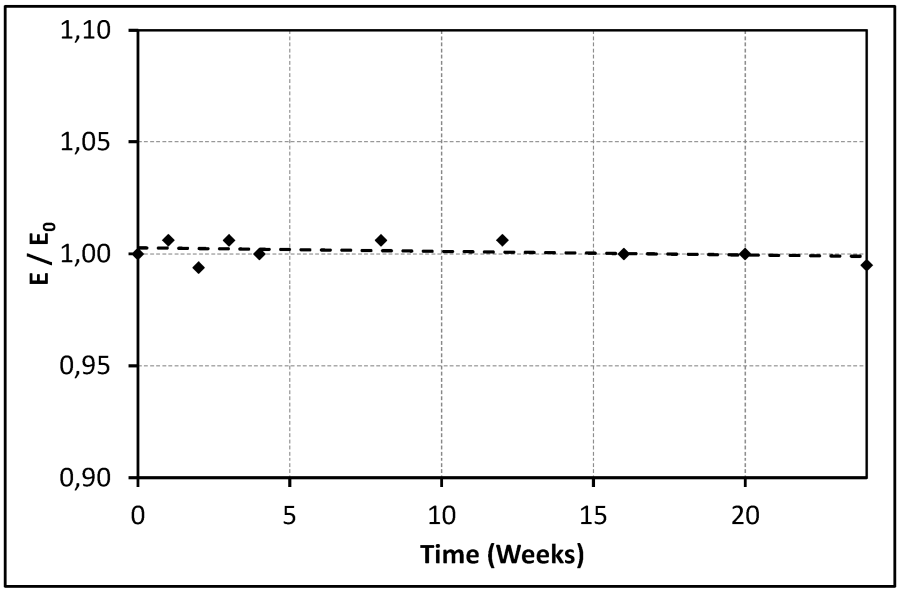

Figure 1.12: Evolution of the flexural modulus for Glass/Polyester specimen

are inside the confidence interval of any of them (shown as dashed lines), meaning that, strictly, there is no statistically appreciable difference between the lines for any test configuration. Although this is true, the fact that exactly the same behaviour was found for E-Glass Vinylester specimens (Figure 1.15) could be taken as further evidence that this behaviour is not a simple random coincidence.

An explanation for the fatigue life difference found between specimens tested in water with respect to those tested in dry conditions could be that the $2Hz$ speed set for the testing was not slow enough to avoid internal heating of the specimens. The internal heat was better released when the specimens were immersed in sea-water because the heat-transfer coefficient of the water is higher than that of the air. The dependence of fatigue life on a specimen's temperature is a topic already studied by other researchers. It is a conclusion of reference [35], a work done with composite laminates, that internal heating of the specimen is so important that by analysing the temperature of the external surface of the specimens during the application of cyclic loading, it

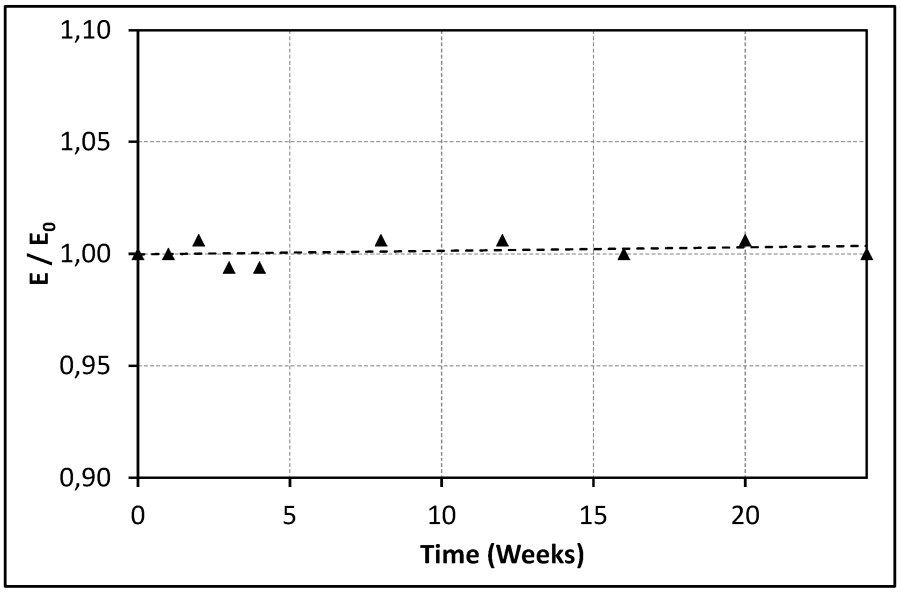

Figure 1.13: Evolution of the flexural modulus for Glass/Vinylester specimen

is possible to evaluate the damage evolution. Reference [36] suggested something similar; after doing fatigue tests at different frequencies and monitoring the temperature with an infra-red thermometer the authors found that thermal energy, which is the amount of mechanical energy dissipated in the form of heat, evaluated in the first few load cycles was a good parameter to predict fatigue life. Also in reference [4] fatigue tests were performed at different temperatures; specimens tested at higher temperature showed weaker fatigue performance.

In the present research, the improved ability to dissipate internal heating of the specimen provided by the water proved more important than the damage it could cause on the material. The exposure to sea-water at $15°C$ for a period of twenty two weeks was not appreciable in terms of fatigue life expectancy of the materials, although they absorbed an average of 0.35% of their weight during the exposure.

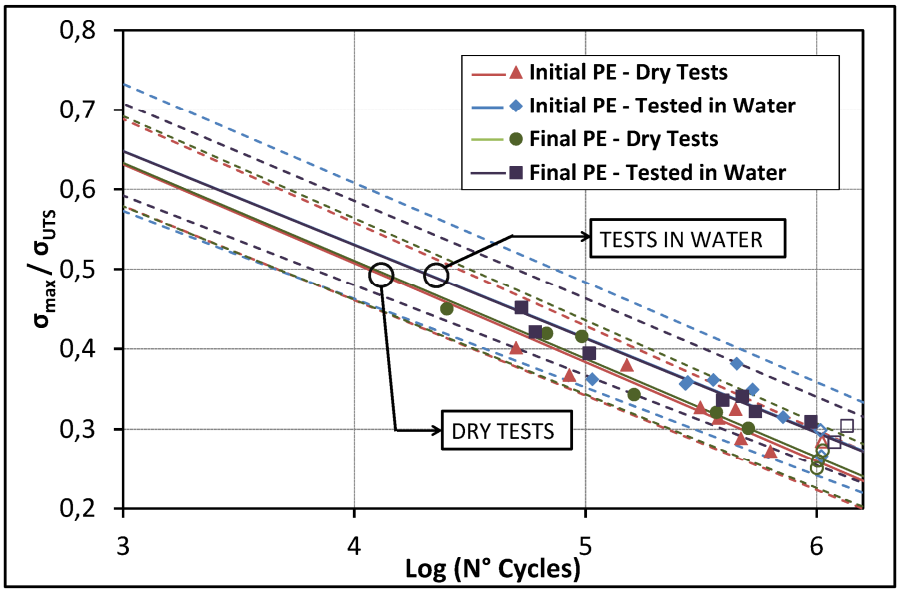

Figure 1.14: Fatigue results of E-Glass Polyester specimens

1.4 Conclusions

The current investigation included Quasi-Static, vibration and fatigue tests that were performed on E-Glass reinforced with Polyester and Vinylester resin systems. Specimens were made using the Vacuum Assisted resin infusion process. These are materials and technology are frequently used in marine applications. The objective was to understand the degradation that the material could suffer if it comes into contact with sea-water, as can happen if the commonly used protective layer of gel-coat gets damaged.
Several unexposed specimens were tested in order to obtain the reference material properties. The rest of the specimens were immersed in water at $15°C$ and weighed every week to get the water absorption from the mass gain. Q-S tests were performed each month. Behaviour was symmetric for each resin, where results showed a decrease in ultimate strength in the first month and then remained fairly constant. The decrease was about 6% for Glass/Vinylester and 7% for Glass/Polyester specimens. The tests were also

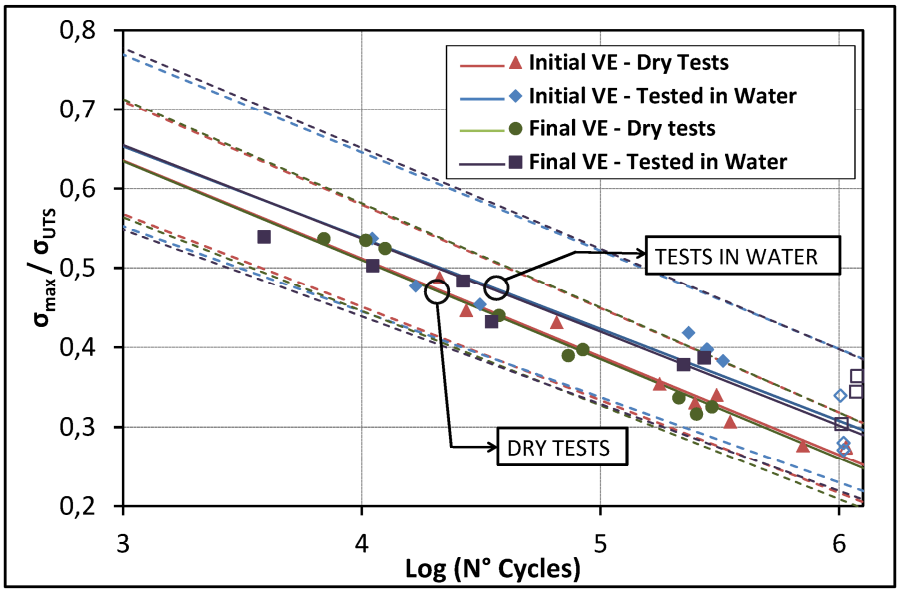

Figure 1.15: Fatigue results of E-Glass Vinylester specimens

monitored for acoustic emissions and these results were used to get the strength at first breakage, but in this case the dispersion between specimens was too high to clearly understand the effect of the absorbed water, though a considerable increase in the acoustic activity was detected for aged specimens.

Vibration tests were used to obtain the evolution of the flexural modulus, where no change was detected.

In the case of fatigue analysis, the tests were performed before and after the water exposure, and in both cases tests were done in wet and dry environments. The specimens tested in water showed better fatigue resistance, probably because of the improved heat transfer provided by water environment. There was no appreciable difference between fatigue response of aged specimens with respect to the untreated ones, for both matrix systems tested. The results show very good resistance of this kind of material towards seawater, much better than metals. As a final anecdotal remark of this study, the loading nose used for flexural testing, made of stainless steel, became very

rusted during the fatigue experimentation performed in water environment, as can be seen in Figure 1.16.

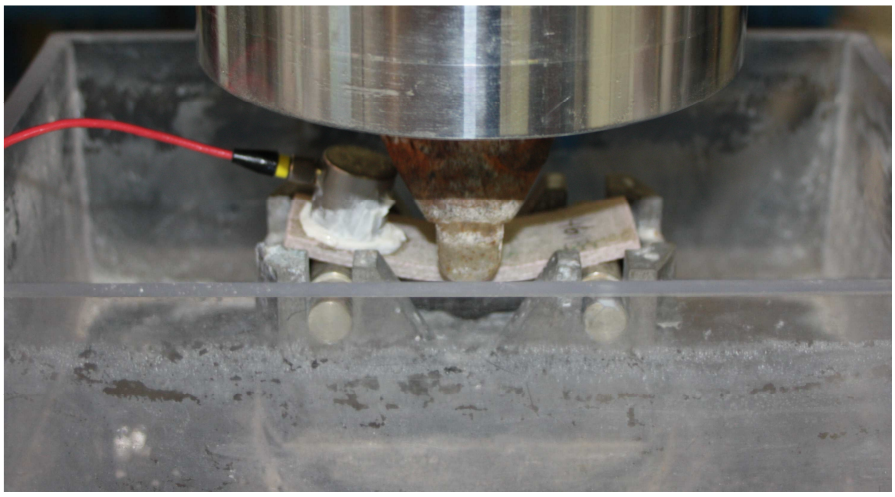

Figure 1.16: Picture taken during the last Q-S testing, notice the very rusted loading nose, this happened during the fatigue experimentation in water environment

2 CHARACTERIZATION OF THE CURE KINETICS OF A THERMOSETTING MATRIX

SIMPLE METHOD TO CALCULATE THE PARAMETERS OF THE KAMAL-SOUROUR MODEL

2.1 Introduction

High performance applications of composite materials e.g. automotive or industrial machinery, demand bigger production volumes, leading to a requirement of higher efficiency and optimized production cycles. The use of thermosetting resins as matrix material of composite materials is a widespread practice and the curing is a delicate stage of the production process, for this reason the study of the curing cycle becomes of paramount importance.
The challenge is to cure the resin of the part being fabricated in the least possible time, without degrading it. Degradation is prone to occur in case the curing is over accelerated, since the chemical process is exothermic.
It is possible to investigate the curing process and to optimize it by numerical simulation. However, before the investigation of the curing could be made, the resin must be characterized.
Because of the rather complicated chemical reaction involved in the polymerization process, the analysis of the cure kinetics is usually studied with a phenomenological approach, where the scope is not to understand the contribution of each single reaction involved, but to give a description of the global process obtained by the contribution of all the reactions involved.
Different testing techniques have been used to study the curing process of thermosetting resins, such as Fourier Transformation Infra-Red analysis (FTIR), or the Differential Scanning Calorimetry (DSC), both isothermal and dynamic methods can be adopted. With the FTIR it is possible to track the variations in the concentration of the different functional groups involved, while the DSC follows the evolution of the heat generation associated with the exothermic reactions characteristic of the polymerization process.
For the method using isothermal DSC analysis, the one applied in the present work, the sample is placed in the DSC furnace that was pre-heated at the

pre-set curing temperature. The system is kept at that temperature and the instrument records the change of heat flux as a function of time. Assuming that the heat evolved during the curing process is directly related to the reaction proceeding [75], the area of the exothermic peak ΔH_{Tiso} is considered as the total reaction heat that can be developed in that particular isothermal condition. When integration of the heat flux curve is carried out up to a given time t, the ratio of this partial evolved heat (ΔH_t) with total reaction heat (ΔH_{Tiso}) is used to determine the fractional conversion α_t of the epoxy resin, by equation 1.6.

$$\alpha_t = \frac{\Delta H_t}{\Delta H_{Tiso}} \tag{1.6}$$

The actual rate of cure can be generally expressed as in equation 1.7

$$\frac{d\alpha}{dt} = k(T) \cdot f(\alpha) \tag{1.7}$$

Where $f(\alpha)$ is a function of the fractional conversion α_t and $k(T)$ is the temperature dependent apparent rate constant. The latter can be described by an Arrhenius equation, as in 1.8:

$$k(T) = A \cdot e^{-\frac{E_a}{RT}} \tag{1.8}$$

where A is the pre-exponential factor, E_a is the apparent activation energy, R is the gas constant, and T is the absolute temperature.
A lot of empirical models were put forward to give a shape to the function for the curing of epoxy resins [76] [77] [78] [79]. However, the most common approach applied in this case seems to be based on the autocatalytic model first proposed by Horie et al. [80] and further modified by Kamal and Sourour, described by equation 2.1:

$$\frac{d\alpha}{dt} = k(T) \cdot \alpha^m \cdot (1-\alpha)^p \tag{1.9}$$

Where $m+p$ is the total reaction order. Although many Authors [76] [81] [82] tried to investigate the physical meaning of the m and p parameter appearing in the Kamal-Sourour equation, no reliable definite physical interpretation is actually provided.
This section presents a straightforward procedure developed to obtain the parameters of the Kamal-Sourour model. This is a more simple procedure with respect to other ones explained in literature. The main difference is that it takes advantage of the possibility to obtain a mathematical relation from the experimental results between the reaction orders m and p; this allows the use of a lineal regression instead of a multiple one.
In order to make a more clear explanation, the method will be explained following an example characterization.

2.2 Materials and methods

The resin used for the example presented in this section was the epoxy EC14 with hardener W61 provided by ELANTAS (mixing ratio of 100:17 by mass). The Kamal-Sourour model is based on experimental data, for its construction isothermal DSC measurements were carried out on a TA Instruments Q2000 DSC Modulated apparatus equipped with RCS cooling system. Every sample (10-15mg) was extracted from a unique mixture, which was kept in fridge between the tests.
Mathematically, three curves would be enough to estimate the parameters, however it is recommended to use at least five. To select the temperatures at which performing the isothermal experiments, it is useful to first run a preliminary temperature-scan DSC. From this test it is possible to get the temperature at which the reaction starts and the one of maximum exothermy; the isothermal DSC analysis should be performed at temperatures between these two (Figure 1.17). The preliminary DSC experiment on temperature scan is also practical to obtain the reaction enthalpy (ΔH_{tot}), this is done by integrating the curve below the baseline.
The isothermal DSC curves obtained for the EC14-W61 are presented in Figure 1.18. It is possible to transform this data to obtain the degree of cure

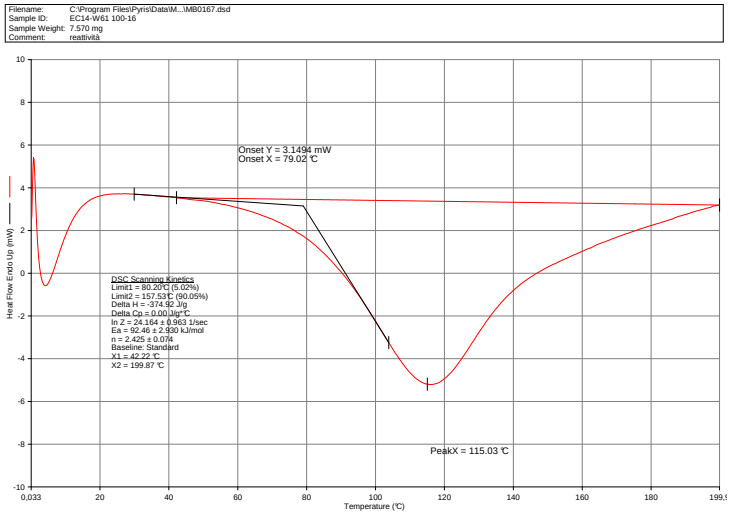

Figure 1.17: DSC analysis on temperature scan

through time for each curve. The degree of cure can be expressed as the heat evolved at time t, divided by the total reaction enthalpy, obtained from the preliminary test:

$$\alpha(t) = \frac{\int_0^t \Delta H}{\Delta H_{tot}} \tag{1.10}$$

Once the degree of cure as a function of time is obtained for each isothermal experiment (Figure 1.19), the cure rate as a function of cure degree is calculated by obtaining the instant slopes of the curves. These last are the curves which would be fitted with the Kamal-Sourour model, which describes the cure kinetics expressing the reaction rate as function of the instant degree of cure and temperature ($\frac{d\alpha}{dt} = f(\alpha, T)$). The result for the example is shown in figure 1.20.

2.3 Obtaining of the parameters and construction of the model

The data for curing rate as a function of cure degree for each temperature, obtained in the last step, will be used to obtain the parameters from Kamal-

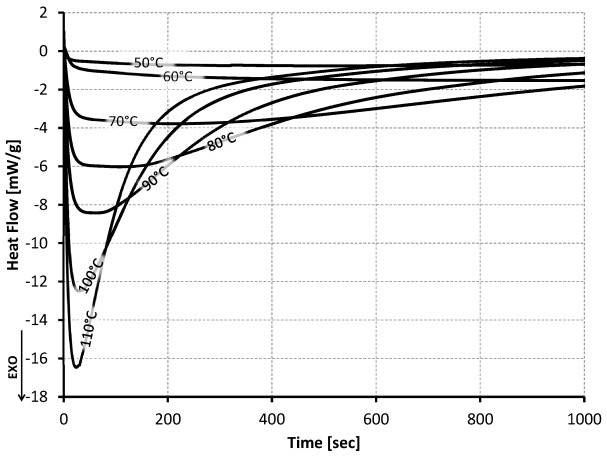

Figure 1.18: Results from isothermal DSC analysis

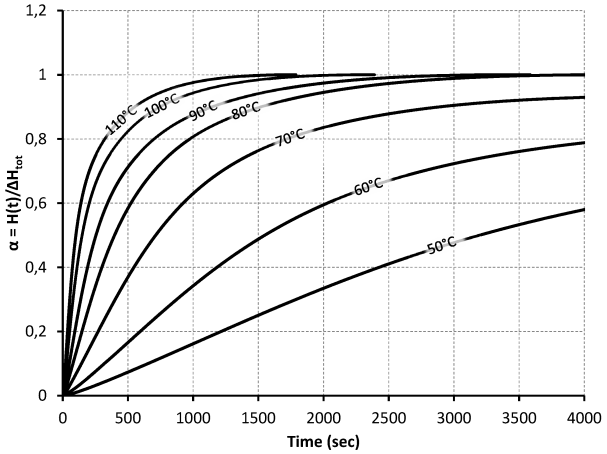

Figure 1.19: Results of degree of cure through time obtained by integrating the curves in figure 1.18

Sourour model. The general expression of the model is:

$$\frac{d\alpha}{dt} = Ae^{-E_a/RT}\alpha^m(1-\alpha)^p \tag{1.11}$$

It is usually seen that the full conversion is not reached at low temperatures.

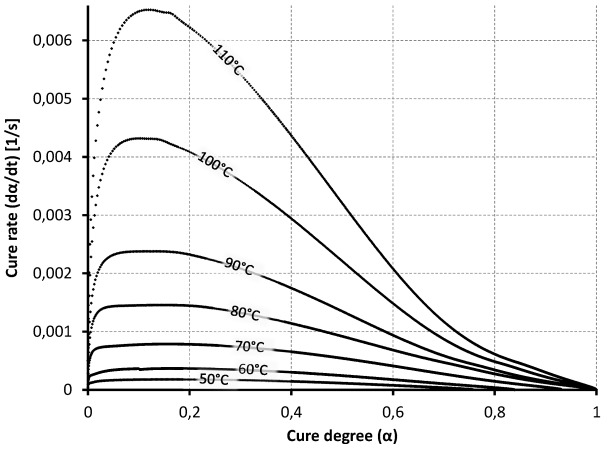

Figure 1.20: Cure rate as function of cure degree for each temperature obtained by differentiation about time of curves in figure 1.19

For example for the EC14-W61 the maximum degree of cure reached (α_{lim}) for each cure temperature is shown in figure 1.21. Also m and p are seen to vary with the cure temperature.

By making few modifications it is possible to introduce these effects; the

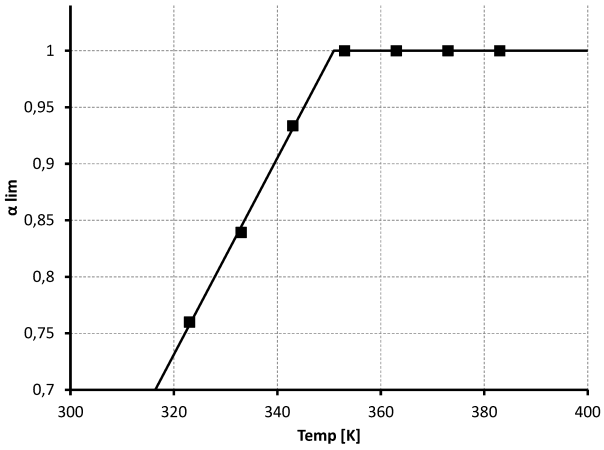

Figure 1.21: Maximum degree of cure at different curing temperatures obtained for EC14-W61 resin

new equation of the model becomes:

$$\frac{d\alpha}{dt} = Ae^{-E_a/RT}\alpha^{m(T)}(\alpha_{lim}(T) - \alpha)^{p(T)} \tag{1.12}$$

Usual procedure

The most wide spread procedure would be to apply logarithms on both sides of equation 1.12 to obtain equation 1.13

$$\ln(\frac{d\alpha}{dt}) = \ln(A) - \frac{E_a}{RT} + m(T)ln(\alpha) + p(T)\ln(\alpha_{lim}(T) - \alpha) \tag{1.13}$$

For each isothermal $(\ln(A) - \frac{E_a}{RT})$ is constant, as well as $m(T)$ and $p(T)$. In this way, for each isothermal experiment, a value of $m(T)$ and $p(T)$ could be determined by using a multiple regression approach of the form

$$Y = Z + BX_1 + CX_2$$

where $Y = \ln(\frac{d\alpha}{dt})$, $X_1 = \ln(\alpha)$, $X_2 = \ln(\alpha_{lim}(T) - \alpha)$ and the parameters to estimate are $Z = ln(A) - \frac{E_a}{RT}$, $B = m(T)$ and $C = p(T)$.

New procedure

It is possible to work with a linear regression approach by making an easy algebraic substitution. As it can be seen in figure 1.20 all the curves present only one maximum value. In other words, $\frac{d(d\alpha/dt)}{d\alpha} = 0$ in only one point (α of maximum rate α_{mr}), where $\alpha_{mr} \in (0; \alpha_{lim})$ (Figure 1.22).
Then:

$$\frac{d(d\alpha/dt)}{d\alpha} = Ae^{-E_a/RT}\frac{d(\alpha^{m(T)}(\alpha_{lim}(T) - \alpha)^{p(T)})}{d\alpha} = 0$$

$Ae^{-E_a/RT} \neq 0$, so we can exclude it from the equation.

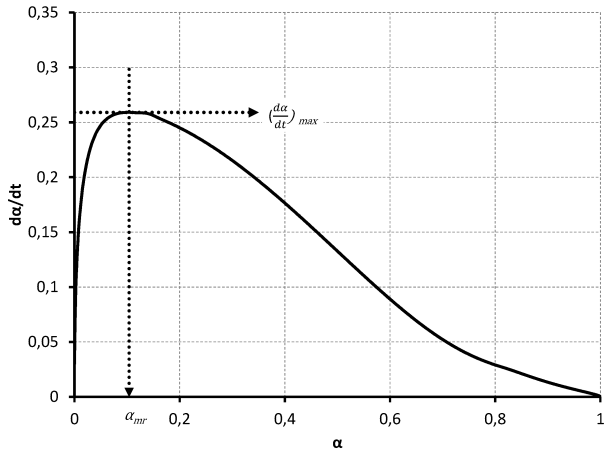

Figure 1.22: $\frac{d(d\alpha/dt)}{d\alpha} = 0$ when $\alpha = \alpha_{mr}$

Resolving the derivation, we obtain:

$$-\alpha^{m(T)-1}(\alpha_{lim}(T) - \alpha)^{p(T)-1}(m(T)\alpha - m(T)\alpha_{lim} + p(T)\alpha) = 0$$

Which has three possible solutions. From these, $\alpha = 0$ and $\alpha = \alpha_{lim}$ are solutions outside the limits of interest, the reaction rate is null at the starting and ending points.
The solution of interest is obtained by resolving the remaining part of the equation:

$$(m(T)\alpha - m(T)\alpha_{lim} + p(T)\alpha) = 0$$

In this way it is found that $\alpha = \frac{m(T)\alpha_{lim}}{m(T)+p(T)}$ is the only solution left, we will call this value of α as α_{mr}.
Thus, it is possible to express $p(T)$ as a function of $m(T)$ as:

$$p(T) = m(T)\frac{\alpha_{lim} - \alpha_{mr}}{\alpha_{mr}} \tag{1.14}$$

Combining equations 1.13 and 1.14, the following equation is obtained:

$$\ln(\frac{d\alpha}{dt}) = \left(\ln(A) - \frac{E_a}{RT}\right) + m(T)\left(ln(\alpha) + \frac{\alpha_{lim} - \alpha_{mr}}{\alpha_{mr}}\ln(\alpha_{lim}(T) - \alpha)\right) \tag{1.15}$$

Again, the term $\ln(A) - \frac{E_a}{RT}$ is constant for each isothermal curve. In this way equation 1.15 can be analysed with a simple linear regression approach of the form

$$Y = Z + BX$$

where $Y = \ln(\frac{d\alpha}{dt})$ and $X = \left(ln(\alpha) + \frac{\alpha_{lim}-\alpha_{mr}}{\alpha_{mr}}\ln(\alpha_{lim}(T) - \alpha)\right)$. X and Y can be constructed from the experimental data. The parameters to estimate are the y-intercept $Z = \left(\ln(A) - \frac{E_a}{RT}\right)$ and the slope of the regression line $B = m(T)$.

Applying this to the example, figure 1.23 shows the plot of X and Y for one of the isothermal experiments ($50°C$) performed on the EC14-W61 resin. In the same figure the linear regression is also shown. Notice that the regression fits correctly with the curve on only the first part of it (the data points in the interval $[\alpha = 0.1 \ ; \ \alpha = 0.6]$ were used in this case).

This deviation from the line seen for the first and last data points was already reported by other researchers, and considering them would give a bad fit of the model. Naturally, this also occurs with the multiple regression procedure, the great advantage of the linear regression approach is that it is easier to manage it to change the part of the experimental data used to fit the model. Another technique would be to iterate different values in order to minimize the squared differences between the model curve and the one obtained from the experiments, in this case the procedure describes is also very helpful since one has to deal with less parameters during the iteration. Figure 1.24 shows the result compared to the experimental data of the $50°C$ experiment.

The process must be repeated for each isothermal set of data to get the values of Z and $m(T)$. In each case $p(T)$ is obtained by applying equation 1.14.

Once all the data has been processed it is possible to calculate the final parameters of the model. It is usual procedure to express $m(T)$ and $p(T)$ as linear functions of the temperature T. The result for the example is represented in figure 1.25.

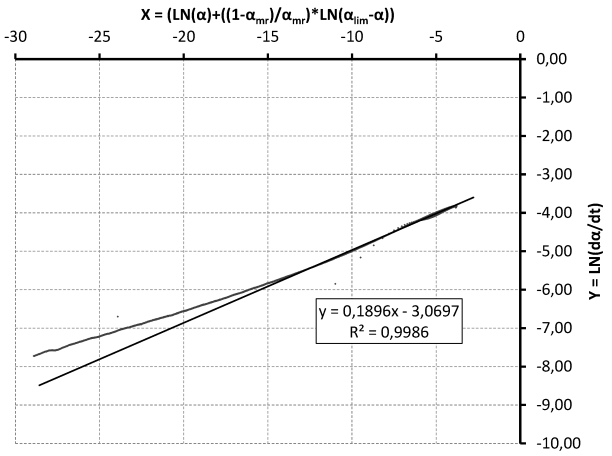

Figure 1.23: Plot of X-Y values and linear regression obtained for the $50°C$ isothermal experiment performed on the EC14-W61 resin

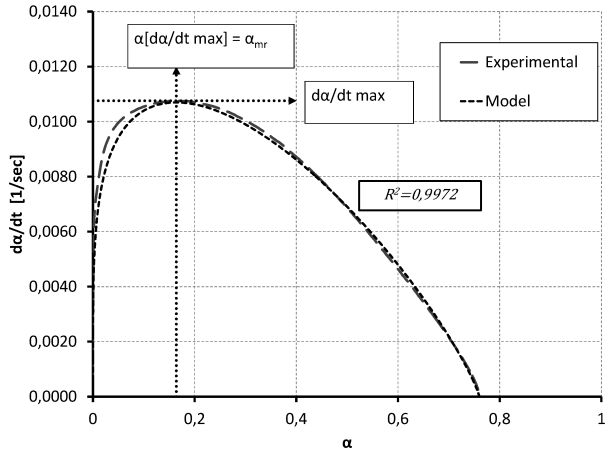

Figure 1.24: Experimental and model curves for the EC14-W61 resin at $50°C$

In the case of parameter $Z = \left(\ln(A) - \frac{E_a}{RT}\right)$, by applying antilogarithm it becomes $e^Z = A^{-E_a/RT}$. In this way the parameters A and E_a/R can be obtained by performing an exponential fit of e^Z as a function of $1/T$. Figure 1.26 shows the plot for the example characterization with it's fitting curve and final results.

At this point all the parameters of the model have been obtained, these

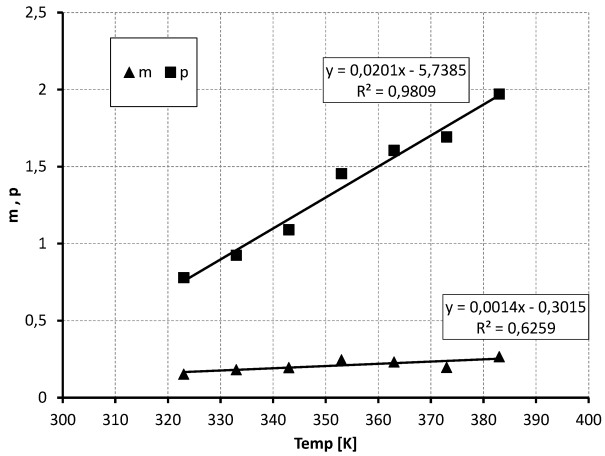

Figure 1.25: Results for m and p obtained for the EC14-W61 resin

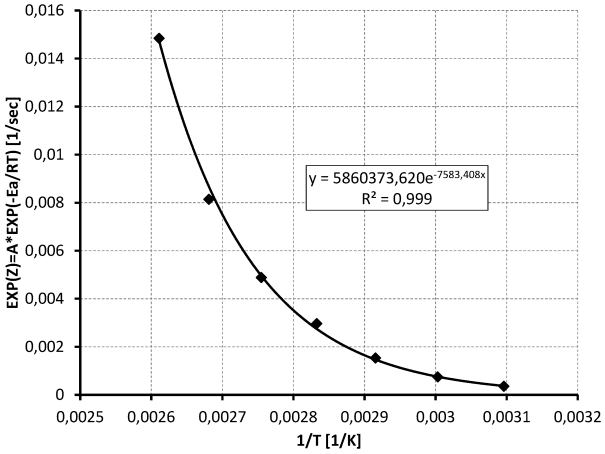

Figure 1.26: e^Z vs. $1/T$ plot for the EC14-W61 resin and its exponential fit showing the values of A and E_a/R to be used in the model

are expressed in table 1.3. The model compared to the experimental data is shown in figure 1.27.

Table 1.3: Final parameters of the Kamal-Sourour model for the EC14-W61 resin

Parameter	value
A	5860373.62 sec^{-1}
E_a/R	7583.41 K
$p(T)$	$0.02011T - 5.73849$
$m(T)$	$0.00145T - 0.30146$
α_{lim}	$0.0087T - 2.0493$ if $T \leq 350.9224$ K 1 if $T > 350.9224$ K

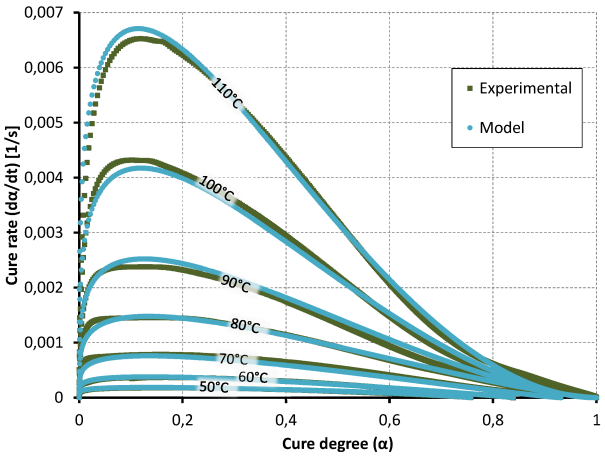

Figure 1.27: Experimental and model curves for the EC14-W61 resin

2.4 Conclusions

The Kamal-Sourour model has been widely applied to characterize the Cure-Kinetics of thermosetting resin. In this section a simple procedure developed to obtain the parameters has been explained and applied to one resin as an example. The new approach uses an algebraic substitution which allows the construction of a relation between reaction orders m(T) and p(T) from experimental data. Knowing this relation it is possible to use a linear regression as the main instrument to fit the model, instead of the usual multiple regression approach which is easily found applied by other researchers.

Chapter 2

Manufacturing Technology: Prepreg Cured in Autoclave

1 EMPOWERING AUTOCLAVE PROCESS THOUGH RAPID PROTOTYPING TECHNOLOGIES

APPLICATION OF RAPID TOOLING FOR THE PRODUCTION OF MOULDS SUITABLE FOR AUTOCLAVE FORMING OF CFRP

1.1 Introduction

In many industrial applications, for example in the case of the production of automatic machines for packaging that should be able to adapt rapidly to different tasks, there is a tendency to transfer Rapid Prototyping (RP) techniques to Rapid Manufacturing (RM), i.e. To use RP as a production technology for components. These components are generally characterized by complicated geometrical shapes and high functional values but they are structurally weak especially if manufactured using polymers and the polyjet (PJET) technique [38], [39]. Better structural performances can be obtained by Selective Laser Sintering (SLS) of metals, but the specific (i.e. per mass unit) strength or stiffness remains low.

Reduction of the tooling costs and the ability to deliver low production volume is perhaps the most distributive aspect of RM [40]. This is sometimes achievable by directly producing of the part, but for some materials there

are still not RP technologies available, in these cases RM could be achievable trough Rapid Tooling (RT) techniques [41].
Some advanced applications, for example in sports, automotive or motorbike racing or aerospace applications [40] require the rapid development of small series of high specific mechanical properties components. In these cases autoclave cured carbon fibre reinforced plastics (CFRP) are often utilized.
CFRP, which is composed of tows of carbon fibre filaments immersed in a polymeric matrix, has remarkable mechanical properties and low density. This makes it very suitable for many applications where a high strength and stiffness to weight ratio is needed or preferable; it also offers the stiffness of steel at one fifth the weight [42].
Autoclave cured CFRP components are usually two dimensional components; the thickness is given by stacking several uni- or multi- directional plies joined together by the polymer matrix. There are different techniques to produce CFRP components. It is possible to start from the dry woven fabrics and wet it by hand or infusion process, or to start from pre-impregnated layers. The second option allows more control on the fibre/matrix volume rate since the pre-impregnated layers already have the optimizing amount of resin. For any method used, at least one open mould is needed to shape the component. When the matrix polymer is a thermosetting resin such as epoxy, a pressure and temperature cycle is performed to compact the layers in the mould and to cure the matrix and this cycle is usually done in an autoclave. The mould used to form the composite thus suffers the thermal and mechanical loads present in the autoclave. Other composite production methods such as resin transfer moulding (RTM, which will be studied in the following chapter), pultrusion or filament winding are more suitable to high volume production with higher initial investment [42].
Moulds used in autoclave forming can be made of different materials; a common technique is to make them with the same composite material as the component they will form. This allows light weight moulds and no mismatch in thermal expansion [43], but in order to make this mould, a pre-mould (or master model) is needed, which is usually machined out from a plastic tooling block. Figure 2.1 shows the work flow when using a composite mould. For the production of the composite mould, a pressure and temperature cycle is

needed, which is also performed in autoclave. However, since the thickness of the mould is considerably higher than the thickness of the parts to be produced, and since tooling blocks are usually not suitable for resisting high temperature and pressure, the cycle is much longer, resulting in an expensive resource consuming step. Composite moulds have an expected tooling life of around 100 pieces.

When a higher number of parts is needed, the most common option is to make the moulds in aluminium, the drawback is that aluminium has a much higher thermal expansion coefficient (CTE) than composites. This mismatch generates residual stresses in the matrix. The thermal conductivity is also different, and thermal inertia is much higher, so temperature cycles need to be revised when using metallic moulds. The CTE problems can be resolved using Invar alloy (e.g. FeNi36) instead of aluminium, but the other issues will still be present.

Many methods for rapid tooling have been developed so far, for the applica-

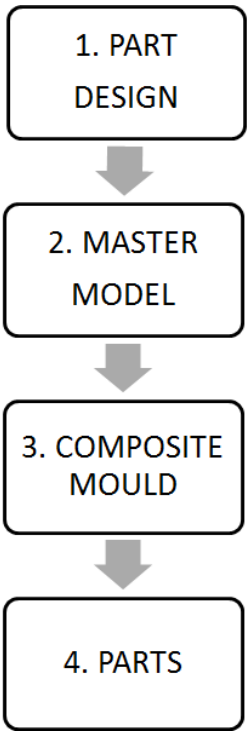

Figure 2.1: Workflow

tion on many production processes including injection moulding ([44], [45],

[46],[47], [48], [49], [50], [51]), investment casting [49], sheet metal forming [52] and RTM [53].

In reference [44] the authors introduce a novel material composed of iron filled polymer that can be processed using the SLS technique, they point out that the material has lower mechanical and thermal properties than steel, enough however for the production of inserts.

Reference [45] considers the production of an iron filled ABS filament to produce the inserts by fused deposit modelling (FDM). Both articles present a direct rapid tooling technique, where the moulds are mainly produced using additive layer manufacturing (ALM).

On composite applications Gibbons et al. [53] used of rapid prototyping, tooling and manufacture technologies to provide rapidly configured and reconfigurable tool concepts, for low-cost resin transfer moulding. On the article they report using the SLS RP technology to produce titanium metallic inserts for a low pressure (1-2 Bar) RTM process. Also they used sintered porous media to increase resin flow.

Due to the highly demanding autoclave environment, with pressures up to 6 Bar and temperatures that can reach $100 - 150°$ C, it was not possible to utilize a direct rapid tooling technique based on plastics, so indirect techniques were considered. In this section one indirect rapid tooling methodology was investigated in particular.

On this topic, according to Wholers [54] filled epoxies have been used in indirect rapid tooling for a long time. These moulds, having a low processing cost, are very competitive when used in the manufacturing of low volume production plastic parts. Many authors have reported indirect rapid tooling procedures and results. Vasconcelos et al. [55] analysed the possibility of using epoxy filled with aluminium powder together with short glass fibres. The addition of the fibres aims to reduce the wear that the injection of the plastic produces in the mould. Another study [48] searched for a solution of a material for rapid tooling by filling epoxy with aluminium, alumina, silicon nitride and gypsum particles. The authors point out that 20% of alumina is the optimum mix for best material properties. Other articles can be found where the properties of filled resins are analysed and analytical models for predicting properties are proposed ([56], [57], [58]).

The aim of the present study is to analyse the possibility of obtaining the mould for autoclave forming by using an indirect rapid tooling technique, i.e. Joining steps two and three of figure 2.1 into a single process.
This approach takes advantage of additive layer manufacturing techniques. With respect to traditional composite tooling, the new process would eliminate the machining process to make the master model, and the mould curing process in the autoclave.
The present study is the first one to test the possibility of using rapid tooling techniques on the construction of moulds for autoclave processing of composite materials; references can in any case be found in previous works where the objective is to obtain mould inserts for plastic injection process. Plastic injection moulds are also subjected to cycles of pressure and temperature, though in a different way so the results cannot be directly transposed.
Results show that the proposed indirect tooling procedure can dramatically speed up the mould manufacturing process without losing the accuracy and expected durability of the mould. This is in accordance with results reported on [49] and [51].

1.2 Methodology

For the present study the RP machine Objet EDEN 500V was used. This system works with sealed commercial cartridges containing photosensitive resin and it was used to manufacture the mould precursor, while for the mould itself a filled thermosetting resin (epoxy) was used. Due to the complexity of the thermomechanical loads that will be acting on the mould, an extensive study on the behaviour of the candidate materials would be necessary. In fact its response to compression, bending and heat (as regards thermal expansion and creep) determine the quality of the final composite product. In this investigation a parametric experimental analysis was performed in which different percentages of different filling materials were added to epoxy resin; the quality of the mould and of the component produced was assessed. An aluminium mould was also fabricated by milling a full block with the same test geometry; the metal mould was also tested and the results serve as benchmark (Figure 2.2).

Figure 2.2: Aluminium mould

The test moulds:

A test part was designed by means of Pro/Engineer CAD software, with the purpose of obtaining a complex shape in a small surface. The perimeter of the part was extended with a border of 15 to 20 mm, forming an angle with the figure of 30° to 60°. This out-of-figure border is usual in CFRP moulds, since the laminate is required to exceed the limits of the part. The joint line between the components perimeter and the out-of-shape border was the trim line; beyond that limit the material exceeded the designed geometry and could be cut away.

From the ending of the out-of-figure border, walls were then designed to convert the shaped surface into a basin. The last step before printing the model was to thicken the surface towards the outside, so that the inside surface of the basin remained the component surface. Figure 2.3 shows the finished CAD design of the pre-mould.

The pre-mould was printed in 45 minutes, the final thickness of the pre-mould was 0.5 mm, which was the minimum printable thickness, the length and width were about 130×70 mm. The maximum dimension of a mould fabricated with this method is limited by the dimensions of the working

table; in the case of the Objet EDEN 500V machine used for this study, the printing table was 500×400×200 mm.

The solid model obtained was used as the pre-mould into which different materials were then poured to obtain the test moulds. The technique of using the RP machine directly to print a basin, where a material selected for the final mould is pourable, is similar to that reported by [51]. In their case a ZPrinter is used to produce the basin and they pour aluminium in it, but then a milling step is needed to get the exact figure.

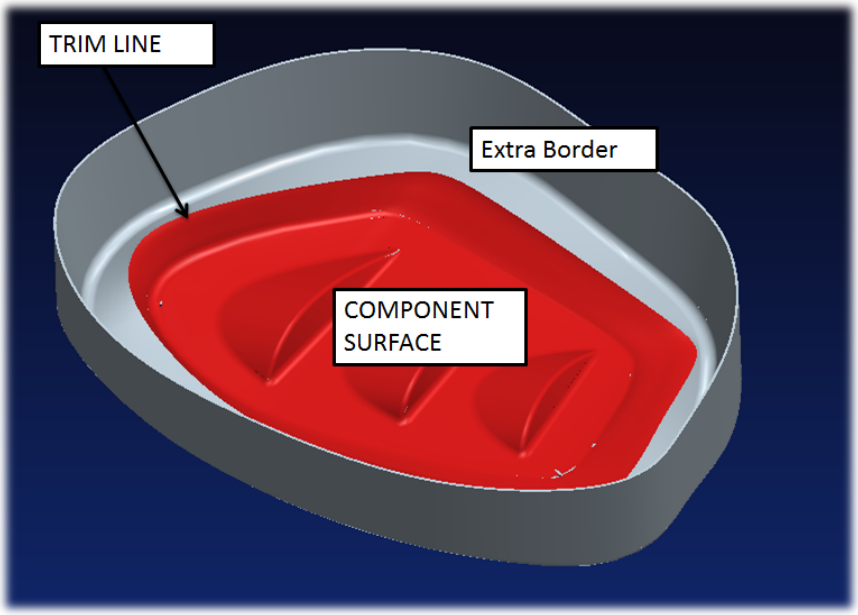

Figure 2.3: Pre-mold design

Mould materials:

Test moulds need to be able to support the autoclave conditions with the least possible deformation. For this study it was decided to use a commercial type of CFRP pre-preg with the recommended cure cycle shown in figure 2.4, where the temperature reaches 120° C and maximum pressure relative to the mould is 6 Bar.

The epoxy system selected as a matrix to fabricate the moulds had to be pourable in high volume and resistant to high temperatures, with an onset

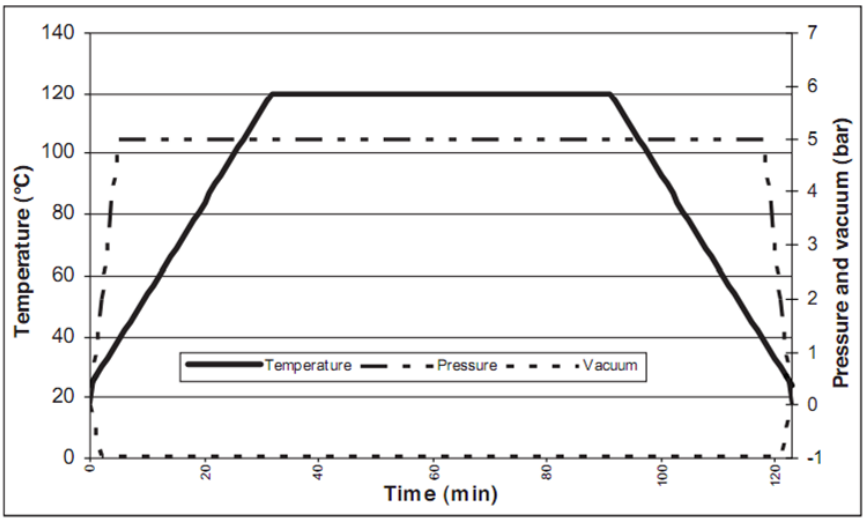

Figure 2.4: Autoclave cycle

glass transition temperature (T_g) > 130° C. This was result of the reaction between Bisphenol-A dyglycydil ether resin and an amine hardener (4,4'-Diaminodicyclohexyl methane). The T_g reported by the producer was 160°C. The matrix was filled with two kinds of fillers, aluminium powder with a diameter of 40μm and glass pearls with a diameter of 70μm, as shown in Table 2.1.

Table 2.1: Details of test moulds materials

	Filler Composition wt%	
Specimen	Aluminium powder	Glass pearls
1	70	0
2	60	0
3	50	30
4	40	30
5	30	30
6	30	0
7	0	30
8	0	0

Mould preparation:

A calibrated amount of epoxy, hardener, aluminium powder and glass pearls was divided for each mould. The procedure was to mix the epoxy and fillers, degas in a vacuum chamber, add the hardener, mix and apply vacuum again and then pour this mixture into the mould (Figure 2.5). The moulds were left to harden at room temperature for 24 hours and a post-cure process was then performed in an oven with a 20° C/hour ramp up to 160° C; at that point the temperature was maintained for 2 hours. The oven was left to cool down until the temperature reached 50° C, then the RP layer was removed taking advantage of its soft state, so it was easy to peel it out from the mould. The last step was to polish the surfaces of the mould using sandpaper, and finally to treat them with liquid chemical releaser. Figure 2.6 shows a finished mould.

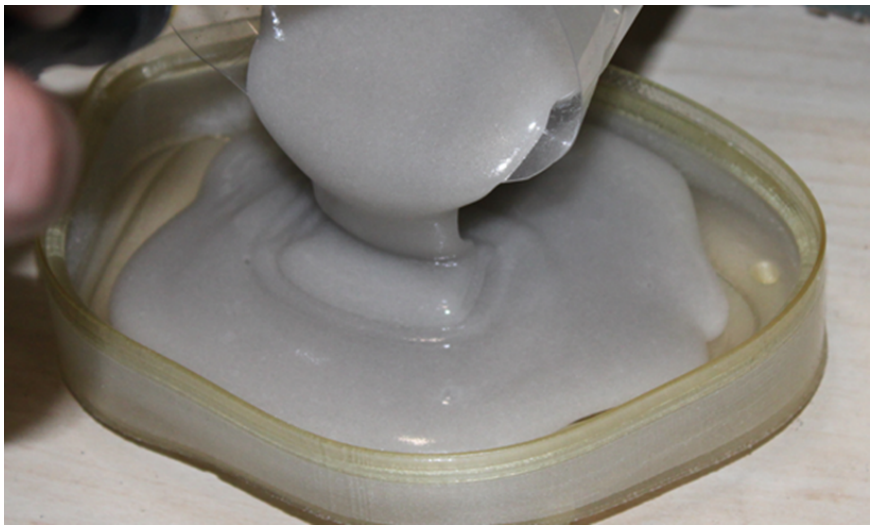

Figure 2.5: Pouring the mix inside the pre-mould

Mould testing

The FARO Laser ScanArm v3 3D scanner was used to acquire the moulds' surface and check their geometrical integrity as well as geometrical precision of the parts produced. The moulds were used in real conditions, inside a vacuum bag, submitted autoclave cycles as shown in figure 2.4. In order to

Figure 2.6: Test mould 1

save CFRP pre-pregs, instead of laminating the composite on them all the time, they were made to work in the autoclave, but without the composite, four out of five cycles; each fifth cycle a real part was manufactured. The aluminium mould was also tested to produce three parts which served as a reference.

In every case the procedure to prepare produce the parts was: 1. CFRP prepreg was laminated over the mould, over it a release film was applied and a breathing cloth was rolled to protect the bag from the moulds' sharp edges, as seen on Figure 2.7. 2. the moulds were closed inside the vacuum bags with a valve to take out the air and create the vacuum (Figure 2.8). 3. The final step of the process before the cycle was started in the autoclave was to accommodate the mould on the autoclave tray and connect the vacuum line to each valve inside the bags, as seen on figure 2.9.

After the cycle was finished, the vacuum bags were extracted from the autoclave and opened to extract the parts from the moulds in order to scan the surfaces of both moulds and parts. When the moulds worked without making parts, the only change in the procedure was in step one, where no prepreg was laminated.

The acquired 3D surfaces were analysed by means of the Geomagic Studio

Figure 2.7: Moulds prepared to with CFRP prepreg, release film and breathing cloth

scanning and reverse engineering software .
The different scanned point clouds were compared to each other using the 3D Compare feature, which calculates the shortest distance of the test model to any point in the reference. The precision of the 3D compare feature was checked before starting the process by comparing 24 point clouds of the same part scanned in different light conditions. As a result of this pretest, it was concluded that the distance between the points of the parts being compared has a normal distribution, centred on zero $(\mu^- + \mu^+)/2 = 0.00255mm$ and standard deviation $\sigma = 0.0271mm$. The average deviation was $(|\mu^-| + |\mu^+|)/2 = 0.0201mm$.

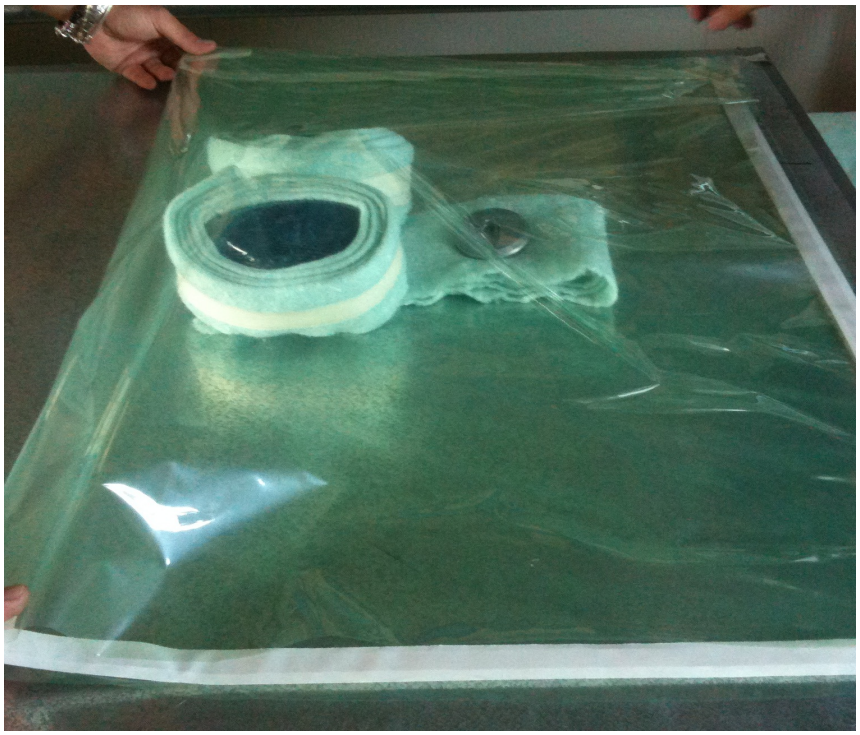

Figure 2.8: Mould being closed inside the vacuum bag

1.3 Results

Moulding process:

The most critical part of the proposed moulding process is the initial exothermic chemical reaction of the filled resin while it is in a liquid state. It is at this part of the process that the pre-mould material (Fullcure 720), being thin and having a low T_g ($\sim 45^\circ$ C), could deform the original design. The polymerization reaction at room temperature allows solidification of the resin, but in order to increase the heat resistance a post curing of the resin is needed. The post-curing was done up to 140° C, a temperature much higher than the T_g of Fullcure, but since the viscosity of the resin remains high enough during cross linking, it does not continue causing deformation.
The deviation effect is more visible in the centre and edges of the part. The extents of the deformation caused by this whole process can be seen in figure 2.10. It may be possible to reduce this deformation by using a more resistant material to produce the pre-mould basin, or by reinforcing the pre-mould

Figure 2.9: Moulds entering the autoclave

with a coating.

Mould performance:

By comparing the scanned models of the subsequent parts to the scan of the original mould it was possible to see the performance and the deformation throughout the cycles. Figures 2.12 and 2.14 show the results of the 3D compare feature for the first four parts of specimens 8 (no filler content) and 1 (Aluminium powder wt% 70). Figures 2.13 and 2.15 show accumulated percentages of points between distances of -0.5 and +0.5 mm for specimens 8 and 1. The six curves correspond to the parts compared to the virgin mould (dashed line), the virgin mould compared to the designed model (soft grey line) and the mould after 20 cycles compared to the virgin mould (full black line). Figures 2.16 and 2.17 show the results obtained with the aluminium mould.

As can be seen, the parts manufactured with test mould 1 are similar in terms of geometrical precision to those obtained with the aluminium mould. Figure 2.11 shows a finished component; notice that the superficial quality is

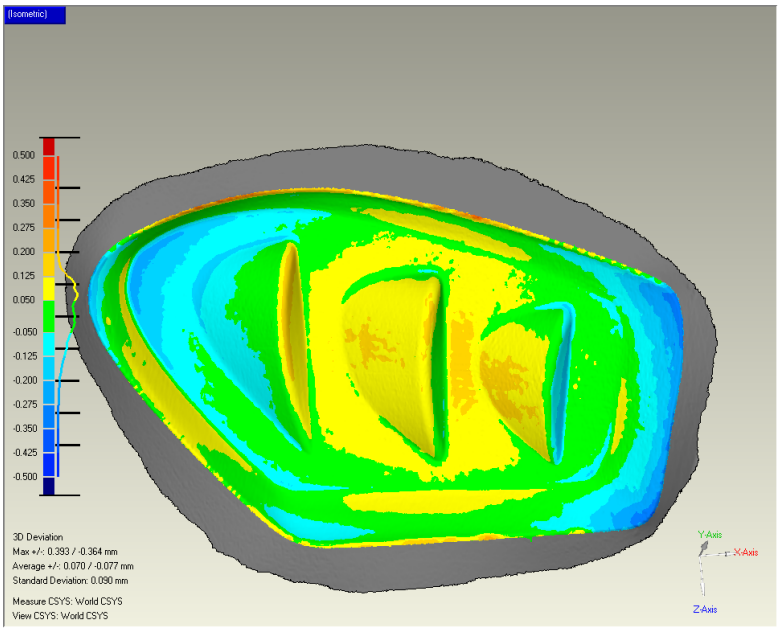

Figure 2.10: 3D Comparison of the finished mould and the designed part model

very smooth. To obtain this result, the surface of the mould was treated with sand paper. When the surface of the mould remained untouched, the parts came out with visible lines caused by the layered structure of the pre-mould, too small to be seen by the laser scanner but clear to the naked eye. Being able to *clean* the layer lines from the moulds without modifying too much the geometry was possible because the RP machine used (EDEN 500V) prints ultra thin layers ($16\mu m$). In all cases the precision was quite favourable taking into consideration that reference [45] reports similar results on the injection moulding process, with deviations of up to 0.076 mm. Also reference [50] reports geometrical variations and they also work with the injection moulding process, but in their case the maximum deviations are much bigger, up to 0.94mm on a 36.2 mm quote.

It is worth noting that the filler content allowed the mould to produce constant quality parts throughout the cycles, while the unfilled test mould suffered permanent deformation on each cycle, thus producing dissimilar parts.

The test were stopped after 20 cycles for test moulds 5, 6 and 7. Tests continued on specimens 1, 2, 4 and 8. While test moulds 1, 2 and 4 contin-

Figure 2.11: Finished part

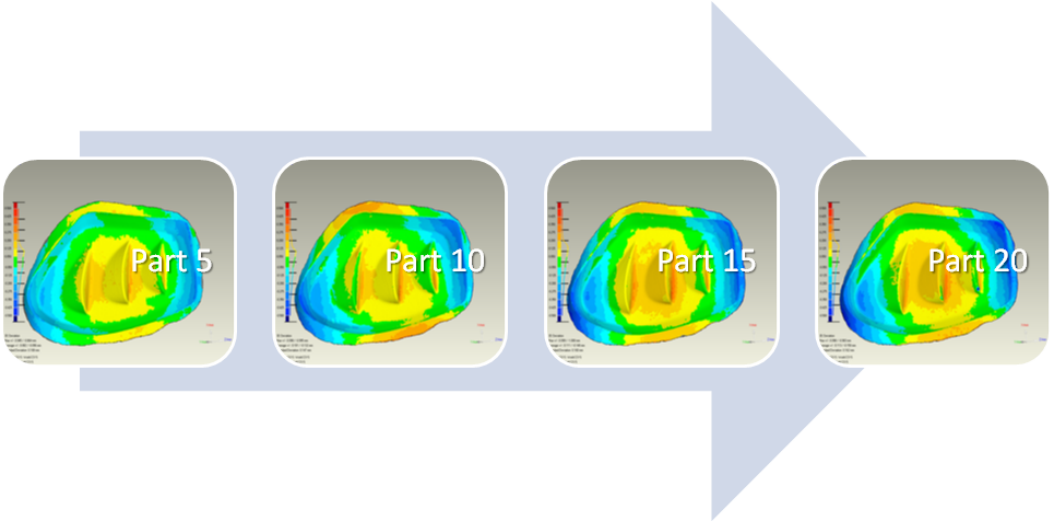

Figure 2.12: 3D compare evolution for mould 8 (No filler content)

ued producing parts with constant geometrical quality, specimen 8 continued to deform until it broke on a side after 30 cycles (6 parts), figure 2.18; the rest of the tests were stopped after reaching 50 cycles. The full results for the average distance of the parts from the virgin mould, using the average of the mean distance of the points for each specimen $\frac{\sum_{i=1}^{n}(|\mu_i^-|+|\mu_i^+|)/2}{n}$, are

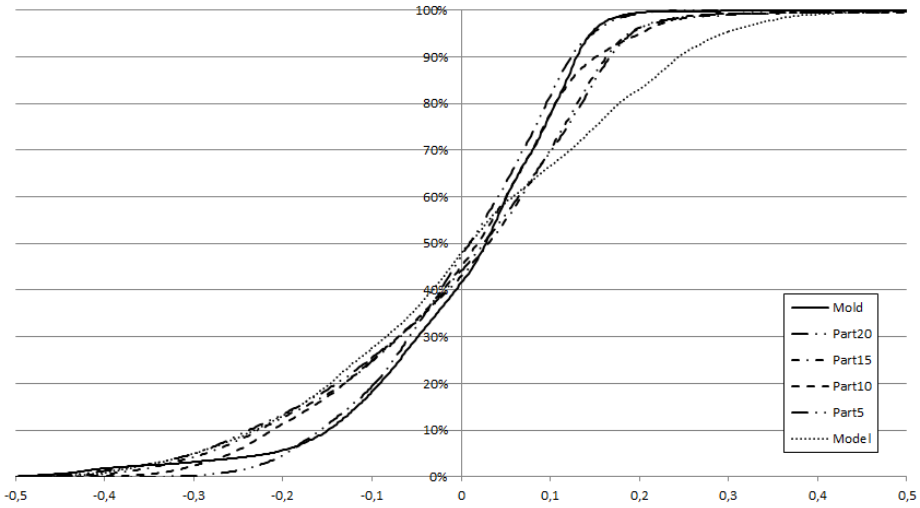

Figure 2.13: Deviation analysis for mould 8

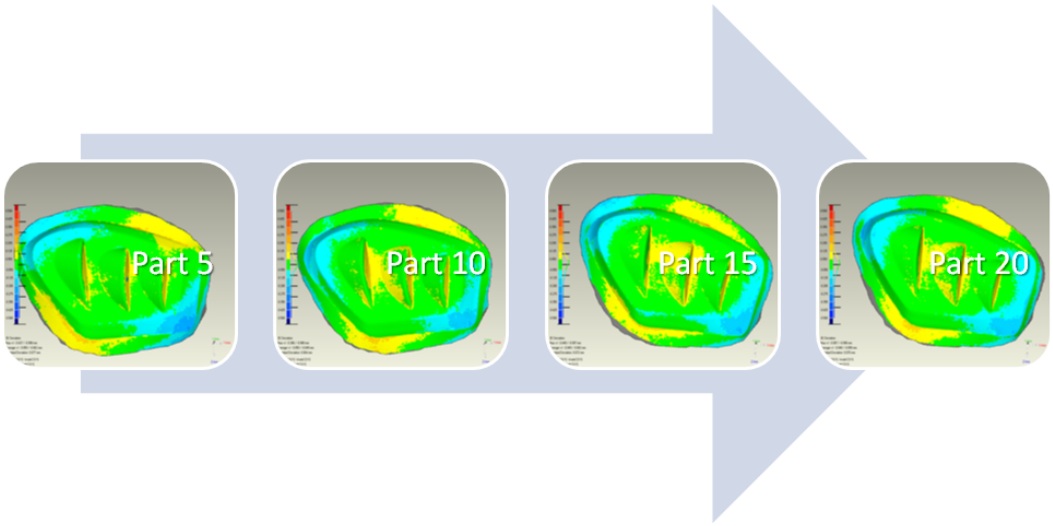

Figure 2.14: 3D compare evolution for mould 1 (Filler content 70% wt)

represented in Figure 2.19.

1.4 Conclusion

An indirect rapid tooling technique was used and tested in a parametric experimental test.

The tooling material was always a filled epoxy resin. Results were analysed

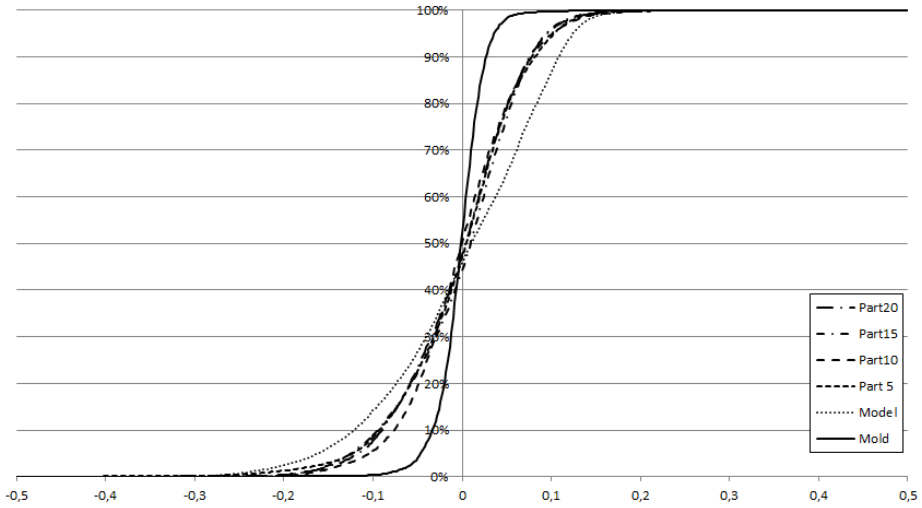

Figure 2.15: Deviation analysis for mould 1

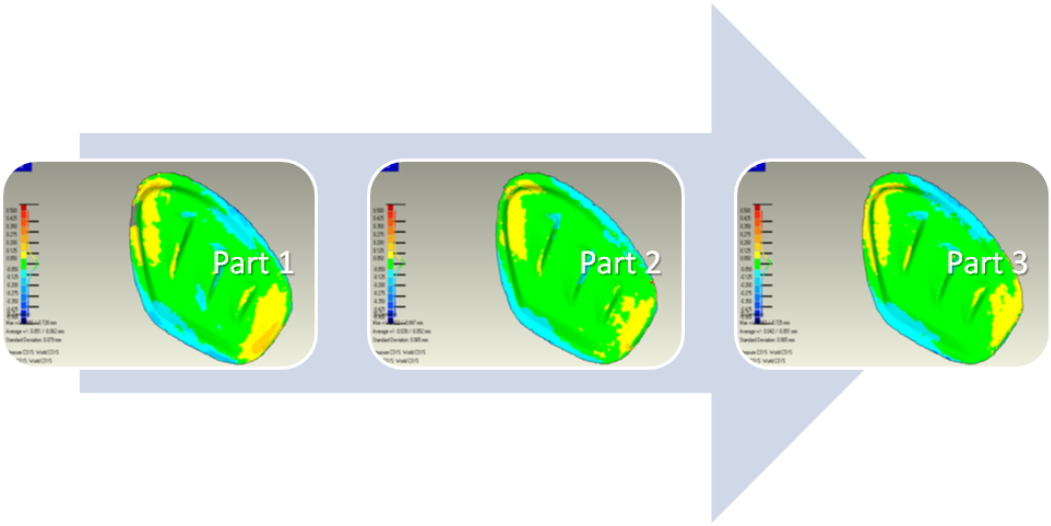

Figure 2.16: Average distance of 3 parts produced with the aluminium mould

using a 3D scanner and comparing the successive point clouds. It was possible to see how the filler allowed the mould to keep its geometrical integrity, producing good quality parts. The results show that moulds produced using this technique and high filler content can withstand several autoclave cycles without changing their shape, producing good quality parts. Further investigations should focus on understanding and optimizing the process variables as thermal cycles and deformation due to thermal expansion when using these

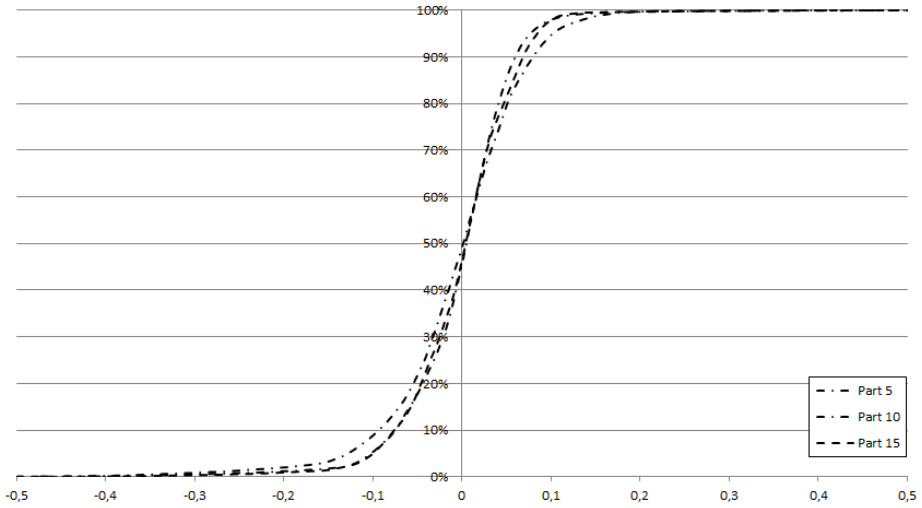

Figure 2.17: Deviation analysis for aluminium mould

Figure 2.18: Mould 8 after 30 cycles, chip breakage can be seen on a side

materials.

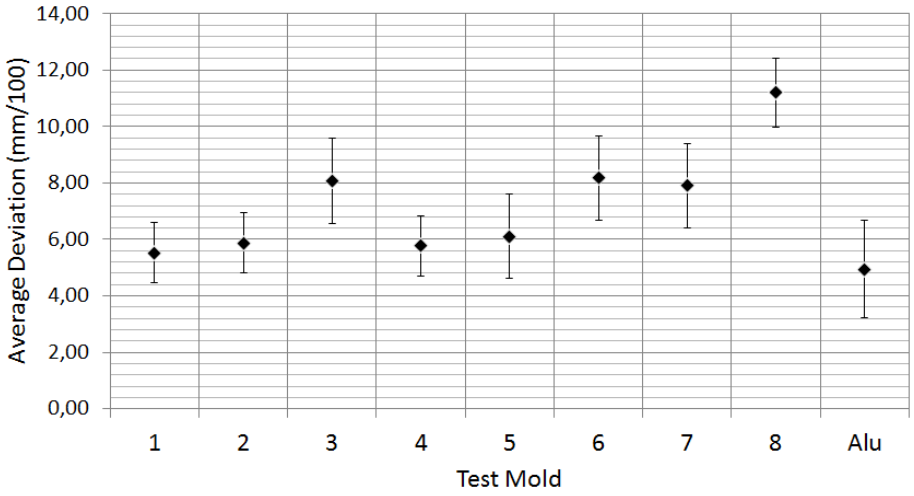

Figure 2.19: Average distance of the parts from each corresponding mould. The average is calculated using all the data available for each mould, the error bar was calculated from this data using the ANOVA method

2 THICK COMPOSITES CURED IN AUTOCLAVE

KINETICS AND MODELLING OF CURING BEHAVIOUR FOR TWO DIFFERENT PREPREGS BASED ON THE SAME EPOXY PRECURSOR

2.1 Introduction

Though in luxury industry CFRP parts often play just an aesthetic role, their main applications are still as structural materials. CFRP parts are generally produced as relatively thin objects, where layers of fibres and resin precursors are stuck one on the other: playing on the composition of the layers, orientation of the fibres and on the stacking sequence, physical and mechanical properties can be controlled and tuned for specific applications.
When the design of the final object is particularly challenging, or the dimension is quite large, the best choice for producing CFRP is hand lay-up of pre-impregnated fabrics that are finally consolidated by applying a temperature and pressure cycle to the laminate in autoclave. When too many layers are stuck, though the composite can reach outstanding properties, problems arise in the manufacturing of the parts [59]. Literature does not report a unique classification of what a thick composite is, but Secord et al. [60] provided clear definition as following: "parts that have large unfavourable temperature overshoots are classified as *thick*, while parts that have little or no overshoot during cure are classified as *thin*". The latter description claims that separation of a CFRM into *thick* or *thin* class depends just on how much the geometry of the object affects its final quality. Indeed, owing to the exothermicity of the curing reaction in epoxy resins and to poor thermal conductivity across the section of single layer (due to the anisotropy of thermal conductivity in prepregs, which is high along the fibre axis, but definitely scarce perpendicularly to it) when thickness exceeds few millimetres overheating of the inner layers may happen [59]. As a result thermal stresses, shape distortion and resin degradation may occur in the final product [61] [62]. Objects that are particularly prone to develop overheating and thus suffer for these defects are considered *thick composites*. Additional problems might arise in the work up of big CFRP objects, where not only the thickness

section is increased, but the overall dimension of the final part extends over a meter scale. In this case the hand lay-up of the whole part is particularly time-requiring and the ageing of raw materials during work up might affect the kinetics of the curing reaction [63]. Additionally the curing process in autoclave is far from ideal laboratory condition, thus making thick composite industrial production an actual challenge [59]. In this context, a good knowledge of the thermal curing behaviour of the resin prepreg is of paramount importance to design a full production and curing cycle for a thick composite object avoiding defects that might compromise the final structural properties [64]. Modelling of the complex phenomena occurring in the thick composite production may provide an estimation of what is occurring during the production of parts, helping to find the best curing cycle conditions. When such a complex object has to be produced, the choice of raw materials is also important: while fibre arrangement may be varied in different prepregs, at least dealing with the same kind of resin precursor should help, in principle, simplifying the design.

In the present work a case-study is presented, where the behaviour of prepregs intended for the industrial production of a thick part (about 35 mm cross section) for primary structural application is investigated. The aim of the work is to highlight the critical parameters to be considered in the optimization of the curing cycle. The final product is meant to be composed of two different prepregs based on the same resin, but obtained with different work-up methodologies and with a different fibre arrangement. The study will first take into account the ageing of the raw materials. Then the experimental determination of the kinetic curing behaviour of the two different prepregs will provide parameters to be used for independently modelling the curing process for the two raw materials, highlighting possible differences that may affect the part production. Comparison of the two models will provide useful hints for the set-up of a convenient and flexible curing cycle, that takes into account number of layers, type and ageing state of raw prepregs.

2.2 Experimental

The materials used in this work are commercial carbon fibre/epoxy prepregs, both provided by ELANTAS: in the two analysed prepregs fibres are arranged either as a woven 2 twill fabric with $600 g/m^2$ fibre weight per unit area or as unidirectional fibres with $300 g/m^2$ fibre weight per unit area. In both cases the resin content is $37 wt\%$. Prepregs based on woven fibres will be named as PP-T2 while prepregs containing unidirectional fibres will be named as PP-UD.
DSC measurements were carried out on a TA Instruments Q2000 DSC Modulated apparatus equipped with RCS cooling system. Every sample ($10 - 15 mg$) was heated from $-50°C$ to $250°C$ twice at $10°C/min$ in nitrogen atmosphere, with an intermediate cooling run carried out at $20°C/min$. Isothermal curing scans were carried out by inserting the sample ($10 - 15 mg$) in the DSC furnace cell, pre-heated to the desired isothermal curing temperature (T_{iso} =90, 100, 110, 120, 130, 140$°C$) and kept at that temperature for a given amount of time, ranging from 60' up to 480'. Then the sample was quenched to $0°C$ and a scan was carried out up to $200°C$ at $10°C/min$.
The 2D-mesh used for the modelling of the cure dynamics was prepared with Hypermesh software: it consisted of 18758 TRI-3 elements and 9882 nodes, representing the cross section of the component at its thickest section ($35 mm$) and the mould used during the autoclave curing. The thickness used for this model is also well representative of the average thickness of the object to be produced. Worth noticing is also that, according to production requirements, the mould is made of carbon fibre/epoxy resin composite too. For the simulation the Curing module of PAM-RTM was used, a commercial software developed by ESI-Group which can simulate the curing process with a finite element approach [125]. The mesh was divided into two zones, namely *the mould* and *the component*. A temperature profile was fixed at the inner and outer layers of nodes, representing the inside bagging film and the outside surface of the mould, both in contact with the air inside the autoclave. Some standard characteristic values such as the density, thermal conductivity and specific heat capacity for each material involved were obtained from literature [138] [67], while the cure kinetics model and other reaction parameters such as reaction enthalpy were obtained from the analysis of DSC measurements.

Figure 2.20 shows a section of the mesh where the green arrows represent the transversal direction, for which the interlaminar thermal conductivity was defined as $0.4W/mK$. The directions orthogonal to the green arrows in the figure (and parallel to the free edges of the mesh) were set as the in-plane direction, with an effective thermal conductivity of $0.8W/mK$. The specific heat was set to $1200J/KgK$ for the resin and $710J/KgK$ for the fibres.

The temperature cycle defined for the simulations consisted of a first ramp

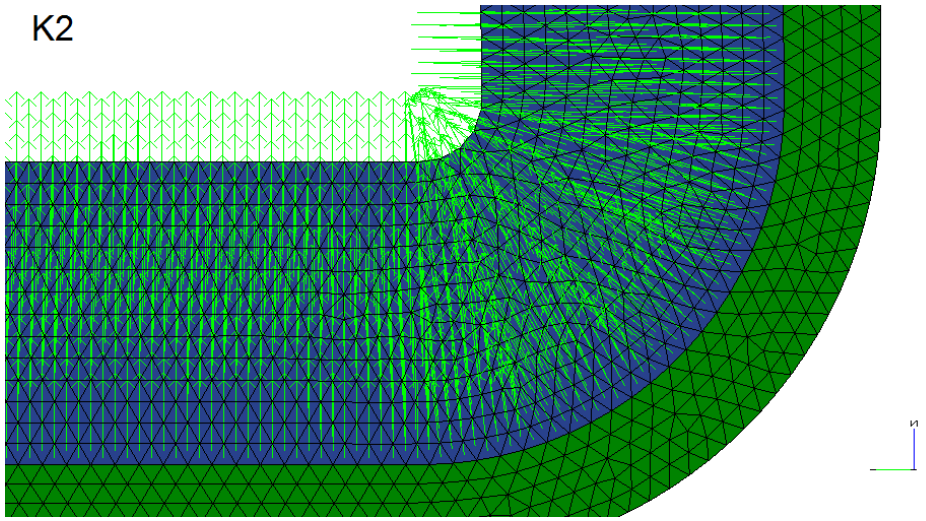

Figure 2.20: Detail of the mesh: the green vectors show the transversal direction (K2), where interlaminar heat transfer properties were defined. K1 direction was defined orthogonal to K2, parallel to the sides of the mesh. The picture shows also the two components considered for the simulation: blue elements are part of the composite to be cured and green ones are part of the mould.

at $2.5°C/min$ to take the temperature up to $100°C$, a 40 minutes hold, followed by a new 30 minutes increase of the temperature up to $120°C$, where a new hold was set for another 80 minutes. The time step of the simulation was defined as two seconds (number of steps = total simulated time/2).

2.3 Results and Discussion

Lay up of commercial prepregs is a simple approach for obtaining thick and complex carbon fibre reinforced parts. Prepregs are tacky, so they can easily be placed in moulds, even in complex shapes, and they are quite tolerant to room temperature conditions. Moreover, layers can be stack using a different fibre orientation and arrangement, i.e. also different kind of prepregs, thus providing a reinforcing effect that can be tuned on different region requirements in the same object. If different kind of prepregs are used for the same part, they must be chosen that can undergo a common curing cycle without falling in those earlier cited overheating critical conditions that may detrimentally affect the final object. In the present case the part to be produced has a thickness of about $35mm$ and one dimension exceeds hundreds of cm: as a matter of fact the work up procedure might take up to three weeks from the moment the first prepregs are taken out of freezing cell (storage at $-18°C$) for the cutting stage. Therefore, it has to be taken into account that time required for the working up might somehow affect the properties of the crude materials. Two different commercial prepregs are used for this case-study: they are made up of the same epoxy resin precursor and different types of fabric (either 2x2 twill woven, PP-T2, or unidirectional, PP-UD, mats) hence, at least in principle, the way ageing, and further curing, affects prepreg performance should be the same. However, the difference between PP-UD and PP-T2 is not only in the fibre arrangement, but also in the prepreg production technique: PP-T2 is obtained via solvent impregnation while PP-UD by hot melt procedure. Hence, an initial assessment of the prepreg condition as a function of time was carried out by DSC measurements.

Every DSC shows a low temperature T_g (below RT) and an exothermic peak in the fist scan, while the second scan, carried out upon reaching $250°C$ in the first one and cooling down at a controlled cooling rate, shows only a high-T_g, well above RT. In Figure 2.21 the first DSC scans of pristine PP-UD and PP-T2 are reported, focusing on exotherm peaks that are attributed to heat evolved upon the curing reaction proceeding. The PP-UD thermogram shows an exotherm whose peak temperature (T_{peak}) is centred around at $147°C$: the signal aspect - including the process enthalpy - and position stay quite invariant with time. PP-T2, on the contrary, shows a narrower exothermal

transition, that is centred at a higher temperature than PP-UD, with T_{peak} that is positioned around $153°C$ for the *as received* material: position of the peak is practically invariant with time passing, while enthalpy of transition are more scattered than in PP-UD, though values does not follow a specific trend. This behaviour might be ascribed to the higher inhomogeneity that characterizes the prepreg with the higher weight per unit area ($600g/m^2$ vs. $300g/m^2$). Figure 2.22 A-B shows the trend in T_g obtained during the first DSC scan for crude prepregs and for the same materials upon heating up to $250°C$ in the instrument furnace. It is clearly observed that, irrespective of leaving the samples at RT or keeping them at $5°C$, no significant differences are observed for PP-UD prepregs (Figure 2.22 A), whether analysed *as received* or after a 4 months storage time in a freezing cell ($-18°C$). The PP-T2 prepregs, on the contrary show an increasing trend in T_g values for the crude prepregs when kept at RT (black symbols in Figure 2.22 B). This is an indication that the uncured resin precursor tends to slowly polymerize in these conditions, i.e. in the processing condition, this phenomenon being more severe after 4 months ageing (open vs. full symbols). Figure 2.22 B also shows that early undesired polymerization can be prevented by lowering T at $5°C$ (red symbols in Figure 2.22), where no changes in the T_g trend is displayed. While T_g of the crude prepreg increases when the samples are kept at RT, the corresponding T_g of the final product upon DSC-curing decreases with a roughly opposite trend. Once more 4 months ageing at $-18°C$ worsen the situation, lowering the T_g attainable in DSC curing condition of about $8 - 15°C$. Figure 2.22 B shows that ageing has also consequences on cured samples whose crude prepregs are kept at $5°C$: though no significant change in the crude material T_g was observed, the maximum attainable T_g - at least upon thermal treatment in the DSC furnace - is even $15°C$ lower than the fresh, non-stored material. Taking into account that T_g values obtained in the reported DSC scans (see applied condition in the Experimental Section) are definitely not representative of what is the real attainable T_g in an industrial curing cycle, and that anyway $5°C$ temperature cannot be easily obtained in the clean rooms where hand lay-up is carried out, the changes shown by PP-T2 with time are a sign that ageing of the crude materials might be a crucial issue when designing the industrial production process of a big thick

part. Indeed, given the fact that the usual shelf life of prepregs, as stated by the supplier, is 12 months at $-18°C$ and 4 weeks at RT, it has to be considered that within this span of time properties of the raw materials might change: in order to obtain the best possible performance in the final object, the curing cycle has thus to be carefully verified and tuned according to specific work up requirements. Accordingly, further studies are thus carried out on 3 weeks aged resins upon storing at $5°C$, in order to better reproduce the actual curing conditions.

With the aim of avoiding overheating effect upon curing, due to the reac-

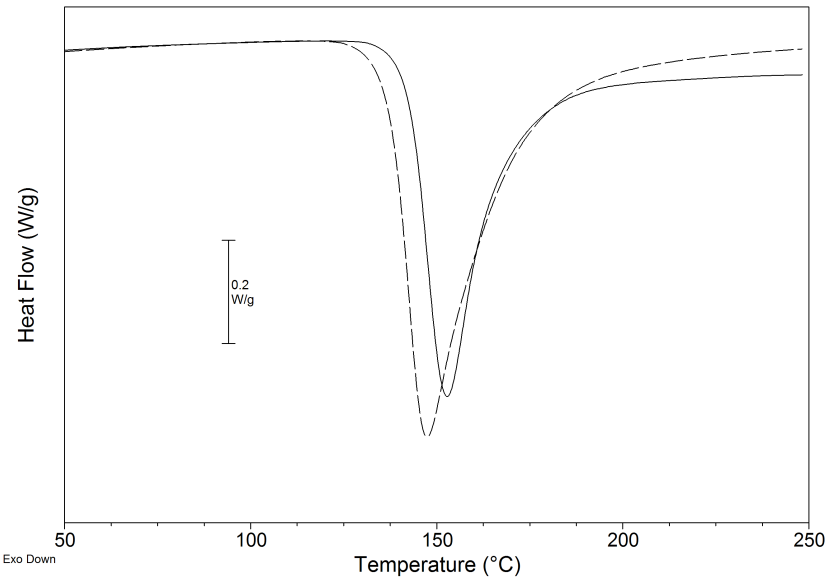

Figure 2.21: First DSC scan of pristine PP-T2 (full line) and PP-UD (dashed line) as received from the producer. The temperature range is focused on the exotherm peak area.

tion exotherm, the curing cycle must be designed in order to slowly heat up the object and allow the heat to diffuse all along before the reaction begins. Therefore, the knowledge of the reaction kinetics is of fundamental importance to provide reliable data for simulations to be carried out. Kinetics modelling of prepregs curing reactions is not easy to evaluate owing to the

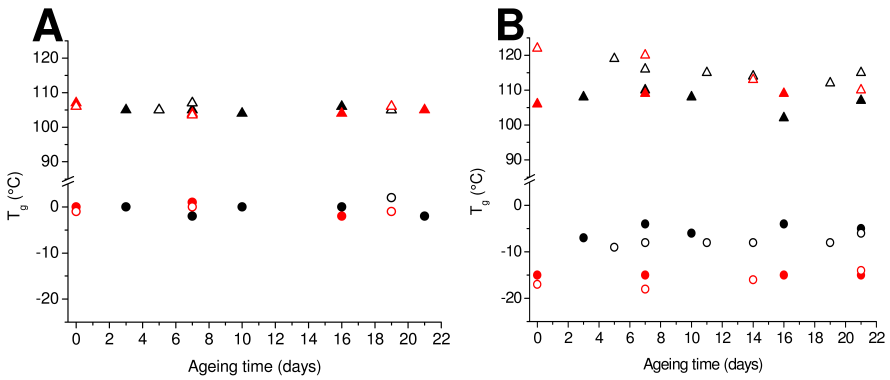

Figure 2.22: T_g evolution of crude (I scan, circles) and cured (II scan, triangles) prepregs as a function of time out of the freezing cell for PP-UD (A) and PP-T2 (B) prepregs. Prepregs were taken out of the freezing cell ($-18°C$) and either kept at Room Temperature during the analysis time span (black symbols) or stored at $5°C$ until analysis is carried out (red symbols). Open symbols refer to prepregs analyzed when received, filled symbols refer to materials analyzed after 4 months storage time at $-18°C$.

many concomitant reactions occurring contemporary and/or in sequence on several co-monomers and initiators, to the possible presence of additive or accelerators and to the intrinsic difficulty of monitoring such a complex system that ends up in an insoluble network [68] [69] [70]. Moreover, in prepregs the situation is made even more complex by the influence that different fibres might have, depending on surface chemistry and sizing treatments [[68] [71] [72] [73] [74]. During the present work, the procedure described in chapter 1 was applied for both prepregs in order to obtain the parameters of the Kamal-Sourour model, described here by equation 2.1:

$$\frac{d\alpha}{dt} = k(T) \cdot \alpha^m \cdot (1-\alpha)^n \tag{2.1}$$

Where $\frac{d\alpha}{dt}$ is the reaction rate, α is the degree of cure, A is the pre-exponential factor, E_a is the apparent activation energy, R is the gas constant, and T is the absolute temperature m and n are the reaction orders. Owing to the differences observed in dynamic DSC scans between the two investigated prepregs

(Figure 2.21), kinetics of both PP-UD and PP-T2 are studied, though in principle no difference was expected. AS explained before, the study takes into account the isothermal curing of a sample prepreg at different temperature, in this case between 90 and 140°C. In each isotherm thermogram a single exotherm is observed, the peak maximum being delayed as the T_{iso} decreases, while the enthalpy stays invariant around $110 J/g$ for all the experiments for both PP-UD and PP-T2. As previously stated, form DSC thermograms it is possible to plot α as a function of time at different T_{iso}. From α vs. t plot, isoconversional curves can be derived, by calculation of the time t required for reaching the same conversion when reaction is carried out isothermally at different temperatures (T_{iso}). A linear correlation is established between Lnt and $1/T_{iso}$, where the slope of the obtained interpolation line represents Ea/R and is thus applied to calculate apparent activation energy E_a values, which are also reported in Table 2.2. Apparent E_a is higher for PP-T2, that indeed requires a higher temperature to start reacting, accordingly to the exotherm profiles previously displayed in Figure 2.21. Since the two prepregs are composed of the same resin precursor, the differences observed both in the dynamic DSC scan and in the calculated E_a values resulting from isothermal measurements can be tentatively ascribed to the lack of some reactive groups in the PP-T2 prepregs, lost during the solvent impregnation process. During the prepreg production, the B-staging might have been pushed slightly further in PP-T2 solvent impregnation than in the PP-UD hot melt process [83], causing the reaction of the low E_a functional groups, and inducing the apparent activation energy - that is not representative of a single occurring processes, but it gives a rough estimation of the energy required to activate the sum of all the contemporary processes occurring upon curing as if they were a single autocatalytic reaction [84] - to raise. Though a partial contribution to the curing differences observed might also be brought in by the possible differences in fibres used for prepregs preparation, since fibre sizing and intrinsic surface properties might affect the curing process, no such a strong effect has been reported in the literature for carbon fibres on the epoxy resin curing [85]. Hence the impact on the final modification of the E_a is neglected.

In order to calculate the cure rate profiles ($d\alpha/dt$) as a function of time and

Table 2.2: Experimental DSC results and kinetics parameters evaluation obtained by DSC isothermal scans

T_{iso} (°C)	DHT^a_{iso} (J/g))		t^a_{peak}(min)		m^b		n^b		E^c_a (KJ/mol)	
	PP-UD	PP-T2	PP-UD	PP-T2	PP-UD	PP-T2	PP-UD	PP-T2	PP-UD	PP-T2
90	106	109	52.8	70.7	0.35	0.78	0.62	1.14		
100	101	113	29.1	34.2	0.51	0.95	1.01	1.73		
110	100	106	13.4	14.2	0.82	0.42	2.04	0.79	80.6	86.2
120	111	109	6.3	7.2	0.51	0.51	1.45	1.40		
130	120	115	3.2	3.5	0.56	0.51	2.02	1.77		
140	109	110	1.5	1.7	0.60	0.54	2.65	2.49		

[a] Calculated from DSC isothermal scan.
[b] Calculated upon fitting of DSC experimental results, according to Kamal - Sourour autocatalytic model reported in eq 2.1.
[c] Calculated from interpolation of isoconversional data derived from experimental isothermal DSC scans. The value reported represents the average of the values calculated for conversion α =0.10, 0.20, 0.30, 0.40, 0.50, 0.60, and 0.70.

of degree of cure α derivative of the α vs. t plot is calculated: those profiles were used for obtaining the m and n values reported in Table 2.2. This was done with a regression approach on equation 2.2, as explained in chapter 1 obtained by applying logarithm to equation 2.1:

$$Ln(\frac{d\alpha}{dt}) = Ln(k(T)) + m \cdot Ln(\alpha) + n \cdot Ln(1-\alpha) \tag{2.2}$$

For each isothermal experiment, $Ln(k(T))$, m and n could be treated as constants, this permitted the construction of a multiple regression linear model of the form $Y = A + B \cdot X_1 + C \cdot X_2$. Figures 2.23 and 2.24 show experimental vs. fitted values.

A linear fit of m and n parameters was obtained in order to get a single expression of the cure model, which could be introduced in the simulation software for modelling the curing behaviour of prepregs. The software requires setting one unique cure reaction for all the resin involved in the simulation and this is the reason why the simulation was done for each resin independently.

It is interesting to analyse the results from two perspectives: the instant tem-

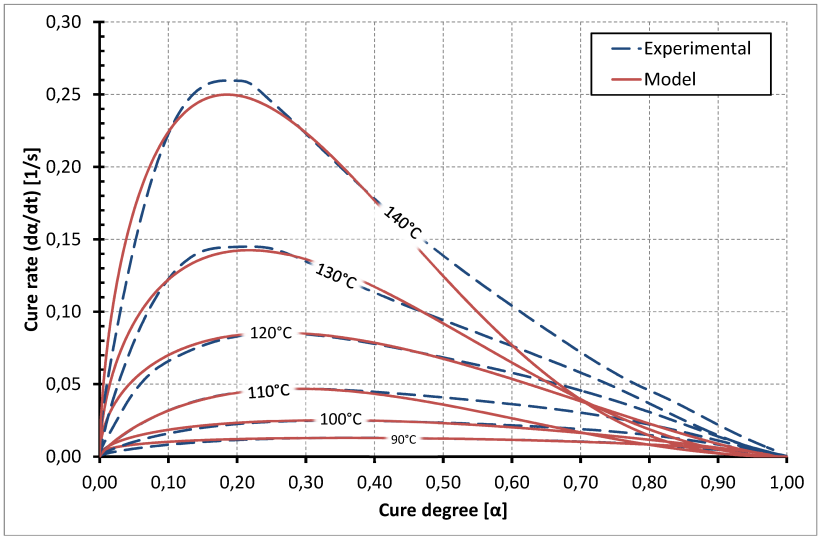

Figure 2.23: Isothermal reaction rate of PP-UD as a function of the cure degree, dashed blue lines show experimental results and red full lines show the data obtained from the model.

perature profile of the component indicates how the exotherm of the reaction introduces heat to the system, deviating the cure cycle from the designed one; the instant cure degree indicates how the curing of the part develops, this is pretty much correlated to the internal tensions developed during this stage, and could end up in deformations due to local shrinkage differences.
The graph in figure 2.25 shows the temperature and degree of cure (α) evolution vs. time for both the analysed prepregs PP-T2 and PP-UD. The curve was drawn for a hypothetical sensor at one half of the components thickness at one of the angles. Though the simulation was run for a longer time, only the first 7000 seconds are shown, since this is the time span where the most interesting reaction phenomena take place. Given the solid line as the imposed thermal curing profile, both prepregs show a slight delay in the beginning; the delay is given by the heat transfer resistance properties of the prepreg components (resin and fibres) and surrounding materials (mould and bag). Since heat transfer properties were taken from the literature for analo-

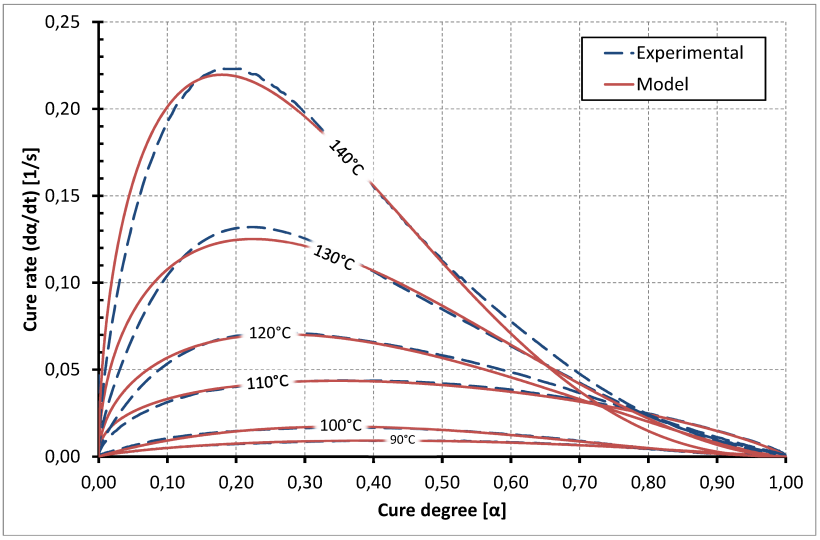

Figure 2.24: Isothermal reaction rate of PP-T2 as a function of the cure degree, dashed blue lines show experimental results while red full lines show the data obtained from the model.

gous materials, and not experimentally determined on the actually used ones, simulated maps can only provide a fine description of phenomena but not the very exact behaviour. This means that, though the estimation of the heat produced upon reaction is well fitted, the heat transport across the section of the material might be slightly different, affecting the maxima position of the overheat phenomena as a function of curing time. As the temperature increases, and slightly before the holding segment is reached, the reaction starts to take place and, owing to its exothermic character, it adds heat to the system. The faster the reaction takes place, the more heat it adds, thus at a certain point the actual sample temperature exceeds the autoclave temperature, causing a further increase of the reaction rate. The temperature peak is found where the reaction starts to slow down, before arriving at the complete conversion, where the temperature tends again toward the autoclave external value. In Figure 2.25 it is interesting to note that peaks reached by the internal temperature of the theoretical composite made by 100% of one of the two

prepregs (1 and 2 for PP-UD and PP-T2 respectively) do not occur at the same time. The PP-UD reaction is slightly more violent, developing a maximum temperature of $408K$ compared to the $403K$ developed when applying the same cure cycle on the PP-T2. In the condition used for the simulation, the difference between the two peaks is about 18 minutes. Of course, the centre of the thick sample is the region most affected by exotherm effects, but the different reactivity of the two samples can be observed in almost all the sample's section. Figure 2.26 and 2.27 are snapshots of the simulation showing the temperature and degree of cure maps for the cross section of the simulated object based on the two different prepregs. Snapshot are taken at two different times, corresponding to the two different maxima in the temperature profile of the hypothetical central sensor, as outlined in Figure 2.25. Figure 2.26 clearly shows that PP-T2 temperature profile is not only characterized by a delayed temperature boost with respect to PP-UD, as expected by Figure 2.25, but when the reaction starts the overheating effect affects a minor region, as shown by the smaller red area. Figure 2.27, which makes an analogous treatment of the data showing the cure degree vs. time, shows that the PP-T2 reaction is not even started when the PP-UD has already reached 50% conversion; when the PP-T2 reaches a similar point PP-UD is already towards reaction completion. The cure degree is correlated to the material shrinkage, and this results evidence that when the two prepregs, containing unidirectionally aligned fibres and 2x2 twill woven fabric, are mixed together in the same component, the PP-UD might possibly start shrinking earlier, thus affecting also the PP-T2 alignment and increasing the internal residual stresses. The observed difference in the development of the curing for the two different prepregs raises also some problem in the chemical homogeneity of the final material. On the contrary, the delay in the reaction that the PP-T2 layers may introduce inside a thick complex object made up of alternate layers of PP-UD and PP-T2, may help reducing the overall overheating effect, since when PP-UD is already reacting, PP-T2 is not still contributing to heat development. Anyway, the quite intense overheating effect observed for PP-UD could be also possibly reduced by designing a longer and smoother curing cycle, although this would increase the production time and the final costs of the industrial process. In order to obtain an optimization, further

simulation tests should be carried out in order to understand how much the internal stresses could affect the final dimensions and mechanical properties of the produced component.

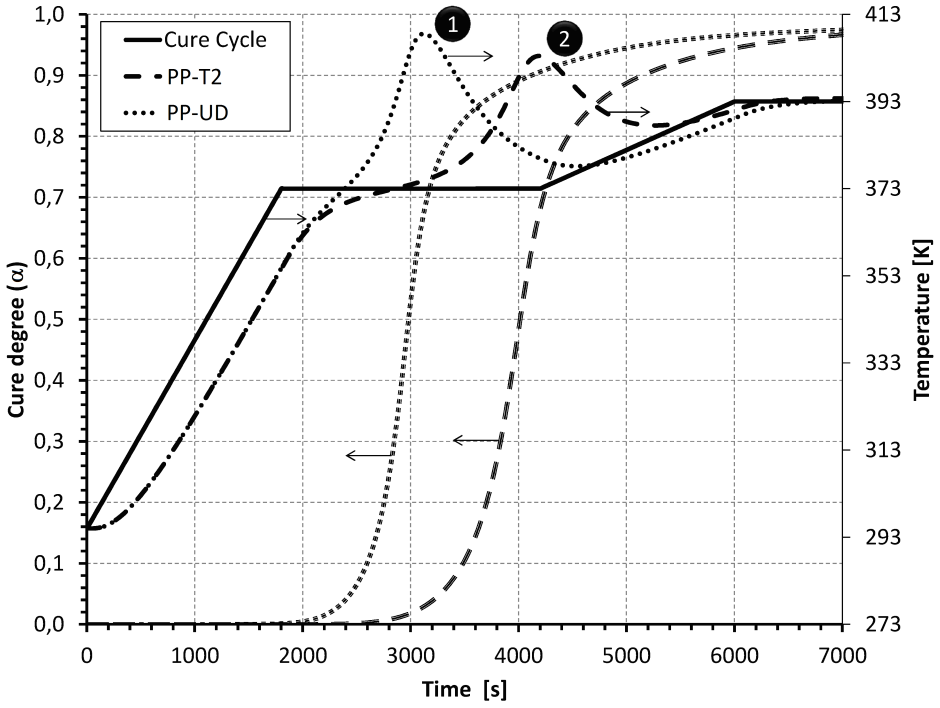

Figure 2.25: Results obtained from finite element process simulation, temperature and cure degree are shown for the mid-section point of the mesh, at one of the components elbow, when the material is the PP-UD (dotted lines) or the PP-T2. The full line shows the cure cycle applied on both cases.

2.4 Conclusion

The present section analyses independently two different prepregs that are intended to be used together for the production of a thick composite object. The two materials show a different ageing trend, with PP-UD (obtained via hot melt process) that is almost invariant with time, while PP-T2 (obtained via solvent impregnation process), when stored at RT tends to slowly react, thus lowering with time the T_g values reached in the final composite object after curing. Though raw materials are still well within their shelf life, and

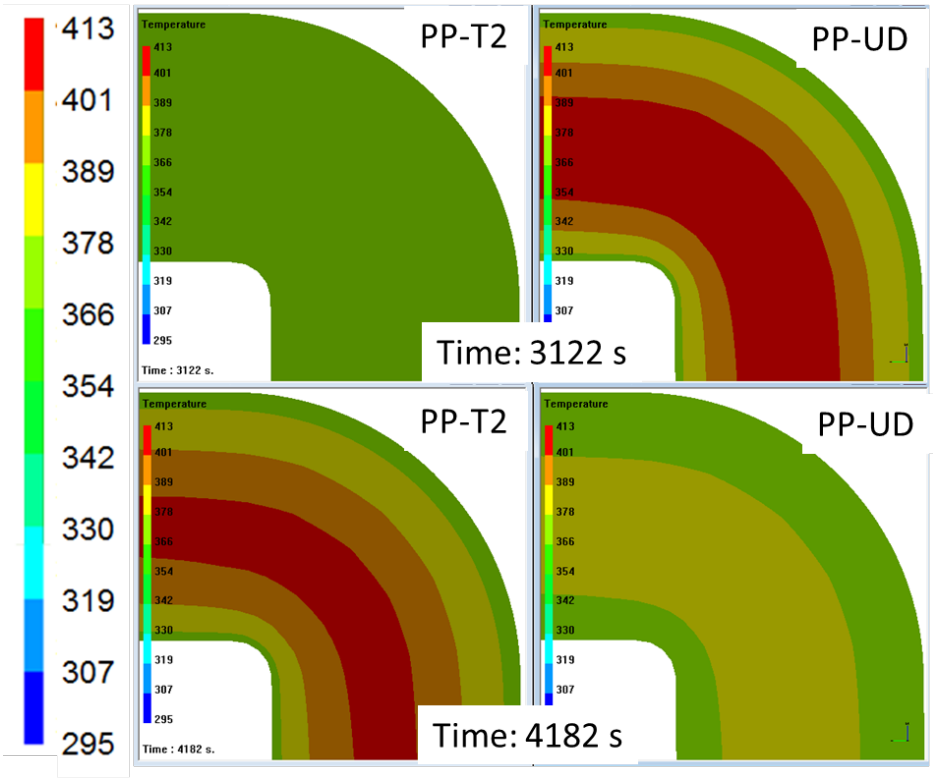

Figure 2.26: The image shows the detail of the temperature profile result vs. curing time for the PP-UD (right) and PP-T2 (left) after 3122 and 4182 seconds, points evidenced on figure 6 as 1 and 2, where the temperature peaks were found on each case.

considering that T_g's obtained in the DSC scans are definitely not representative of what is the real T_g reached in an industrial curing cycle, nevertheless the differences observed for the two commercial prepregs suggest that a good practice should imply verification of actual attainable features of materials in the applied work up conditions in order to reach the best possible performance when designing a curing cycle for such a complex part as the one investigated in the present study.

Kinetic behaviour upon curing was studied for the two raw prepregs, in order to obtain parameters for a curing simulation. In the simulation conditions differences in the curing behaviour were outlined, with the PP-UD that reacts faster and slightly more violently. Though curing condition used for simula-

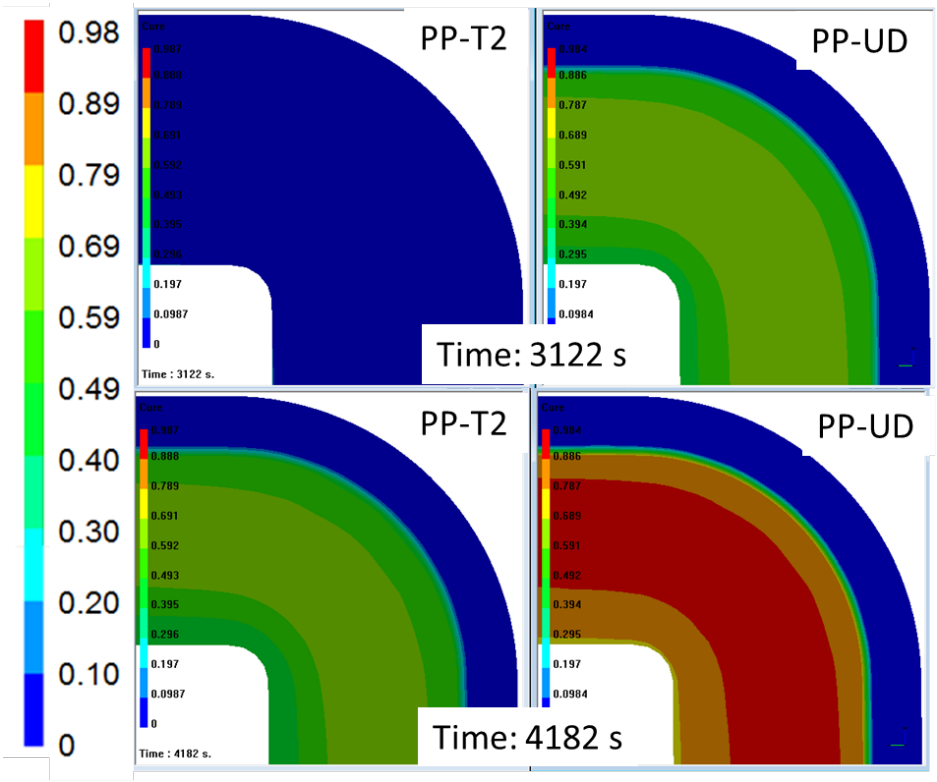

Figure 2.27: The image shows the detail of the cure degree profile result vs. curing time for the PP-UD (right) and PP-T2 (left) after 3122 and 4182 seconds, points evidenced in Figure 6 as 1 and 2, where the temperature peaks were found on each case.

tion can obviously be tuned in order to limit the observed differences, the simulation demonstrate clearly that two prepregs produced by the same supplier and composed of the same resin precursor in the same fibre/resin ratio unexpectedly behave quite differently. Once again the observed differences in the reacting behaviour impose the need of tuning curing cycle conditions in order to reduce overheating shots and, contemporary to promote equal reaction of the two components without inducing too much residual stress between adjacent layers. Indeed, this is particularly important when the final object to be cured is made up of a sequence of layers where the prepregs alternate, and not necessarily with a regular pattern. The discrepancy in the heat evolution might indeed induce stresses and overheating ending in affecting

the final mechanical properties. This work shows that the experimental verification of raw materials and curing conditions, though it may sound costly and time-consuming, might help identifying unforeseen critical situations and avoiding the lack of performance in the final composite materials.

Chapter 3

Manufacturing Technology: Liquid Composite Moulding

1 VACUUM ASSISTED RESIN INFUSION PROCESS

FE ANALYSIS AND PRODUCTION EXPERIENCE OF A SANDWICH STRUCTURE COMPONENT

1.1 Introduction

Among the several manufacturing technologies, the vacuum assisted resin infusion process (VARI) is commonly used to produce large structures [87], [88].

The marine industry started replacing the open mould hand lay-up process with VARI for several reasons: a key motivation can be identified with a healthy improvement of working conditions of manufacturing plant due to lower volatile component emissions and less hazard contact between the operator and the materials [89]. In particular, many producers use polyester based resins with Styrene content, a chemical known to be harmful to health. Another benefit of VARI process in comparison to hand lay-up is the possibility to better control the component thickness through the dosage of the quantity of resin and, consequently, to improve the final mechanical properties [90], [91], [92]. VARI process is also economically advantageous with respect to other processes such as autoclave moulding of pre-impregnated

layers (PrePreg), since no autoclave is needed and also because raw materials are less expensive than pre-impregnated ones; or to RTM process thanks to lower tooling costs. Indeed in VARI process only one side mould is needed; the dry layers of fibres are placed on top of it and the compaction is realized through an economic flexible bagging film which is closed to the rigid mould using sealant tape and sealing the whole system. Inlet and an outlet positions are defined for each particular component, a correct selection of inlet and outlet positions allows to obtain 100% impregnation, thus being a critical point for the process [163]. The outlet is connected to the vacuum line so that the cavity is initially under-pressurized while the inlet is connected to a bucket with catalyzed resin at atmospheric pressure. The pressure gradient between the two points give rise to the the resin flow. In order to assist the process several process enhancer materials can be placed over the fibres: peel ply, which promotes bag detachment and provides to the surface a rough finishing almost ready to adhesive bond on it; resin flow media, which acts as a high permeability layer and accelerates the resin flow inside the media; micro-perforated membrane, which allows air to escape while retaining the resin, thus drastically reducing air bubbles and voids.
Darcy's law (Eq. 3.1) is often used to predict the saturated permeability of the fibrous media [94], [95], [125]. This law was first proposed by Henry Darcy in 1856 while studying the flow of water through saturated porous media.

$$\vec{V} = -\frac{\mathbf{K}}{\nu}\vec{\Delta}P \tag{3.1}$$

Where $\vec{V}$ is Darcy's velocity (resin speed), $\mathbf{K}$ is the permeability tensor, ν is the resin viscosity and $\vec{\Delta}P$ is the pressure gradient, which in VARI ranges between atmospheric pressure (1 Bar) at the inlet to the vacuum level (e.g 0.1 Bar) at the outlet. Particularly in VARI process (and differently from RTM), the counter-mould is a flexible membrane, which can generate different compaction level of the preform within the mould: the compaction pressure of the fibres (P_c) is a result of the balance of the external pressure (P_{ext}) and the resin pressure (P_r) at each particular point of the component and stage of the process. For this reason the fibre volume fraction (V_f) changes during the

process and, as a consequence, also the permeability tensor varies [97], [92]. The variation of laminate thickness and fibre content are usually neglected in industrial practice process design while their influence on permeability can be properly considered by process simulation codes such as the commercial software PAM-RTM [98]. In this way FE analysis can be used to accurately predict the resin flow thus allowing the definition of optimal inlet and outlet positions in order to guaranty a complete impregnation of the component before starting the real production campaign. The dependency of permeability on fibre compaction makes the material characterization more complex and tedious, since the permeability values need to be obtained not only for the different directions, but also for different laminate compression levels (i.e. compression of the laminate determines the fibre volume fraction). Accurate permeability data are essential for reliable process simulation [99].

Moreover, when low weight components are required, it is a widespread design strategy to distance two high strength fibre reinforced layers with a low density/low strength core, thus creating a sandwich structure [100]. In this way the bending stiffness is strongly increased with a minimal increase of the weight. When the manufacturing process is the VARI, the introduction of a core between the fibre reinforced layers generates an additional technological problem because it also separates the layers in term of resin flow. Indeed the inlet and outlet are usually positioned on the top-side (within or in contact with the flexible membrane) and the core would isolate the bottom layer from the resin flow path. For this reason process-optimized core materials such as longitudinally cut or transversally perforated PVC foams are available on the market.

At today, the modelling of core materials is not integrated into PAM-RTM simulation software, this work will present an approach to model such sandwich structures together with a procedure able to provide compaction dependent permeability data with a reduced number of experimental tests. The activities presented in this work were part of an industrial case-study aimed in producing a semi-structural component for marine use. In particular, the component is a light-weight ship runway, made of carbon fibre reinforced epoxy resin with a PVC foam core. The industrial case will be used as conducting line and as practical example of application of the previously

mentioned aspects.

1.2 Component and materials

The component under study was a ship runway (Fig. 3.1), 2400 mm long and 350 mm wide. During the production, the visible side was in contact with the rigid mould, in order to give it a smooth surface quality, while the bottom of the runway was in contact with the peel ply, distribution media and bagging film. The central part of the runway had sandwich construction with a 20 mm thick PVC foam core of 60 kg/m^3, with transversal holes of 1 mm diameter distanced 20 mm from each other. Two kind of reinforcement materials were used: a carbon fibre 2x2 twill of 200 g/m^2 and carbon fibre non crimp biaxial fabric of 600 g/m^2. Regarding the resin, it was an epoxy for infusion resin EC157 with W61 hardener, both provided by ELANTAS srl, the viscosity at room temperature was 250 mPas and the pot-life of 90 min.

A central injection setup was used: the inlet was positioned on the centre of the runway with a line runner covering the whole runaway length, while the outlet was positioned all along the periphery of the mould. This setup made the resin flow mainly unidirectional, going from the line runner to the sides. For this reason and in relation to the used balanced fabrics, the characterization of the laminates for the simulation was done in just one direction, by considering that the permeability in the two principal directions was equal ($K_1 = K_2$). The permeability isotropy assumption was a simplification used for this particular case, the reader has to be very careful about this: a balanced fabric can have a different permeability in each principal direction because of the influence of the stitching or different tension in warp and weft fibres during weaving process.

Moreover each combination of reinforcements may have a different permeability which needs to be specifically characterized [101];in the runaway five different stratifications were realized depending on component shape (see table 3.1 and figure 3.2):

- Laminate A0, in the centre of the runaway bag side, with one layer of

biaxial fabric, peel ply and the distribution media;

- Laminate A1, in the centre of the runaway mould side, with one layer of twill and one layer of biaxial, the core is placed in between A0 and A1;
- Laminate B, at the end of the core where A1 and A0 were overlapped thus providing two layers of biaxial, one layer of twill, peel ply and the distribution media;
- Laminate C, similar to zone B but with no distribution media, hence two layers of biaxial, one layer of twill and peel ply;
- Laminate D, where the two adjacent laminates were overlapped giving as a result a doubled C laminate, thus two layers of biaxial, one layer of twill, again two layers of biaxial and one layer of twill and finally the peel ply.

Figure 3.1: Image of the runway, on the left the top side and on the right the bottom side

1.3 Permeability characterization procedure

An adequate characterization of the materials permeability is of paramount importance in order to be able to perform a FE analysis of the process which correctly accomplishes the prediction of the resin flow through the cavity, the required quantity of resin and the filling time. Permeability characterization is a topic quite discussed in literature, where several characterization methodologies have been proposed [102] [103] [104] [105]. In most cases the transversal permeability (K_3) is not used since the components to be produced are usually thin enough to allow neglecting this dimension. This is even

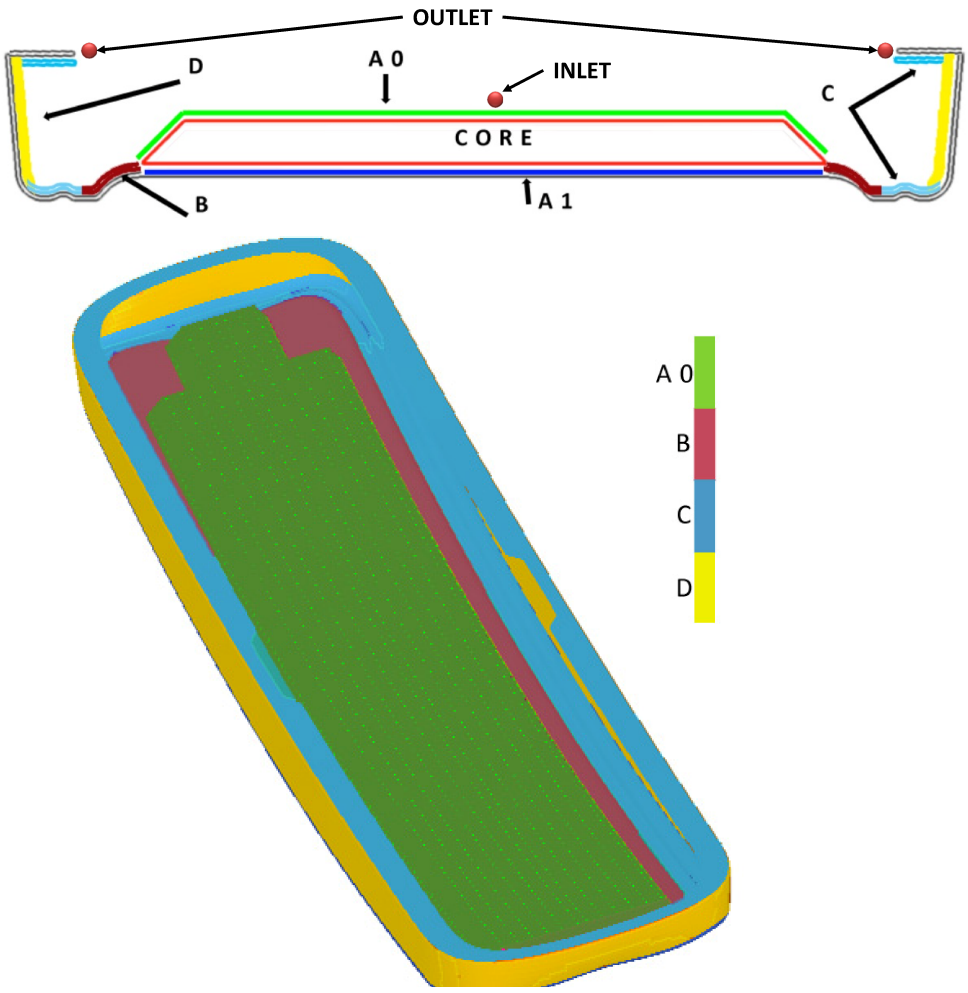

Figure 3.2: Representation of different lamination zones on the runway, cut view on top and view from the bottom below

more evident when the VARI module of PAM-RTM code is used because the meshing of the geometry is realized through surface elements and transversal permeability is neglected by the code.
The most simple characterization technique is to perform unidirectional flow measurements in each principal direction. The usual configuration consists on a rectangular mould, with the injection placed on one side and the vacuum applied on the opposite one; measurements of the flow front position throughout time are cried out in order to retrieve the permeability values [126].

Table 3.1: Summary of Zones

Zone	A (^{0}: A0; ^{1}: A1)	B	C	D
Process materials	Distrib. media^0 Peel ply^0	Distrib. media Peel ply	 Peel ply	 Peel ply
Reinforcements	Biaxial^0 CORE Biaxial^1 Twill^1	Biaxial Biaxial Twill	Biaxial Biaxial Twill	Biaxial Biaxial Twill Biaxial Biaxial Twill

Another technique utilizes an injection point in the centre of a mould so as to analyse a radial flow front [128], [129]. This technique has the advantage to avoid the so called *edge effects*, referring to high permeability zones usually found on the sides of the mould on unidirectional measurements. Indeed on the mould edges, where the fibre preform ends, the resin has the tendency to flow faster thus distorting the calculated permeability values. The radial flow permeability characterization is also attractive because the full in-plane permeability tensor can be measured in a single experiment, but it adds difficulties in the data acquisition phase, because an ellipse has to be measured throughout time, and also in the data analysis stage because it was seen that the diameter of the injection gate influences the permeability result [109], [110].

Different methods to obtain the flow front position had also been proposed in literature: manual point registration during the tests [126], video recording camera [135], in-situ sensors such as thermistors [131] and optical fibre sensors [99] are some of them.

In this study, the two principal permeabilities (K_1 and K_2) were considered equal, so only the unidirectional permeability measurement was performed for each laminate although the characterizations were repeated for the different stratification types (zones A,B,C and D).

In order to measure the permeability as a function of fibre volume fraction (K-V_f), the usual approach is to perform many individual characterizations

at different fibre volume fractions and then use the data to interpolate a curve, however this makes the characterization stage burdensome, time consuming and expensive. A method to simplify this process will be presented here, the methodology is applicable to any laminate. The method consists on three steps which will be explained in next sections.

Permeability characterization at Constant fibre volume fraction

The methodology starts with a constant volume fraction permeability measurement with the scope of obtaining one point of the $K - V_f$ curve. From the unidirectional expression of Darcy's law (Eq. 3.1) and the mass continuity equation ($divV = 0$), it is possible to obtain the following relation by integration in time and length:

$$L(t) = \sqrt{\frac{2K\Delta P}{\Phi\nu}t} \tag{3.2}$$

In equation 3.2, L is the length of the flow front at a given time t, Φ is the porosity of reinforcement (equal to $1 - V_f$, where V_f is the fibre volume fraction) and K and ν are the already described permeability and viscosity. Equation 3.2 can be easily applied to obtain the permeability at a given porosity (i.e. volume fraction) value, consequently requiring a rigid cavities test configuration (i.e. comparable to a RTM process) because it allows the constancy of the volume fraction during the experiment.

Each laminate was tested at a given fibre volume fraction value, by using a rectangular mould made with two 8mm thick polycarbonate plates distanced with a metal ring (Figure 3.3). The effective mould length was 320 mm and the width 100 mm, rather small in order to minimize the deformation of the plates by vacuum effect, although long enough to measure the flow front and make the characterization. The deformation of the plates can alter the the estimated measurement [126]; in order to keep this value low during the present investigation, the vacuum level used was never superior to 0.5 Bar. The deformation of the plates was monitored by means of a digital indicator and observed less than 0.05 mm of deformation in the length where the flow

front position was recorded (central 200 mm).
The laminate was positioned between the plates and sealant tape was used to seal the mould and avoid any edge-effect phenomenon. The injection point was placed on one side and the outlet on the opposite side of the mould. A video camera was used to record the trials and retrieve the flow position as seen from the top throughout time (Figure 3.4). Trials were repeated for the four different stratification types. The fibre volume fraction could be easily calculated when the total volume of the cavity, the fibre weight and its density are known. The permeability K was obtained by applying equation 3.2 at different points of the process and then averaging the results. The values obtained are presented in table 3.2.

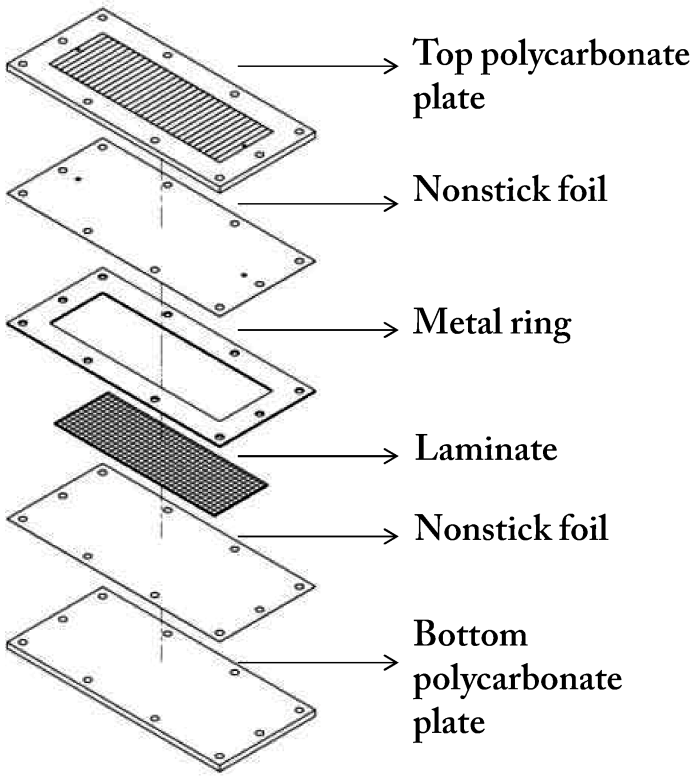

Figure 3.3: Design of test mould used to perform constant volume fraction permeability characterization

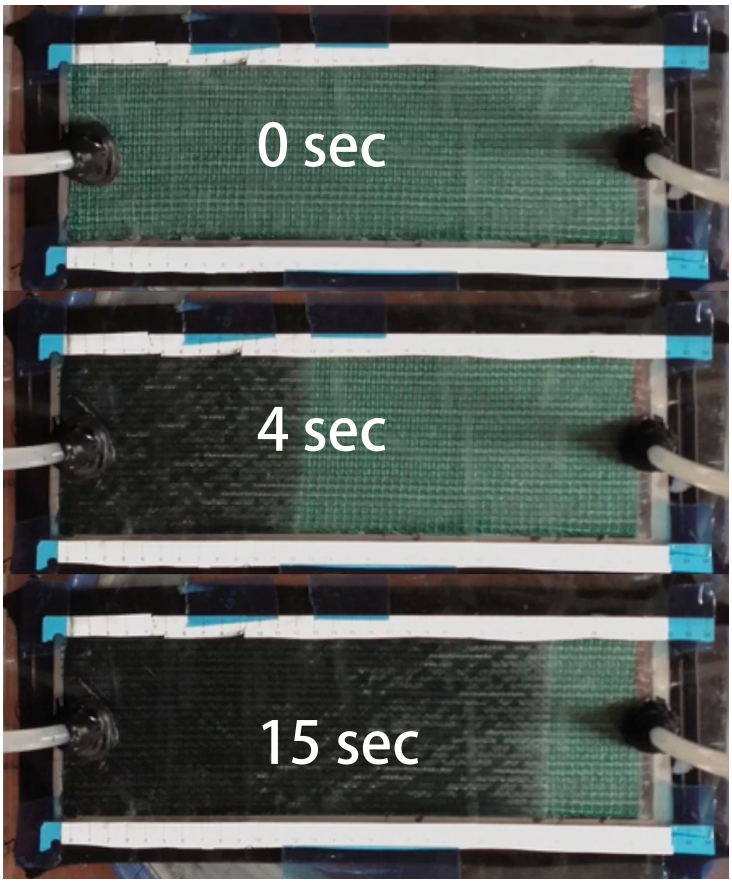

Figure 3.4: Flow front advancing through test mould

Table 3.2: Results for constant Φ permeability characterizations

Zone	K	V_f	Φ
A0	$3.021x10^{-9}$	0.44	0.56
A1	$1.817x10^{-10}$	0.51	0.49
B	$4.867x10^{-10}$	0.54	0.46
C	$2.102x10^{-11}$	0.53	0.57
D	$7.804x10^{-12}$	0.57	0.43

Compressibility curve

The compressibility curve describes how the fibre volume fraction (V_f) changes with a change of the pressure. PAM-RTM code requires this information as input for each laminate in order to perform VARI simulation. A very sim-

ple and straightforward method was used to determine this dependency: the laminates were placed between two rigid plates and sealed inside a vacuum bag. A similar methods to obtain the compressibility curves were already presented previously by other authors [113], [114], [88]. In this way it was possible to change the pressure over the laminate by modifying the vacuum level, assuring a uniform distribution of the pressure over the laminates. The thickness change was measured with a Mitutoyo digital Indicator with an accuracy of 0.01 mm, as reported in figure 3.5. The function of the rigid plates was to provide a flat, smooth and uniform surface where the instrument could be positioned, unlike the rough surface of distribution media and reinforcements. Measures were done starting from 0.1 Bar (maximum vacuum grade), and releasing in steps of 0.1 Bar up to 1 Bar (no vacuum, natural thickness of the laminate) as reported in figure 3.6.
From the thickness data obtained it was easy to calculate the fibre volume fraction by using the following equation:

$$V_f = \frac{\rho_{sup}/\rho_f}{thickness} \tag{3.3}$$

Where ρ_{sup} is the surface density of the laminate expressed in g/m^2 and ρ_f is the density of the fibres in g/m^3.

Thus, the data were used to regress a power law curve in the form: $P = A * V_f^B$, which was found to properly match the experimental results [115]. The regressed equations are reported in figure 3.6, these equations were assigned to each zone in the simulation as input.
This type of measurement assumes that the lower friction provided by the resin does not modify substantially the measurement of the compressibility curve, though it was reported that this could happen and that the nesting effect could be increased thanks to the lower friction provided by the resin [116]. The measurements were done starting at full compression and releasing the pressure in steps of 0.1 bar: it was seen that the dry release curve is similar to the wet release, while very different to the dry compression curve [117], for this reason only the release curve was considered for the computation of the power law [118].

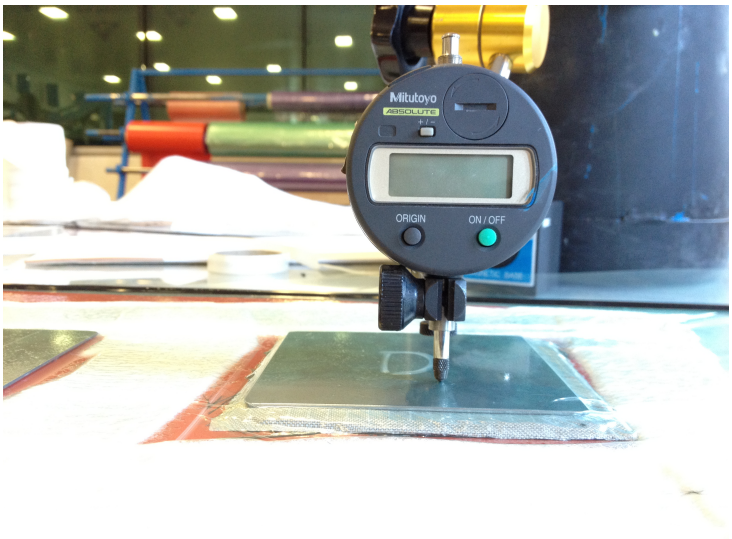

Figure 3.5: Measuring the compressibility curve

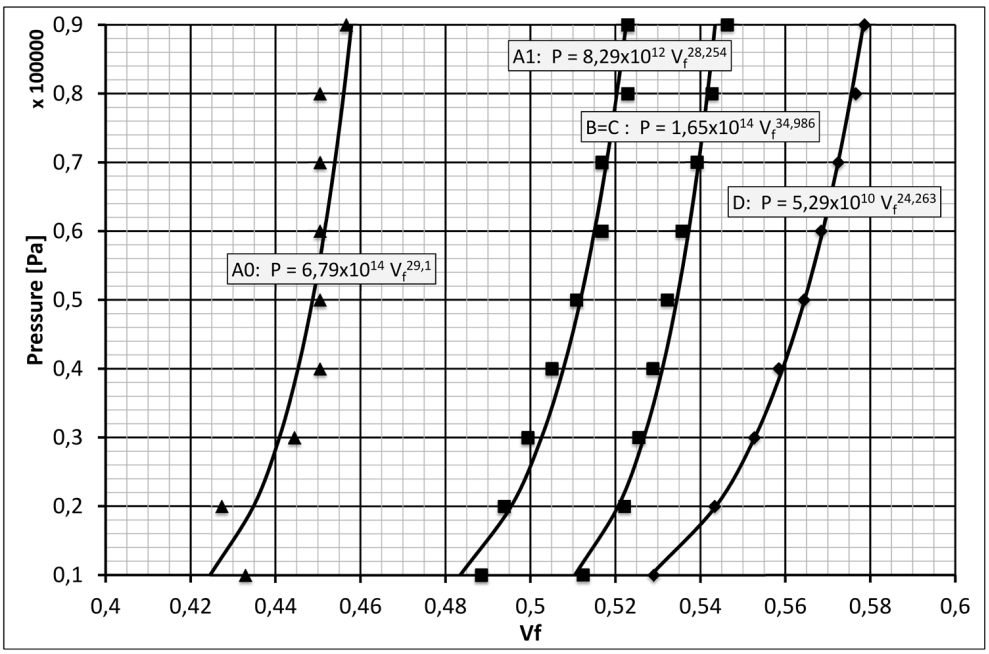

Figure 3.6: Fibre volume fraction and compressibility curves for the different laminates

Infusion experiments and correlation for the computing of $K - V_f$ curve

In line with many researchers, an empirical power law function of the fibre volume fraction of the form:

$$K(V_f) = GV_f^N \tag{3.4}$$

was adopted to express the $K - V_f$ curve ([118], [113], [135]), where G and N are characteristic values of each particular laminate. The value of K obtained with the constant V_f permeability characterization was assumed to be a point belonging to the curve, this simplification allowed to express a relation between G and N (e.g. $G = \frac{K}{V_f^N}$).

Thus, it was possible to estimate the parameters G and N by correlating a simple VARI experiment with the same process simulated by means of PAM-RTM. The VARI experiment configuration used was an unidirectional permeability characterization, with the laminate positioned over a flat mould and closed with the bagging film. During the VARI process, the resin passes through the whole range of permeabilities that the preform presents from a volume fraction at atmospheric pressure to a volume fraction at vacuum level of pressure (Fig. 3.7).

In an iterative procedure, the simulation was run several times varying the value of N until an acceptable correlation was obtained between the flow advancement in the real experience and in the simulation. Figure 3.8 shows three iterative steps used for zone D, on the right side it is possible to see how the permeability curve changed using values of $N = -10$, $N = -30$, $N = -40$, notice that the three curves pass through the point obtained with the constant V_f permeability characterization, the left side of the picture shows the numerical results of the flow position in the three iterations, compared to the values obtained from the experiment.

This should not be treated as the most accurate method to obtain the $K-V_f$ curve, the possible errors of the constant V_f permeability measurement are directly dragged-in to the final result. A regression approach to fit a curve after many constant V_f permeability measurements is probably a more correct approach. However, the presented proceeding is a very efficient since only two injection trials are needed, one at any constant V_f value and one with the VARI configuration.

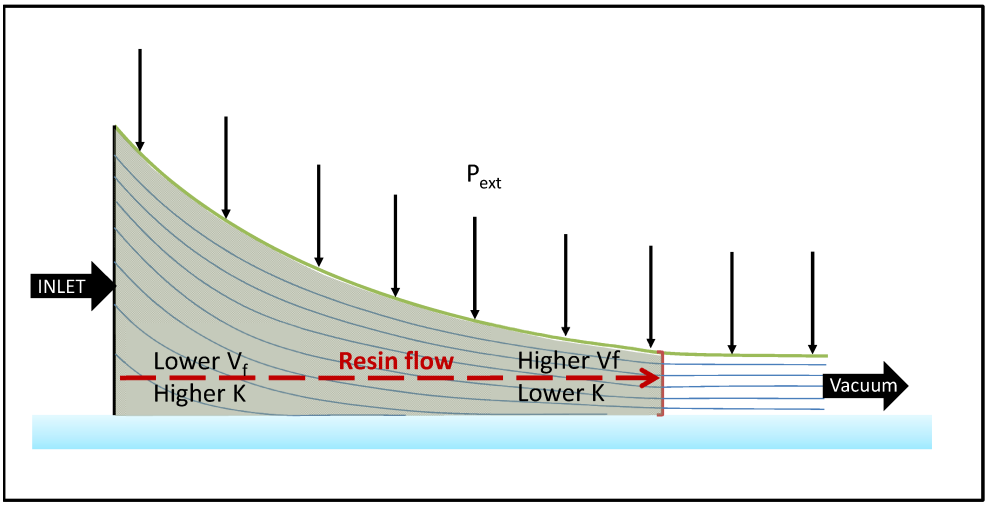

Figure 3.7: Illustration representing the fibre volume change across preform saturated with resin

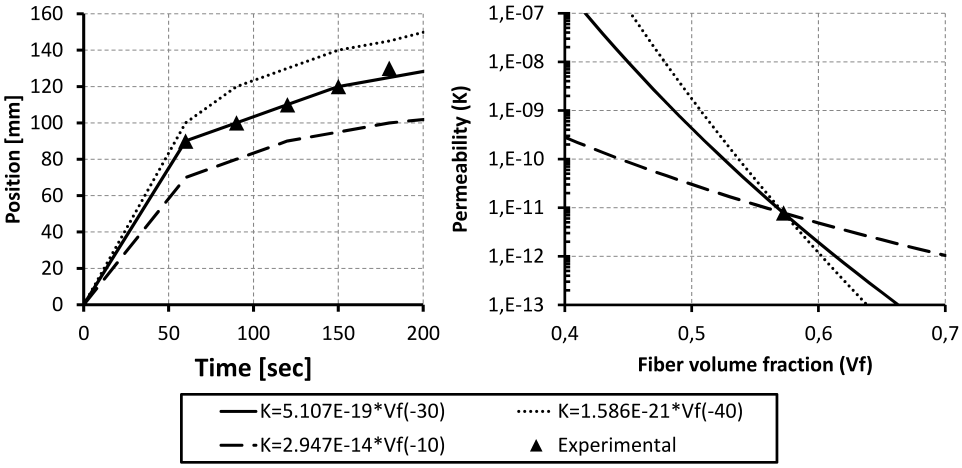

Figure 3.8: Three iterations for laminate D. Right: curves of permeability. Left: numerical vs. empirical results

The case of a sandwich structure

As already mentioned, zones A0 and A1 of the runway were the upper and lower laminates of a sandwich structured section, distanced by a 20 mm thick PVC foam core. This type of construction allows to increase the bending stiffness of the component with low weight increase. The foam core was enhanced

for the manufacturing process with transversal holes of 1 mm diameter in a 20×20 mm grid. The perforations allow the resin to flow to the laminate in the tool-side (A1) during the infusion with line inlet over the bagging film-side laminate (A0).

This configuration needs to be characterized for permeability in order to simulate the resin flow through it. Since the VARI module of PAM-RTM software runs only with triangular surface elements, it was not possible to consider the use of 3D elements. Nevertheless, surface elements can be combined in a 3D space to get a so-called 2.5D model: this approach was used to model the top and bottom layers as surfaces representing the laminates connected by surfaces in the transversal direction representing the perforations of the core (figure 3.9). A similar solution can be found in reference [119], although in their case the core had grooves instead of holes to enhance the process. Mould filling with the grooved core was also studied in [120], although it was not found any study regarding the flow through the perforated core.

The permeability of zones A0 and A1 were characterized individually as the rest of the laminates, and then a specimen with the sandwich construction was used to define a *thickness* value for the holes (permeability was not considered by the code since porosity was set to 1), and to perform a first correlation between experimental and numerical results before performing a full-scale simulation of the filling process of the runway.

The mesh representing the specimen is reported in figure 3.9:the three zones of the model representing the laminates and perforations can be seen in the bottom detail of the figure, composed by the yellow, green and blue elements. Each perforation was composed by 16 triangular elements and connected by two nodes to each laminate in order to allow the resin to flow through them, a porosity of 1 and thickness of 1.6 mm was assigned to the zone containing the elements of the perforations. Figure 3.10 shows the flow of resin through the 2.5D model of the sandwich. Figure 3.11 shows the simulation compared to the real experience as seen from the top and bottom of the specimen at a specific stage of the process (29 sec).

This approach completes the materials permeability characterization process: a summary of the K-V_f power laws is reported table 3.3. The next section will present the results of the full-scale runway simulation.

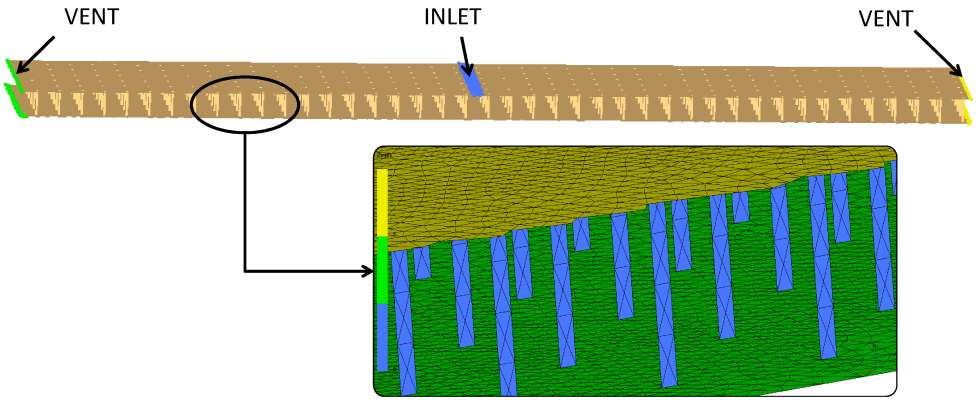

Figure 3.9: Mesh of the specimen used to simulate the sandwich structure with perforated core. The image on the top shows the full specimen, with the positions of the inlet and vents, on the bottom image the detail of the mesh is shown, with the elements representing the laminates connected by the elements representing the holes

Table 3.3: $K - V_f$ curves obtained for each laminate

Zone	$K(V_f)$
A0	$5.059x10^{-15} * V_f^{-16}$
A1	$6.412x10^{-12} * V_f^{-4.8}$
B	$2.604x10^{-10} * V_f^{-1}$
C	$3.676x10^{-14} * V_f^{-10}$
D	$5.107x10^{-19} * V_f^{-30}$

1.4 Full scale simulation and experience results

Once the permeability curve was obtained for each laminate, it was possible to proceed with the simulation of the injection process of the full component. The aim of the procedure explained before was to obtain these characteristic values and to perform the simulation, which served to verify the injection strategy of the component, assuring a complete impregnation of the component within the pot life time of the resin before its production, and in this

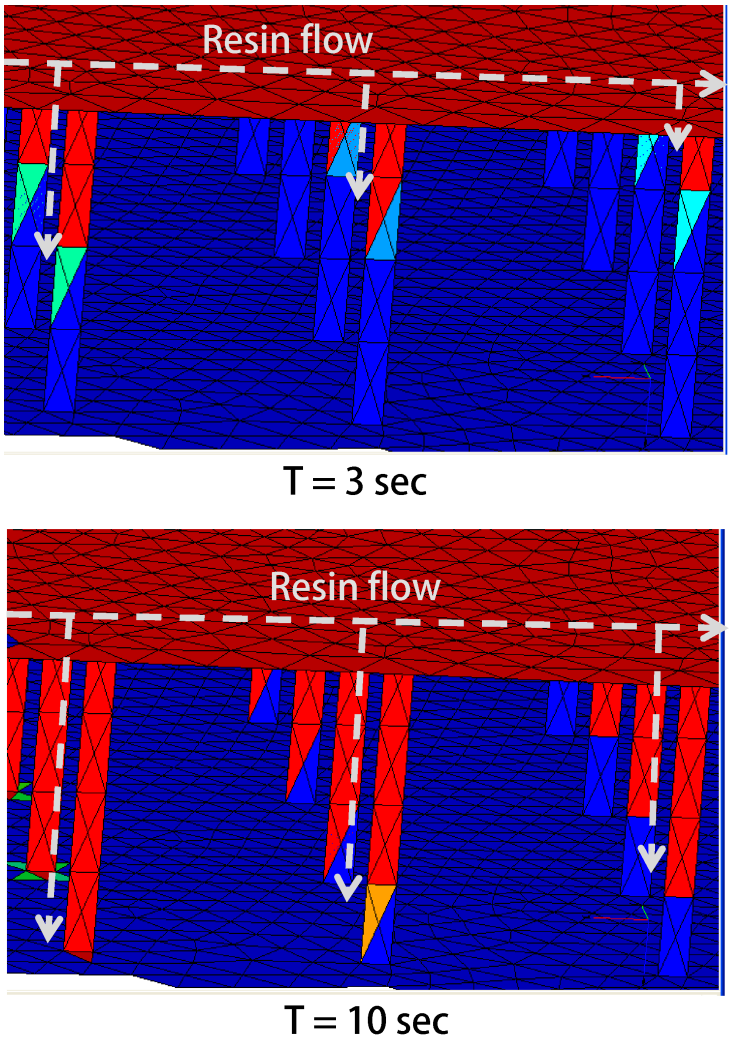

Figure 3.10: Simulation results at 3 and 10 seconds with the 2.5D representing the sandwich specimen

way guaranty a good result of the manufacturing process.
A CAD model of half runway was used, taking advantage of the symmetry of the component. The model was meshed using triangular elements; the perforations in the core were represented as explained before, using triangular elements, with two nodes in common with the layers over and under the core. The elements were divided into zones, as shown in figure 3.12, each representing a specific laminate. The Pressure-Fibre content compressibility curves reported in figure 3.6 and the permeability curves as a function of fibre con-

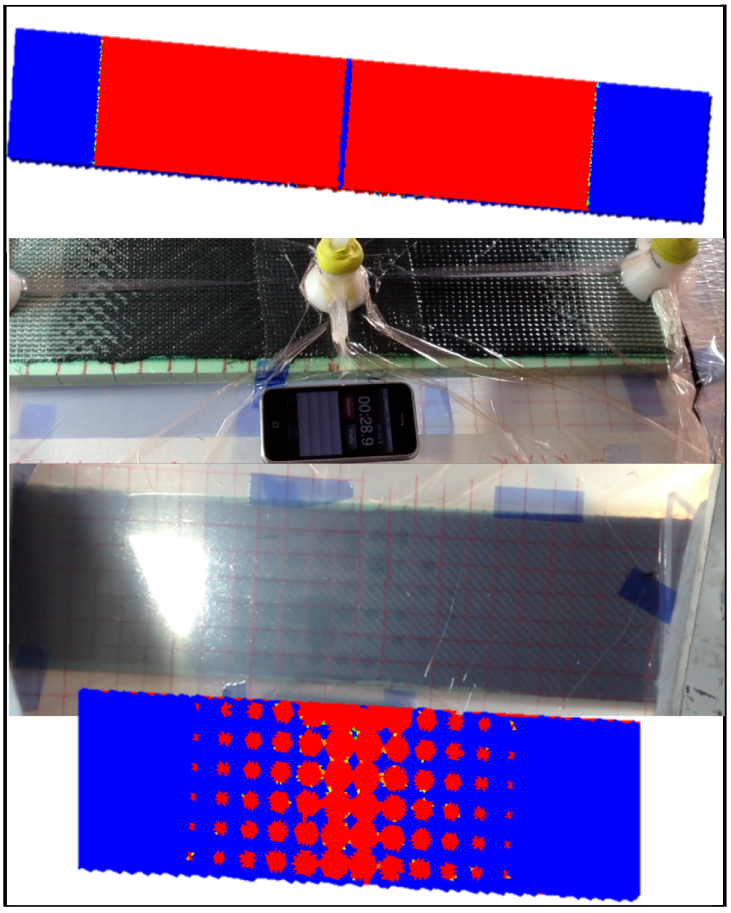

Figure 3.11: Experimental and simulated results for the sandwich specimen as seen from the top and bottom at 29 seconds

tent reported in table 3.3 were assigned to the zones. The injection strategy was, as explained before, to position an inlet with a line runner on the top layer of the symmetry plane and a line vent on the external periphery of the runway.

After running the simulation it was possible to verify that the injection process would take about 20 minutes, amply inside the pot life limits of the resin, and it would assure a complete impregnation of the component. The first component was produced and the flow dynamics were found to be in good agreement with the prediction of the simulation, proving the success of the characterization procedure. A series of pictures comparing experience and simulation at different points of the process can be found in figure 3.13.

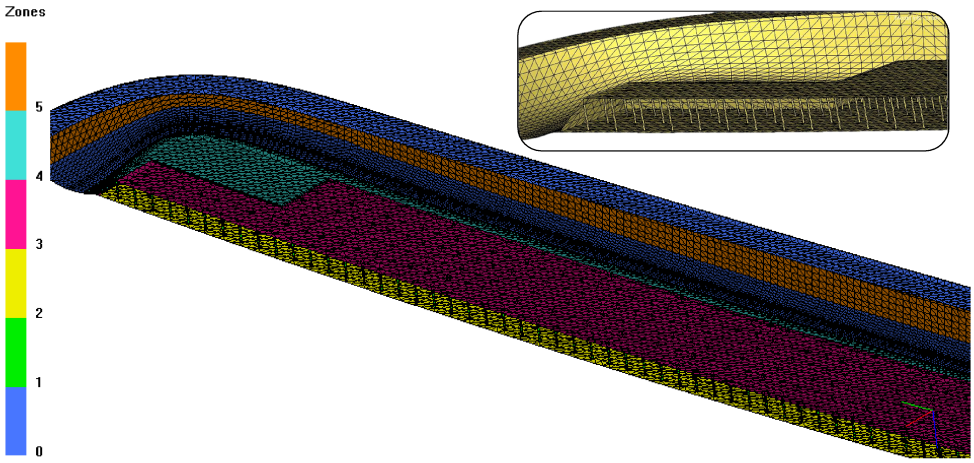

Figure 3.12: Model of the runway divided in zones with the different laminations, the detail on the top-right corner shows the sandwich section of the mesh

1.5 Conclusions

The section deals with a problematic very common in industry when manufacturing processes are based on vacuum assisted resin infusion. Trial and error is still today the most used approach for the definition of injection strategies but the interest towards the application of FE analysis for processing optimization is of growing attention. In order to perform a valid simulation there is a need to characterise the laminates and to obtain reliable permeability data. A procedure able to obtain characteristic values with few experimental procedures was presented and applied with success to the production of a ship runway. The procedure starts with a classic characterization at constant V_f and then the acquisition of data to construct a $Pressure - V_f$ curve. These data are then used together with an infusion test to correlate the last with a simulation and finally obtain the $K - V_f$ curve for each laminate.

The assumptions made with the method are: *a*) the $K - V_f$ curve is continuous and can be described with a power law function; *b*) the value of K obtained with an RTM approach (constant V_f) belongs to the $K - V_f$ curve;

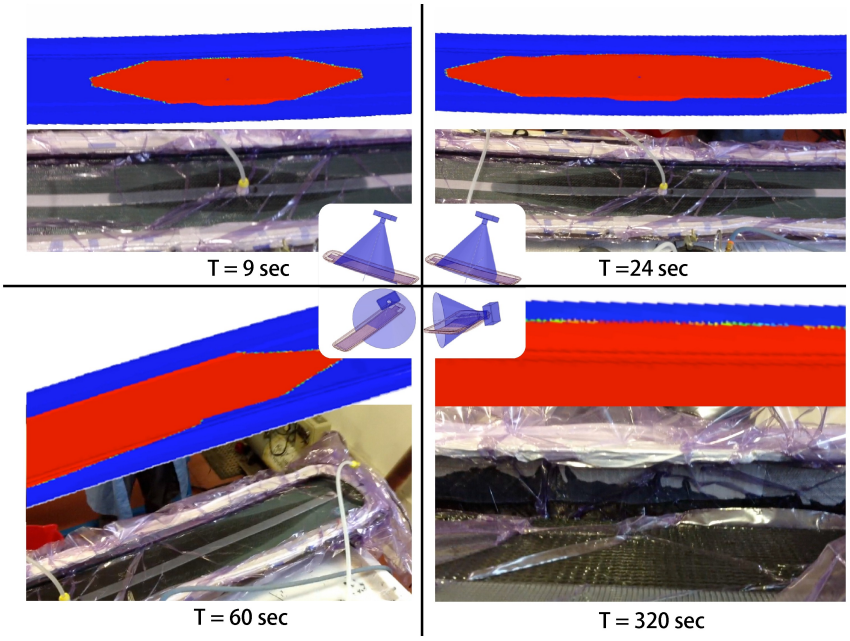

Figure 3.13: Experimental and simulated results of the runway injection after 9, 24, 60 and 320 seconds

c) dry release compressibility curve is able to provide the fibre volume fraction as a function of pressure, modelled with a power law function.
The industrial case study, a lightweight ship runaway, provided as a conducting line during the study had a zone made with a sandwich structure (with perforated core), this kind of structures are not directly implemented in PAM-RTM, one of the most divulged commercial software, the section provides a way of dealing with sandwich structures where perforated cores are used.

2 RESIN TRANSFER MOULDING PROCESS

FABRICATION AND PROCESS SIMULATION OF A CFRP CON-ROD BEAM

2.1 Introduction

Resin Transfer Moulding (RTM) is a process that has lately received much attention in industry [121] because of the many advantages it shows over the widely spread hand lay-up of pre-impregnated plies (prepreg) and autoclave curing technology. In RTM manufacturing, a closed rigid mould is needed, inside it layers of dry fibres are positioned before closure and resin is then injected to wet the fibres in order to obtain the composite material part. The curing process can be achieved by heating the mould on a predefined cycle before the part gets extracted. When compared to prepreg hand layup and autoclave curing process, the advantages of RTM are: direct economical savings because dry fabrics and raw resin are cheaper than prepreg, since an echelon in the supply chain is skipped. Logistic savings, because raw materials don't need to be stocked inside a fridge, unlike prepregs. Productivity advantages since process times can be reduced, not only because there is no need of hand lay-up, but also because more reactive resins can be used. In general Prepreg+Autoclave is considered a low scale technology ($10^1 - 10^2$ parts/year) while RTM can cover the medium scale production ($10^2 - 10^5$ parts/year) [122]. Also improvements in terms of mechanical properties can be achieved since with RTM it is possible to work with 3D woven preforms which can include fibres oriented in any direction [123]. When using prepreg layup it is not possible to position fibres oriented in the perpendicular direction with respect to the stacking sequence.

The drawback of RTM and other Liquid Composite Moulding (LCM) technologies e.g. Vacuum infusion, is that a new production variable needs to be considered: the optimization of the resin flow to properly wet all the fibres and avoid dry spots [124]. For this purpose commercial packages were developed, such as PAM-RTM [125] or RTM-Worx, where numerical models were coded to predict the resin flow.

PAM-RTM Software was used during the study that leads to the present section. This software, developed by ESI-Group, includes many packages covering almost all LCM technologies. The RTM module can work with a full 3D model and calculates the resin flow using the viscosity properties of the resin, the permeability of the plies and the boundary conditions imposed, which can include Pressure or Flow-rate inlets, Vents and eventually temperature inhomogeneity (for this last variable a different module called Heated-RTM is available). The calculations of the flow are based on Darcy's Law and the continuity equation.
This study includes also the experimental results on the injection process, the curing process simulations using PAM-RTM curing module, DSC analysis of the final component and mechanical tests, in tension for the full component and on interlaminar shear strength for specimens produced by the RTM process as well as specimens produced using the prepreg and autoclave process, including a subsection analysing the impact on interlaminar strength of a product used during the RTM process.

2.2 Part and Mould design

The part under study was a Carbon-fibre-reinforced-epoxy con-rod beam, to be used in a crane arm assembly. Composite materials are characterized by high strength to weight ratio, and in this case using a light component was important in order to increase the stability of the crane vehicle, and thus to reduce the possibility of rotational overturning.
The design indicated that the con-rod thickness was 20 mm, this involved a big mass of resin to cure. If manufacturing in autoclave, it was the case were normal curing cycle needs a revision, since the heat generated by the exothermy of the reaction becomes so important that would raise the temperatures too high, potentially degrading the mechanical properties of the finished component. The beam design can be seen in Figure 3.14, as it can be noticed the component had a double-symmetry.
The mould projected and constructed had three main parts: top, central and bottom; and two inserts, positioned at bearing housing bores. A sketch is shown in figure 3.15. This design allowed an easy extraction of the pro-

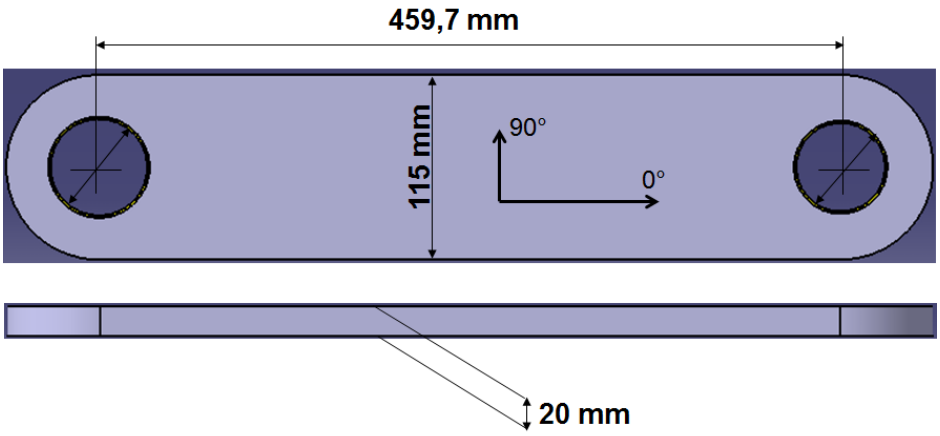

Figure 3.14: Con-rod beam dimensions

duced component, and in case the design had to be changed it could be easily achieved by modifying only the central part of the mould. The sealing was done using gaskets. Two cartridge heaters were added to the top and bottom parts, these were used to heat the mould during injection and to cure the part before the extraction.

2.3 Materials

The laminate consisted in 40 PAN based carbon fibre layers, including the following types:

- 200 g/m^2 twill fabric ($Twill\ 0-90°$)
- 600 g/m^2 non-crimp biaxial fabric ($NCF\ \pm 45°$)
- 500 g/m^2 unidirectional ($UD\ 0°$)

Positioned in a symmetric layup, with the percentage of fibres in each direction indicated in figure 3.16:

A characterization of the in-plane permeability was performed for each of the three materials in each principal direction, by using a rigid mould and unidirectional test configuration [126]. The fibre volume fraction used during the characterization was 65%, which was approximately equal to the one on the component. Results for K_1 and K_2 are reported in Table 3.4, were K_1 is the first principal permeability (0°, or along the fibres in UD) and K_2 is

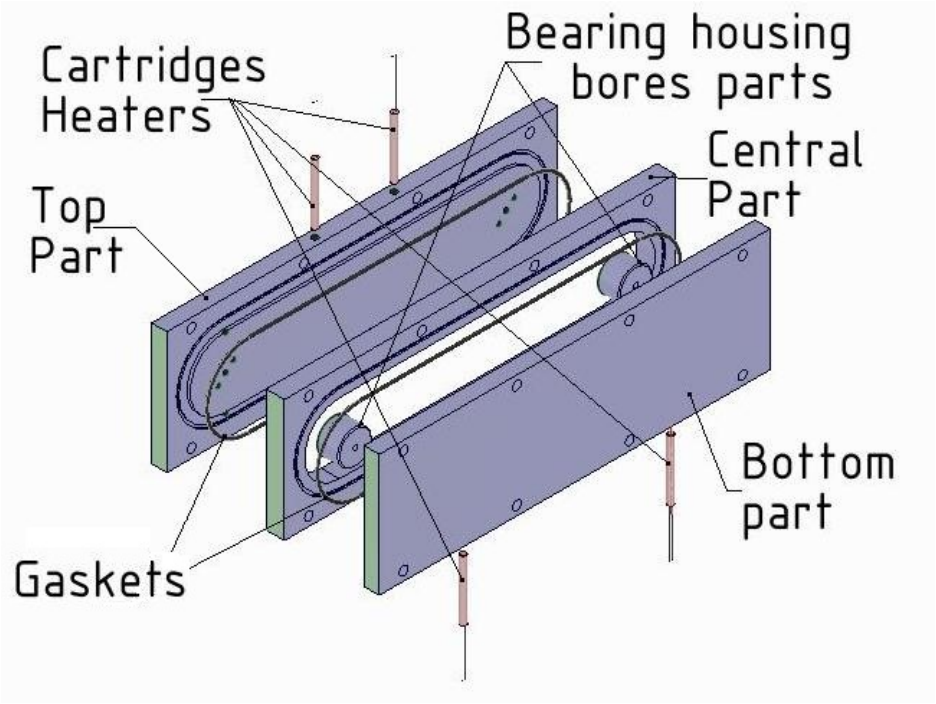

Figure 3.15: Mould design

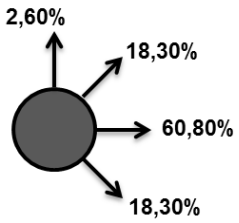

Figure 3.16: Lamination

the permeability in the orthogonal direction. This values were then used to perform preliminary filling simulations.

The resin used was the EC14 with hardener W61, both provided by ELANTAS; the specified mass ratio was 100:16. The viscosity profile as a function of time and temperature of the mixture was provided by the manufacturer (figure 3.17), a model based on it was used later for the simulations.

Table 3.4: Principal in-plane permeabilities (K_1 and K_2) for the different materials used

Material	K_1	K_2
Twill	2×10^{-11}	2×10^{-11}
NFC	1.2×10^{-10}	1.2×10^{-10}
UD	1.7×10^{-9}	1×10^{-11}

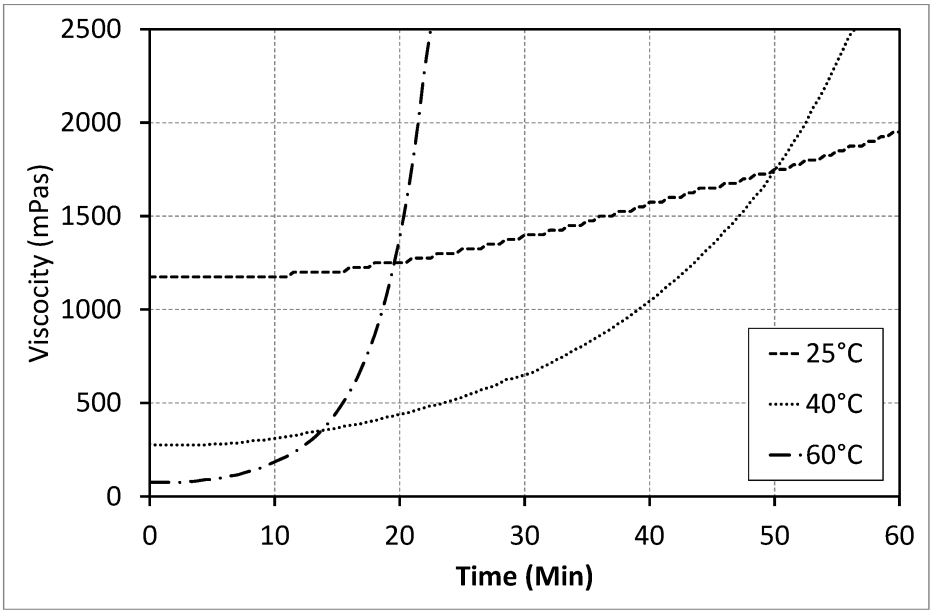

Figure 3.17: EC14-W61 Resin viscosity as a function of time and temperature

2.4 Preliminary Filling Simulation

Simulations of the mould filling process were performed by means of RTM module on PAM-RTM software. A simple planar mesh with the shape of the beam was first constructed and imported into PAM-RTM, where a laminate with the actual stacking sequence of the con-rod was defined and used as input to extrude the planar mesh into 3D elements. The resulting model was composed of 254800 elements and 136708 nodes; figure 3.18 shows a sector of it, close to one of the bearing bores.

Preliminary simulations were performed with one *flow-rate* inlet boundary condition, set to issue resin at a rate of $5.035 \times 10^{-6} m^3/sec$, the same rate used later during the production experiences, which allowed the completion

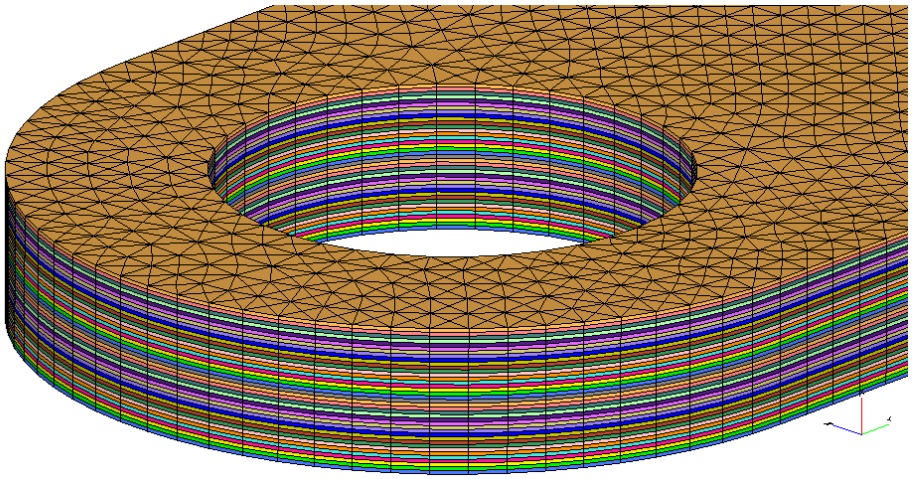

Figure 3.18: Mesh divided in zones to assign the corresponding material and properties

of the injection process in 2 minutes. The inlet was positioned in the midpoint of the mould's bottom part, in order to take advantage of the double symmetry of the part for the infusion. The scope of the simulation was to analyse which were the potential *last filling sectors* according to different values for the average transversal permeability of the laminate (K_3). Tests were performed within a range between $1 \times 10^{-11} m^3/sec$ and $1 \times 10^{-13} m^3/sec$ of K_3, these limits were obtained from literature. The simulations were set to consider also gravity during the analysis.

Although measuring the in-plane permeability values for the individual materials was a simplification, since it is known that in a laminate the plies of fibres *nest* between each other creating a new permeability configuration [127], these preliminary simulations were useful to analyse the possible flow dynamics, and to define the inlet and vent configuration of the mould. The study of the flow is a critical step in the process, a good understanding of it allows to correctly configure the process in order to obtain full impregnation. On the other hand, academic research has focused on the in-plane permeability characterization developing different methods for this (see [128], [129], [126], [130]), while on the case of a 20 mm thick component the flow is 3-Dimensional and the characterization becomes much complicated. Researchers have proposed different methods to deal with 3D characterization,

these not being anyhow simple (see [131], [132]). In this context it was decided to keep a basic mould configuration, and to continue with the work assuming the uncertainty of exact permeability values.

Figure 3.19 shows the resin progression obtained for the three different cases, according to the value of transversal permeability (K_3). Notice that for $K_3 = 1 \times 10^{-11}$ and $K_3 = 1 \times 10^{-12}$, the last filling location were the sectors behind the bearing bores. These were critical zones, also because the flow fronts were joining after getting divided by the mould inserts, potentially causing air entrapment in between the joining flow fronts. In case the transversal permeability was lower ($K_3 = 1 \times 10^{-13}$), the top-midpoints of the con-rod presented a new *last filling location*. Some sensibility tests were also performed, varying the in plane tensor 50% up and down with respect to the experimentally obtained values. In other sensibility test the original permeability zones were modified to introduce edge effects. Considering that the fibres in the first and last layers, being in contact with the mould, were in a different condition with respect to the internal ones which could *nest* between each other, an increased porosity of 80% was assigned to these elements in the computer model, and also to the elements in contact with the sides of the mould and the bearing bore inserts. It was seen that none of these tests presented a *last filling location* different to the ones seen in figure 3.19.

The information obtained from the simulations was used to define the possible vent locations. In a first stage a higher transversal permeability value was hypothesised, and only two vents were implemented. Although the safe configuration was the one with all three outlets, being this a test experience it was of interest to test first the two-vent configuration. The next section will report the results observed during the production experiences.

2.5 Production experience

An MVP PAR-50 metering mixing and dispensing machine with high precision volumetric pumps was used for the injection. During the process, the resin reservoir and the dispensing tube were kept at $60°C$ in order to maintain the resin at a low viscosity level. The mould was also maintained at

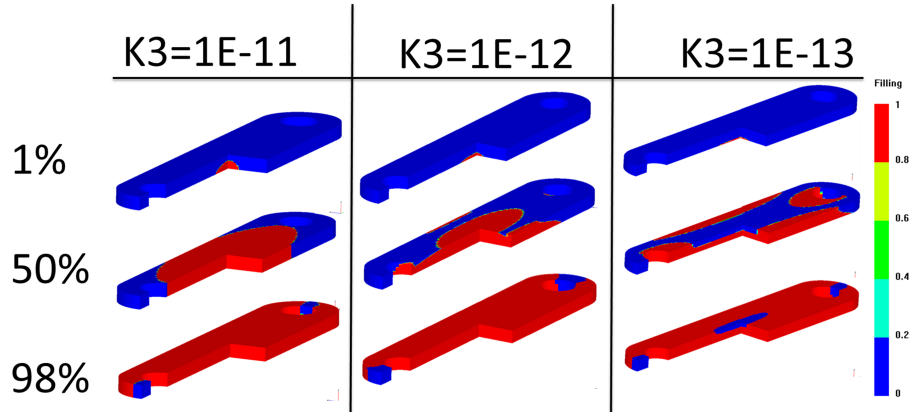

Figure 3.19: Filling profile using values reported in table 3.4 and three different values for K_3. Blue zones are dry, red are impregnated.

$60°C$ by means of four cartridge heaters electronically controlled with feedback from the reads of a thermocouple, which was positioned between the two cartridge heaters of the top side of the mould. As already mentioned, inlet for injection was positioned at the middle point of the moulds' bottom surface, while the vents were positioned on the top surface. Air was pulled from the vents creating a vacuum level of 0.05 Bar inside the mould before the injection started, and it was maintained during the process until resin was seen to flow out from the tubes. An image of the final configuration can be seen in figure 3.20.

More than ten beams were produced during the investigation. Some experimental findings will be reported which can be taken as industry experience. Many of the problems should be better studied in academic research, possibly with more instrumented equipment.

Experience with 2 vents

Some initial experiments were done with only two vents, these positioned behind the bearing bores. In this way it was possible to test the hypothesis that the characteristic value for transversal permeability of the laminate was between 1×10^{-11} and 1×10^{-12}. During the experiment, resin was injected until it was seen to flow out from the vents; subsequently the injection and

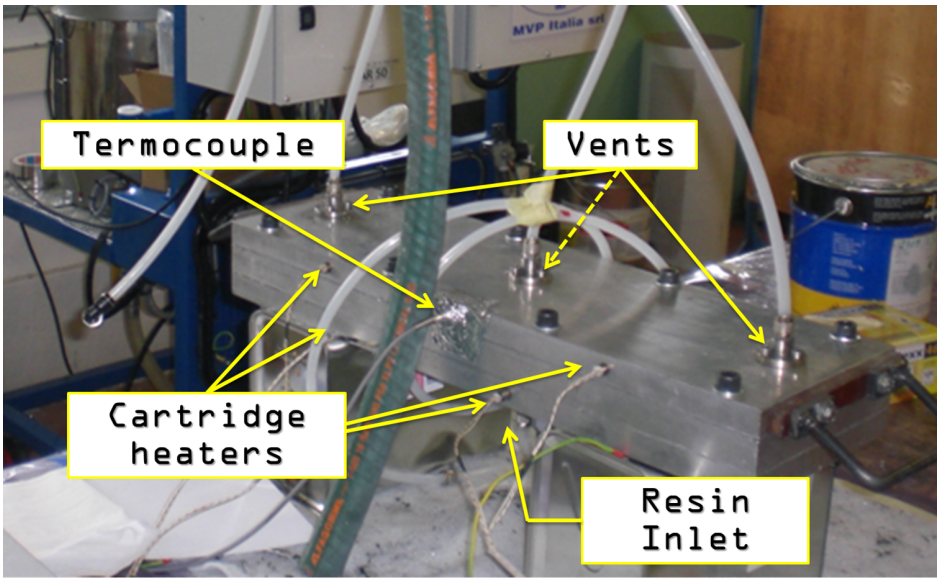

Figure 3.20: Final configuration production of the beam with the RTM process

vacuum tubes were closed to proceed with the curing of the part. After extracting and analysing the part it was observed that the impregnation was not completed. As it can be seen on figure 3.21, which shows the beam from the top and lateral cut-view, some fibres remained dry. Although it cannot be said which was the exact dry portion present at the moment the resin injection was stopped, because the vacuum entrapped by the resin would continue the suction until the pressure stabilizes inside the mould, the dry profile recalls very much the last filling step shown in figure 3.19. This result was considered evidence of a transversal permeability being closer to the lowest value studied with the simulator, confirming that a third vent was necessary. In successive tries the *One Shot* function was used to obtain the exact value of K_3 that changes the dynamics of the flow to introduce the center of the beam as a *last filling sector*, for any K_3 smaller than 3.2×10^{-13} it was seen

Before modifying the mould a new test was put forward. Probably one of the biggest concerns on RTM technology regarding the flow study are the race-track and fibre rearrangement effects, since they are difficult to predict and their effects are still being studied. The following test presents some evi-

Figure 3.21: Top and cut view of beam produced with two vents, dry fibres were found on the top-centre portion of the part

dence of the consequences of such effects, combined with micro-impregnation issues.

The test was performed laying less plies than the corresponding, the objective was to understand if the resin was able to move the fibre layers during the filling. The configuration was similar to the one studied in [133], though the resin inlet was on the bottom side of the mould, instead of on the side.

The mould was closed and heated up to $60°C$, when the temperature stabilized the resin was injected until it was seen to flow out from the vents; at that moment the injection and vacuum tubes were closed to proceed with the curing of the part. Once the mould was opened and the part was extracted, it was seen that the fibres were correctly impregnated, though packed on the top side of the mould, while on the bottom side a lack of resin was observed. To remind the reader, the resin was injected through the bottom side, and the fibres were first placed in contact with bottom plane, for this reason the

result was surprising, one would expect the resin and fibres to fall down by gravity force. Figure 3.22 shows both sides of the resulting beam.

The mechanisms which can explain this result are: at the beginning the

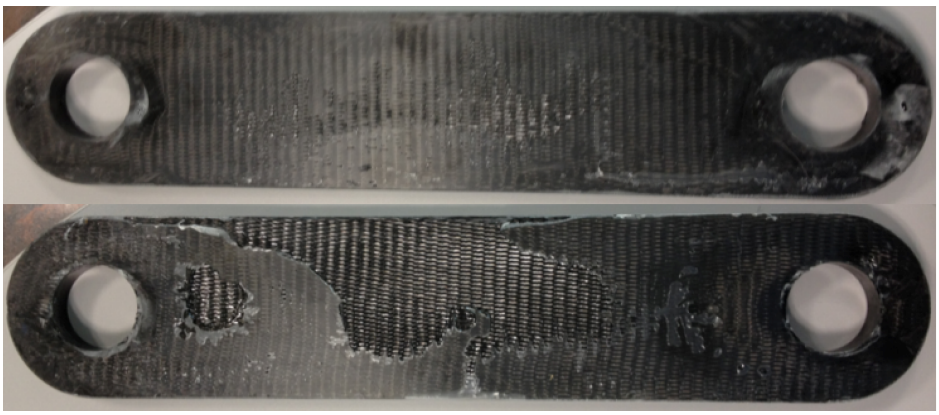

Figure 3.22: Top and bottom sides of beam number three, a resin shortage can be appreciated specially on the bottom side

mould was closed with the fibres on the bottom; successively, when the injection started, the resin moved the layers upwards, helped by the suction applied at the vents. The resin flowed inside the mould and between the layers wetting them macroscopically, until the flow came out from the inlets, moment when the inlet was closed.

In a successive stage and once the resin entrance and vacuum lines closed, the resin started to get absorbed by the remaining vacuum in the dry zones and by the micro-spaces inside the tows of fibres, capillarity forces can help this mechanism. In other words, the preform of fibres acted as a *sponge* absorbing the resin and drying the bottom side of the mould. Capillarity forces and micro-impregnation effects are not included in the simulation code of the software; this result shows that they can play an important role.

This was the last test performed with two vents. The mould was modified before the experiences follow reported. The third vent was positioned on the mid point of the moulds' top surface.

Experience with 3 vents

Without considering resin track and fibre rearrangement effects, having the problem a symmetric configuration, it was expected that the resin would exit from the lateral vents simultaneously, before or after (depending on the permeability tensor) the flow came out from the central vent. In other words, a symmetric result. Instead, it was seen in all production experiments that the resin was exiting from one of the side vents, then from the central one, and finally from the other side vent. The time difference between the exit through the lateral vents was not negligible. It was verified that this was not caused by an inclination of the mould.

Thus, this asymmetric behaviour could only be explained by adding some asymmetries to the problem configuration, and these could be caused by the already mentioned fibre rearrangement and race-track effects. Some effort was done to reproduced this with the simulation software.

In order to add an asymmetry, the following hypothesis was put forward: the resin, when entering at high pressure in the cavity, moves up the fibres and creates a *free-of-fibres duct* through where it could freely move, and this effect not being symmetric, but instead favoured towards one side of the mould. The concept is illustrated in figure 3.23.

Figure 3.24 shows the mesh with the final disposition of the zones. A poros-

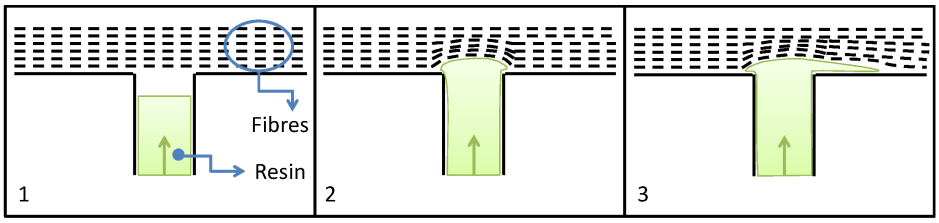

Figure 3.23: The image illustrates the hypothesis made for the last simulation in which the resin creates a race-track towards one side of the mould by compressing the fibres

ity of 100% was assigned to the dark-yellow elements in the centre near the injection point. The flow sequence obtained as result is reproduced in figure 3.25, worth noticing is that this modification allowed the reproduction of the asymmetric exit through the vents.

The need of manual introduction of race-tracking and fibre-rearrangement

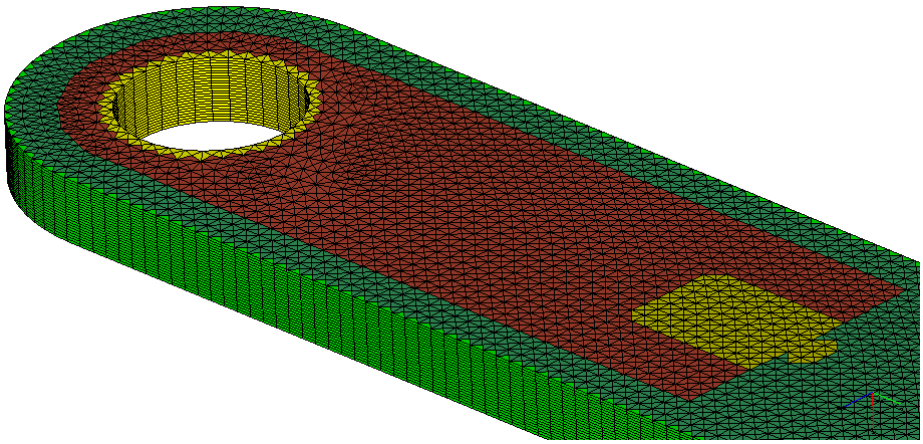

Figure 3.24: Final disposition of the zones in the mesh

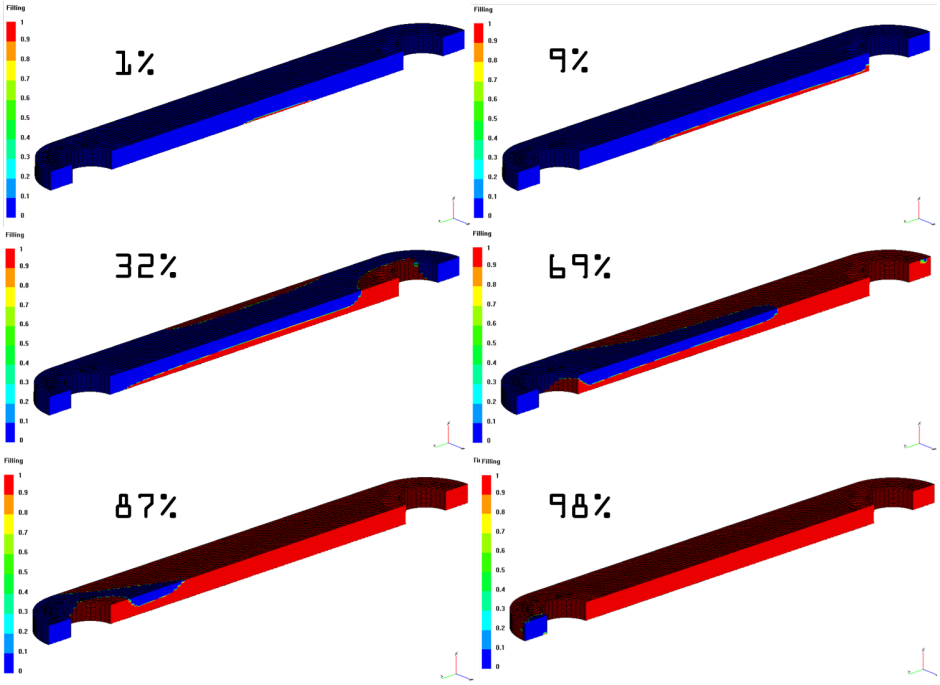

Figure 3.25: Resin flow sequence after the manual introduction of high permeability zones emulating race tracking

effects to reproduce the reality is not a limit of the software itself, but of

the knowledge of the physics behind the problem. One normally expects the simulation to predict the real result, although this is probably a difficult case because of the asymmetric result in an initially symmetric problem, which probably gets asymmetric due to the mentioned effects.
Race track and fibre rearrangement should be studied deeply in order to introduce them as part of the simulation code, since they sometimes play an important role on the result. Some studies on this subject have already been performed (e.g. [134] [133] [135]).

Final compaction to reduce porosity

Figure 3.26 shows the profile of pressure applied by the machine in order to pump the resin, it was recorded during one of the tests with the three-vent configuration. The curve should not be taken as the pressure inside the mould, since there are pressure losses between the machine and the mould.
The curve shows a first peak of pressure as soon as the resin enters the

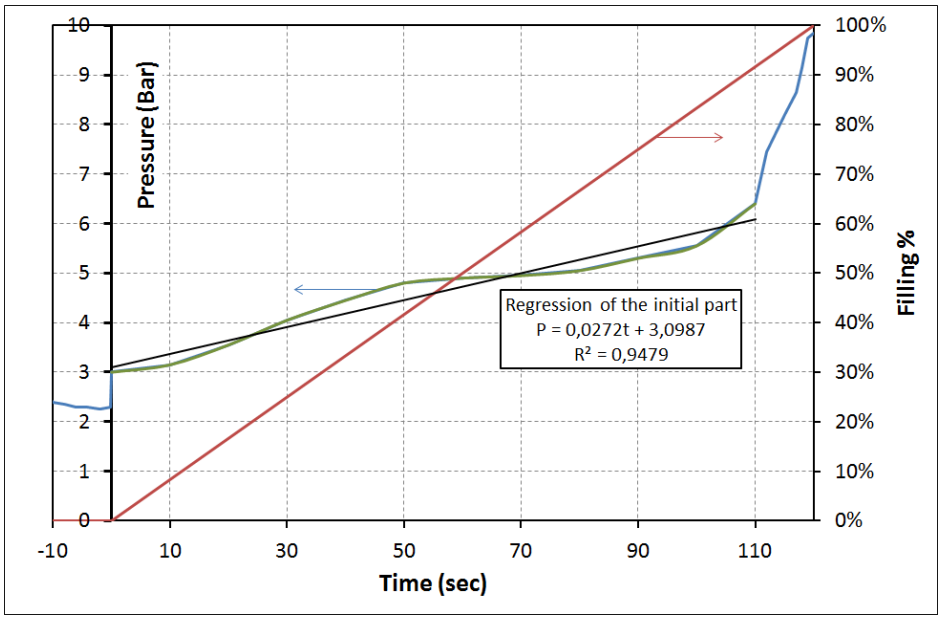

Figure 3.26: Pumping pressure applied by the metering machine and filling percentage of the mould trough time

mould ($t = 0$), where the difference in the traversal area of the tube and the

mould entrance causes a concentrated loss of pressure and a sudden increase of the one needed by the machine in order to pump the resin. From $t = 0$ until $t = 110$ (green curve), the pressure shows a slow increase rate, a lineal approximation results in a slope of 0.027 $Bar/second$. It is only during the last ≈ 10 seconds of filling that the pressure starts to increase faster. This increased effort made by the machine at the end of the process was reduced by making some modifications on the configuration.

In the new configuration, a long transparent tube which allowed the observation of the resin flow, was connected to the inlet, with the opposite end connected to a T-valve. The two other ends of the T-valve were connected to the machine and to compressed air. During the injection the machine entrance was opened while the air one was closed. Once the machined reached the 8 Bar set as maximum allowable working pressure it's entrance on the T-valve was closed in order to open the air access, which pressed against the resin present in the tube, making it flow further and finishing the filling process. This also allowed a final compaction of the resin.

The new procedure permitted to anticipate the release of the machine, making it available for another injection. The effect on the part was a better aesthetic result, especially in the edges as it can be seen on figure 3.27, and a reduction of the porosity.

Regarding the porosity, an Olympus Epoch 1000i instrument with V103-RM contact transducer was used to perform ultrasound A-scan pulse-echo analysis. Water was used for the coupling. The *reference standard* was set to give an end signal of 80% when scanning a plate produced with the prepreg and autoclave process (Filter between 0.5 and 4 MHz and Gain set to 36.7). The signal when scanning the beam produced without using compressed air was varying from 60% to 90%; instead when analysing the last beams produced with the new configuration including the final compaction by means of compressed air, the signal was always over 100% and in some zones reaching 110% (end of scale). Figure 3.28 shows a picture of the scanning process on one of the beams.

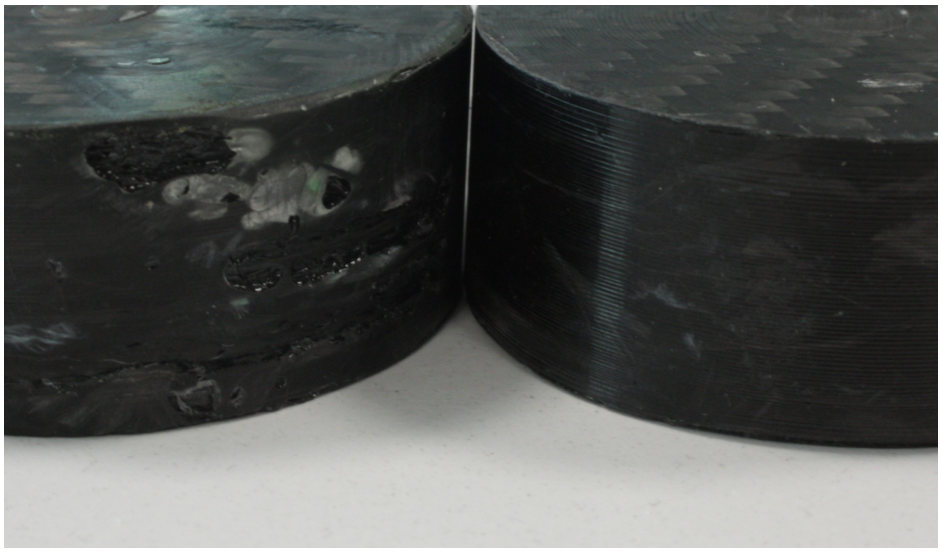

Figure 3.27: Difference on surface finish between parts produced with (right) and without (left) final compaction by means of compressed air

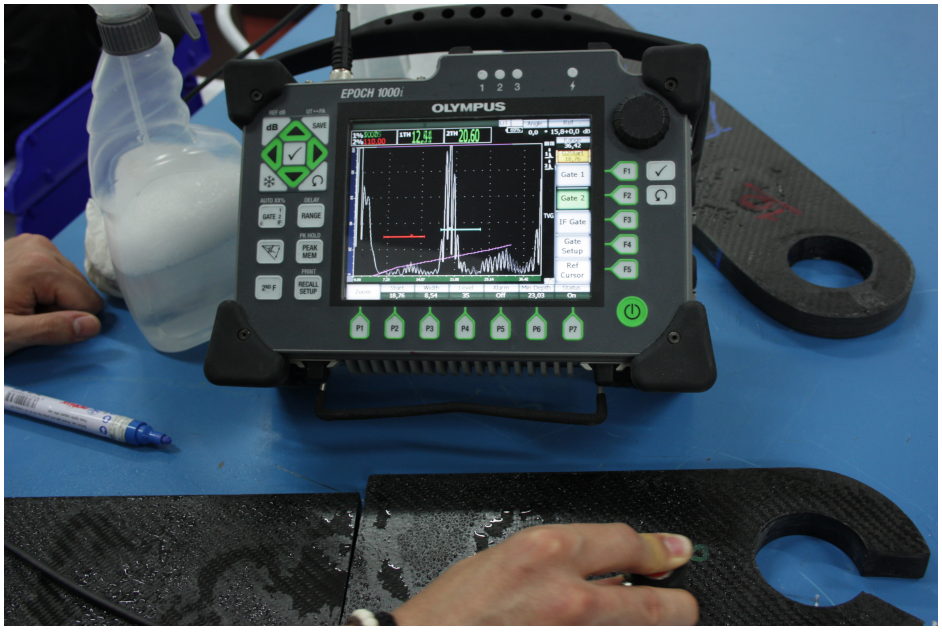

Figure 3.28: Beam under porosity and delamination analysis by A-scan ultrasound method

2.6 Curing Simulation

The curing of a thick part is a critical step of the production process [136], since a big amount of resin is involved. The curing is an exothermic chemical reaction which is faster as the temperature is increased, thus in case the curing process is not correctly studied it could derive in a high temperature increase which could degrade the polymeric matrix and consequently compromise the mechanical performance of the component.
For the current investigation, the curing was studied using Curing module of PAM-RTM software. The simulation results were verified with DSC analysis performed on specimens extracted from the finished component.
A Kamal-Sourour [137] cure-kinetics model was constructed from isothermal DSC analysis as explained in chapter 1. A reaction enthalpy of 374920 J/Kg was obtained from temperature scan DSC measurements.
The model is described in equation 3.5:

$$\frac{d\alpha}{dt} = A \cdot e^{-\frac{E_a}{RT}} (\alpha_{lim}(T) - \alpha)^{p(T)} \cdot \alpha^{m(T)} \tag{3.5}$$

Where $d\alpha/dt$ represents the reaction rate, α is the degree of cure, $\alpha_{lim}(T)$ is the maximum value of α reachable at temperature T, A is the pre-exponential factor, $p(T)$ and $m(T)$ are temperature dependant values characteristic of the resin, E_a is the activation energy of the reaction, R is the universal gas constant and T is the temperature. The values for thermal conductivity and specific heat were provided by the producer of the resin; 0.25 $W/m.K$ and 1200 $J/Kg.K$ respectively.
For the fibres the following characteristic values were used [138]:

- Density = 1700 Kg/m^3
- Effective thermal conductivity = 0.25 $W/m.K$
- Specific heat = 1200 $J/Kg.K$.

Due to the symmetry of the domain and the boundary conditions, a plain model hypothesis was made, where each cross section was assumed to have a similar temperature profile. Hence, a 2D mesh was used, representing the

cross section of the beam between the bearing bores. An outside layer of elements represented the mould. In total there were 10296 elements and 5288 nodes. Figure 3.29 shows the mesh and the position of two sensors, one on the surface of the component and the other inside it at the middle point from the edges. Figure 3.30 shows the simulation results of temperature and cure as a function of time for both sensors.

The surface sensor follows the temperature profile defined as boundary con-

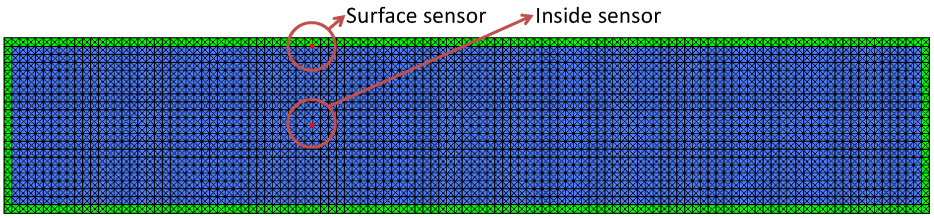

Figure 3.29: 2D mesh used for the curing simulation with the position of two sensors where the temperature and degree of cure are monitored.

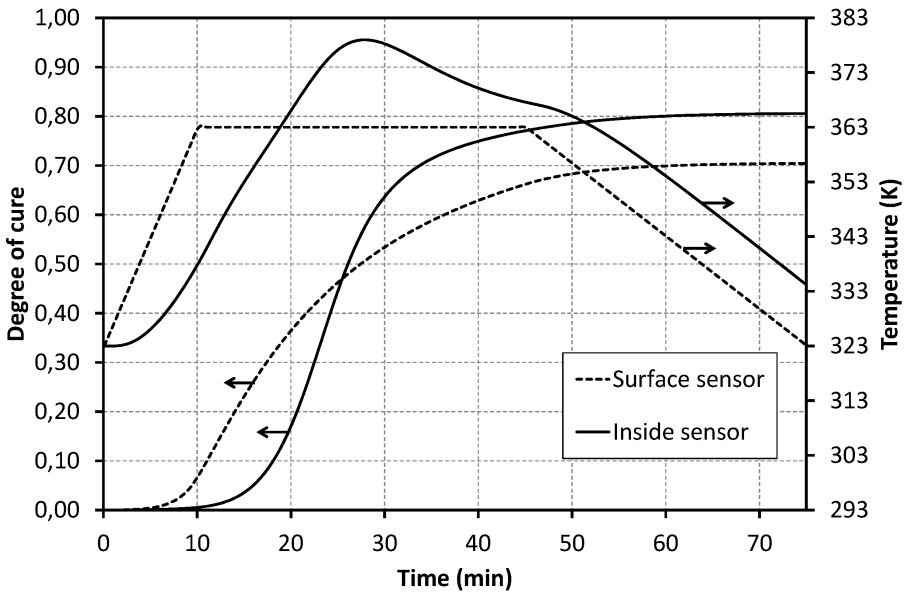

Figure 3.30: Temperature and degree of cure as a function of time for the two sensor positions

dition, the temperature at the inside sensor is lower for the first 19 minutes,

but then runs higher due to the heat generated by the reaction. In terms of cure, the inside of the beam cured quicker than the surface. This 75 minute cycle allowed a sufficient degree of cure in order to perform the extraction of the part in a short time, limiting the temperature below $110°C$; in order to get a homogeneously cured component a post-cure was needed.

2.7 DSC Analysis

DSC measurements were carried out on a TA Instruments Q2000 DSC Modulated apparatus equipped with RCS cooling system. Every sample ($10 - 15$ mg) was heated from $0°C$ to $250°C$ twice at $10°C/min$ in nitrogen atmosphere, with an intermediate cooling run carried out at $20°C/min$. The samples were obtained from two beams treated with the curing cycle presented in Figure 3.30.

They showed in the first scan a slightly different T_g as a function of the position, with a lower T_g ($106°C$) recorded in the external layers and a $5°C$ higher value measured in the inner core (Figure 3.31, green and red lines, respectively). The difference observed is a clear sign of an incomplete curing, at least in the outer shell. As a consequence a post-curing treatment (two hours at $125°C$) was applied to the part, and the results show not only an increment in T_g value up to $119°C$, as reported for the external layer in Figure 3.31 (blue line), but no difference between inner and outer layers (curve not shown due to overlapping). This behaviour implies that the resin was not completely cured upon the first heating cycle, and post-curing treatment was able to drive curing of the resin to higher extent both in the inner and in the outer layers. Hence, results postulated in previous section were fully corroborated by experimental DSC scans of real specimens.

2.8 Mechanical Tests

Interlaminar shear strength

Interlaminar shear strength (ILSS) was tested by means of three point bending mechanical tests, following ASTM standard D-2344 [139]. The specimens were sliced with a diamond saw transversally from two finished beams pro-

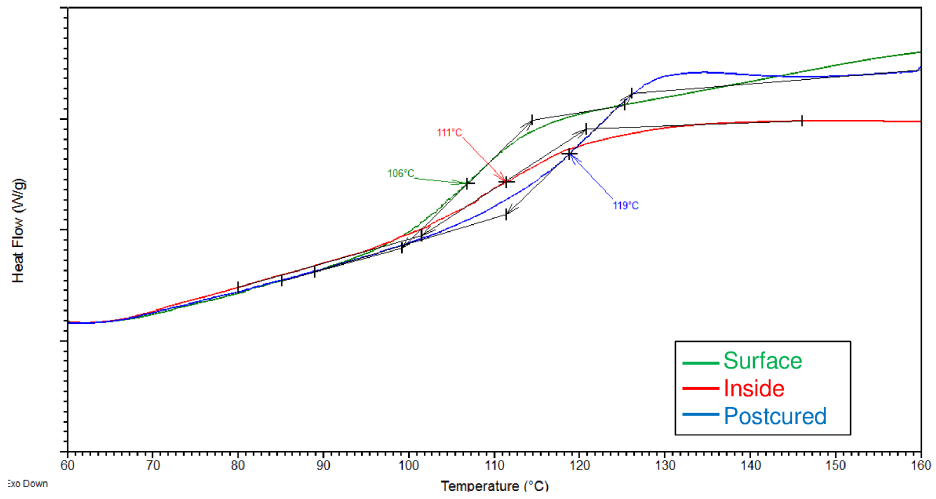

Figure 3.31: Temperature and degree of cure as a function of time for the two sensor positions.

duced with the RTM process (RTM) and from a plate made with the prepreg and autoclave process (PP) with the same lamination sequence. The percentage of fibres in the longitudinal direction was 2.6%, in the transversal direction 60.8% and the rest distributed equally in the 45° and −45° directions. In total 10 RTM and 4 PP specimens were tested, with dimensions of 20×40×120 mm. The machine used was a universal test machine with a load cell of 250 kN.

Results for Force-Displacement curves of one characteristic specimen for each technology are shown in figure 3.32. As it can be seen, PP specimens resisted a higher load. Short beam strength was calculated using Equation 3.6, where P_m is the maximum load observed during test and b and h are the specimen width and thickness.

$$F^{sbs} = 0.75 \cdot \frac{P_m}{bh} \tag{3.6}$$

The following average values were obtained: F^{sbs} (RTM) = 26.7 MPa and F^{sbs} (PP) = 34.1 MPa. The standard deviation of the maximum load was 1.7 MPa for RTM specimens and 1.9 MPa for the PP ones.

This difference between RTM and PP could be caused by some variables

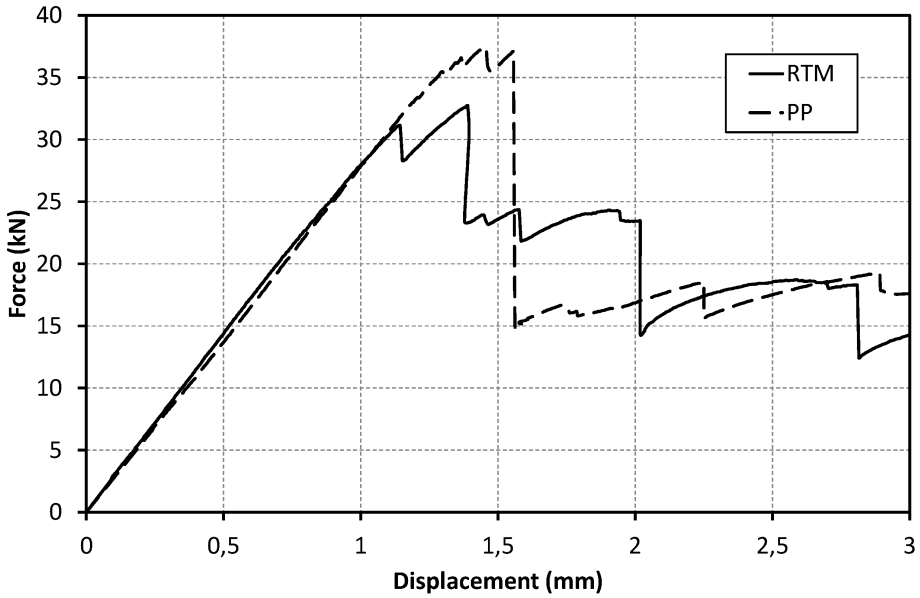

Figure 3.32: Force-Displacement curves for one characteristic specimen of each technology

introduced when changing the process. The fibre-volume fraction, stacking sequence and type of fibres remained the same, the porosity was found inferior for the RTM specimens.

Failure modes were different: while RTM showed first a small crack in tension on the lower layers before the interlaminar shear crack took place, PP showed first the cracks going from the loading nose up to one of the side supports, and then the interlaminar shear crack occurred. The failure modes can be better understood by looking at the images in Figure 3.33 which shows the broken specimens. Figure 3.34 shows the surface where the interlaminar shear failure took place, as it can be seen on both types of specimens the delamination took place within the biaxial layers. A very important difference should be highlighted; while some fibre cracks and fibre bridging can be seen on PP specimen, for RTM a pure delamination was obtained, with no fibre cracks, a clear clue that the interface was weaker. In order to analyse the interface and the impact of one particular product introduced in the new process, the test campaign reported on the following section was performed.

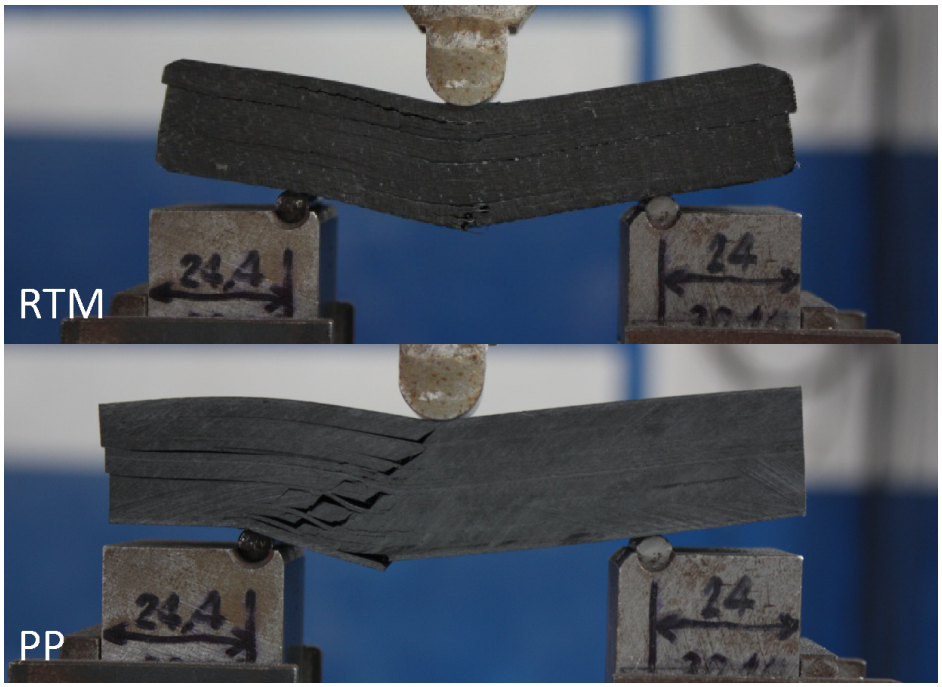

Figure 3.33: Broken profile of RTM (top) and PP (bottom) specimens

Impact of spray tackifier on interlaminar shear strength

When stacking prepregs there is no need of adding adhesives, since the prepregs already have a natural tack given by the resin in β-stage of polymerization. Instead in RTM process, since the stacking of layers is done with dry layers of fibres, they have no tack. Thus two difficulties appear:

- Stacking and keeping the layers together and in position inside the mould becomes difficult
- The layers, specially the unidirectional ones, will *shed* fibres on the sides after they are cut, since the *binder* used in dry fabrics is usually a filament, which is trimmed and left loose during the cut process, this is the most critical aspect.

This is the reason why it is normal procedure to use a process enhancer product known as *tackifier*, which helps on solving both problems. The objective of the experimental campaign that will be reported on this section was to analyse the impact of one of different takifier products on the interlaminar

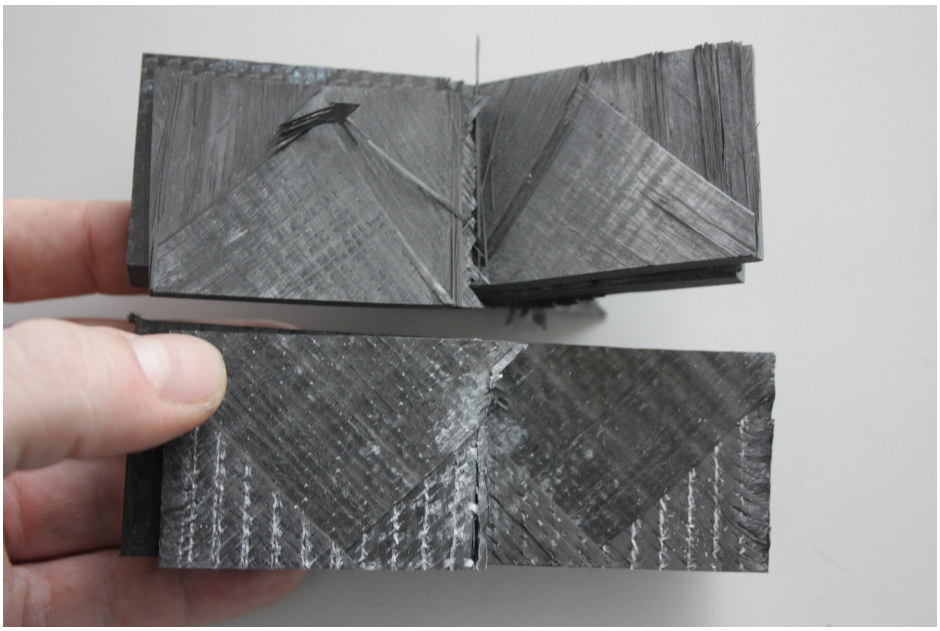

Figure 3.34: View of the surfaces where delamination took place for PP (top) and RTM (bottom) specimens

shear strength of a laminate. All the products tested are commercially available in spray presentation.
With this scope CFRP panels were fabricated using prepreg laminates moulded with two plates and closed inside vacuum bagging before starting the cure process in autoclave. Five different kind of panels were made, to test three tackifier products:

1. Only prepreg
2. Prepreg + AirTack® sprayed every three layers without following the recommended spray distance and wait before placing following layer
3. Prepreg + AirTack® sprayed every three layers, following the procedure recommended by the producer**
4. Prepreg + StayZ® sprayed every three layers, following the procedure recommended by the producer**
5. Prepreg + AeroFix3® sprayed every three layers, following the procedure recommended by the producer**

AirTack®, StayZ® and AeroFix3® are commercial spray tackifier products, all reportedly compatible with epoxy resins.

** Spray distance to the part of minimum 30 cm. Wait after spraying for at least 10 seconds to give solvent the possibility to evaporate. From each panel six specimens were cut, with final dimensions of 20 × 80 × 7 mm, which were tested to obtain the interlaminar shear strength (ILSS) by means of three point bending mechanical tests, following ASTM standard D-2344 [139], as explained before. The span was set to 30 mm.

Figure 3.35 shows one representative result for each case, where F_{sbs} as a function of displacement is plotted. It is possible to see how AirTack® applied without following the guidelines of the producer performed the worst. The same product applied correctly improved the F_{sbs}, though still worse than the base line given by the untreated specimens. The other two products show a behaviour unaffected respect the untreated specimens. The average result of F_{sbs} is shown in figure 3.36, the error lines show the dispersion of the data.

AirTack® affects considerably on the interlaminar shear strength, to the

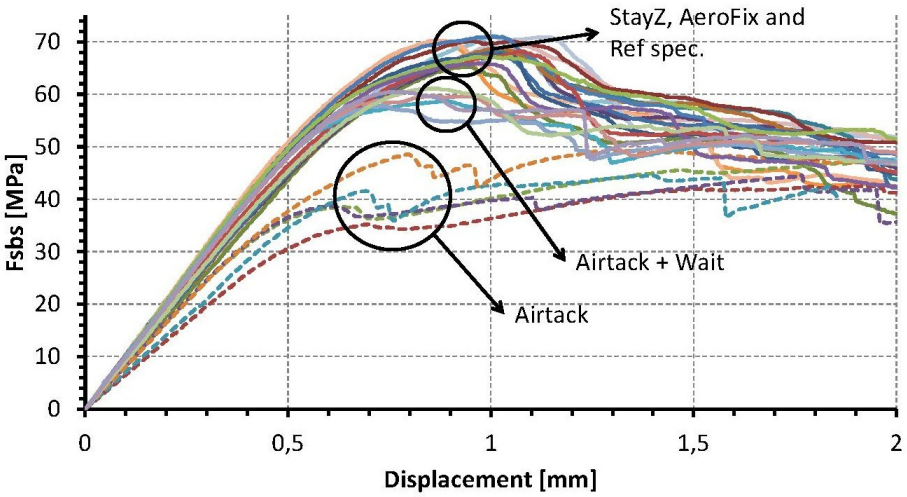

Figure 3.35: F_{sbs}-Displacement curves obtained for one representative specimen treated with different *tackifier* products

point of changing the failure mode. As it can be seen in figure 3.37, the specimens where it has been applied show interlaminar shear failure mode in the

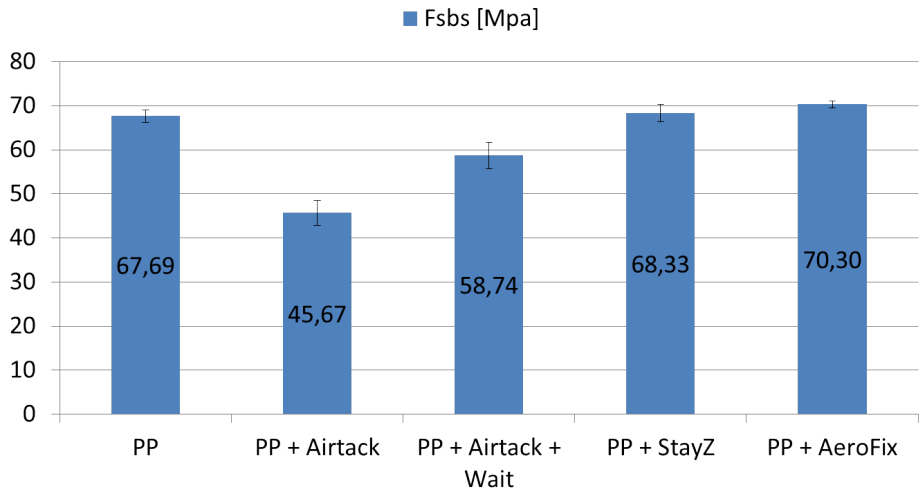

Figure 3.36: Maximum F_{sbs} and standard deviation obtained for each kind of specimen

side, while the specimens treated with the other products and those untreated show inelastic deformation and interlaminar-shear failure mode between the loading nose and the one of the supports. Based on the results of the current experimental campaign it is possible to conclude that the difference between RTM and prepreg specimens shown in the previous section can be minimized by using the appropriate tackifier product. AirTack® is apparently incompatible with epoxy resin, while StayZ® and AeroFix3® can be used with no effects on the ILSS properties of the final part.

Testing of final component

Tensile tests were used to compare finished con-rods made with the RTM production technology with the ones made with the Prepreg+Autoclave method. The configuration of the tensile test can be seen in figure 3.38. The machine used was an Instron 8033 with load cell of 250 kN. The diameter of the stud fixes was 50 mm. The tests were performed on displacement control and the speed was set to 0.05 mm/sec. A compatible tackifier product was used during the production of the beams tested made with the RTM method.

Figure 3.39 shows pictures of the broken con-rods, as it can be seen in both

(a) (b)

(c) (d)

Figure 3.37: Images of typical specimens of *(a)* untreated specimens, *(b)* specimens where StayZ® or AeroFix3® was applied, *(c)* specimens where AirTack® was applied without waiting for volatile chemicals to evaporate and *(d)* specimens where AirTack® was applied as recommended by producer.

cases the failure was caused by contact pressure, which also caused delamination, this was the same failure mode seen on the con-rods produced with Prepreg. Figure 3.35 shows the contact pressure to axial displacement curves. The beam produced with the RTM method performed slightly better than the Prepreg ones, although this difference could be a result of the reduced porosity they can also stand within the test variability, the performance can be taken as equal. In any case this is a good result considering the advantages of RTM method in terms of processing time.

The failure mode of contact pressure could be avoided to improve the performance of the beams by adding a metallic bushing in order to increase the contact area with the CFRP. Moreover, in case of excessive contact pressure the metallic bushing can plasticize and deform before final failure. This is actually the normal procedure on this kind of beams, where the bushings are adhesively bonded in a successive step of production. The interesting point with the RTM process is that it is possible to insert the bushings inside the mould and obtain the final part in one step. Some good results in this direction have been obtained, figure 3.41 shows a finished con-rod with the bushings, though this is still preliminary work.

Figure 3.38: Configuration of the tensile test of the finished component

2.9 Conclusion

The section presented the case of a con-rod beam, a thick CFRP part which was produced using the RTM method. For both injection and curing, results of simulations performed with PAM-RTM were presented and compared to real experiences. It was found that the resin flow during injection could be rather unpredictable, probably because of the fibre rearrangement and race tracking effects. An asymmetric solution on a symmetric problem was ob-

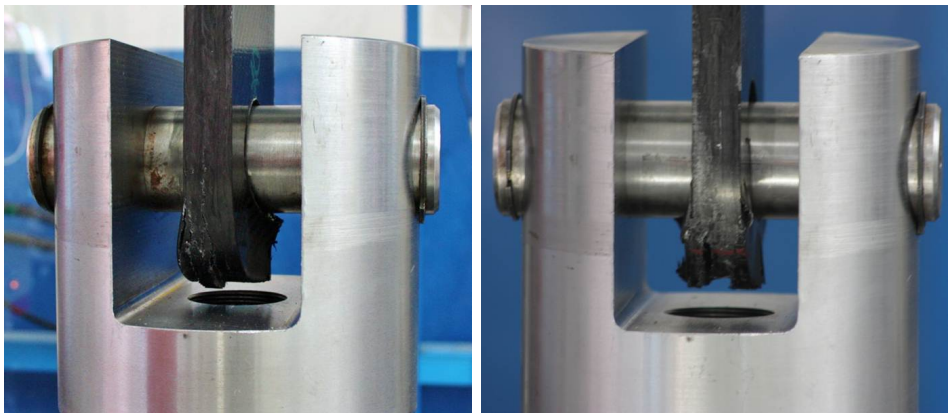

(a) (b)

Figure 3.39: Broken components produced by RTM tested on tensile test

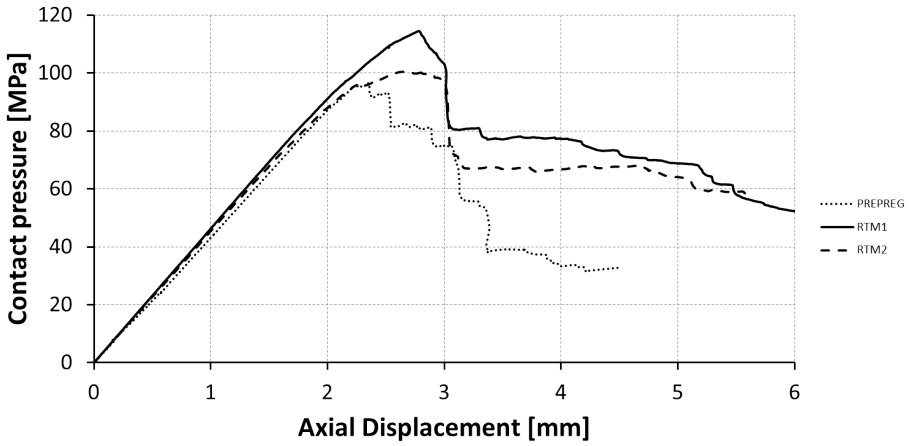

Figure 3.40: Force-Displacement curves for the tensile tests on the full components made by RTM and Prepreg technologies

tained. This effect could be reproduced using the software by manually applying asymmetries that emulated the effects mentioned above. Results from the experience also showed the improvements in terms of aesthetic aspect and porosity of the part that could be achieved by applying an end compression of the resin by means of compressed air.

Regarding the curing of the part, the simulation of a 75 minutes curing cycle was presented, the results were corroborated by means of DSC measurements. This cycle was designed to obtain a quick curing without causing and exces-

Figure 3.41: Con-rod beam produced by RTM integrating the metallic bushings inside the mould

sive exothermy, which would decrease the mechanical properties of the final component.
Results of mechanical tests were also presented, performed on specimens produced by RTM and compared to others produced with the prepreg and autoclave method. In particular, the impact of a process enhancer product normally used in industry has been studied, showing that it can have a substantial influence on the mechanical performance of the resulting product. On other tests i.e. tensile, RTM components showed comparable results with Prepreg ones in terms of maximum load before failure.

Chapter 4

Composite Products

1 DESIGN OF COMPOSITE STRUCTURES

DESIGN RULES FOR COMPOSITE SANDWICH WAKEBOARDS

1.1 Introduction

Wakeboarding is a sport born in the mid 80s that derives from surfing and water skiing. The necessary equipment consists of a board with two bindings where the user's feet are fixed; the system user-bindings-board is pulled by a boat through a rope held by the user. The boards design has been improved throughout the years, usually following a trial and error procedure where the shape performance evaluation is based on the riders' feelings only. Current boards allow professionals to perform jumps over four meters in height. Figure 4.1 (left) shows a professional wakeboarder performing a jump.

In order to keep the weight as low as possible, boards are usually made with a composite sandwich structure. The core is usually made by plastic foams; the most used is polyurethane, since it can be fabricated on the designed shape by the RIM (Reaction Injection Moulding) process. Only a few boards are made by PVC foam cores, due to the major difficulties to shape.

The faces are later joint to the core using the compression moulding process, with dry fabrics (e.g. carbon or glass fibres) as reinforcement and a thermosetting resin as matrix material. For finishing and aesthetic purposes, boards are covered by a non-structural outside plastic layer. Figure 4.1 (right) shows the typical construction of wakeboards.

The total board weight is about 3 kg. In order to improve the wakeboard

Figure 4.1: Left: Pro Wake-boarder performing a jump Right: Wakeboard components

technology, a weight reduction is needed since lighter boards are easier to manoeuvre. As a rule of thumb, a reduction in weight usually leads to weaker structures. Thus, an accurate structural strength optimization has to be performed to be able to design lighter boards.

Some improvements on this design aspect have been recently seen. Most of them based on a trial and error procedure where prototypes are tested on the field to experimentally verify their structural strength and performance. This is the first systematic study on the structural design of wakeboards; there is no evidence of any other published paper where the design of this product is studied. A number of papers regarding other kind of sport boards can be found, especially on snow sports like skiing and snowboarding [140, 141, 142, 143, 144, 145]. Even if snowboards, skis and wakeboards are all usually made as a sandwich structure, it is not possible to follow the same design rules due to the different surface where they are used: snow in the first two cases and water in the last case. In 2003, Kawai, Otani and Sakata [146] developed a simulation approach for estimating a ski turn, justifying the numerical approach by comparing with experimental results. Also in 2003, Brennan, Kollar and Springer [143] developed a computer code that simulates the mechanics of a snowboarder travelling down on an S-shaped course; this model can be used for comparing different snowboard designs. Recently, Scott et al. [144] measured the pressure on a ski by using load cells and pressure sensors.

This work presents an experimental, numerical and analytical study of the

water-entry problem of wakeboards. The objective is to give reliable and practical formulas for the damage-tolerant design of sandwich structured wakeboards.

The analysis of a board failed in service is initially presented, followed by the experimental investigation of three-point-bending tests on specimens obtained from a finished board to investigate the failure mechanisms. Fully coupled SPH/FEM numerical simulations of the slamming event are later presented. The analysis focuses on the impact-induced loads during the first instants of the contact, when the hydroelastic loads are higher. Due to the high non-linearity of the slamming phenomena, a numerical model capable to correctly account for the fluid/structure interaction is needed [147, 148, 149]. The commercial explicit non-linear code Ls-Dyna was found to be suitable for this purpose, especially when dealing with hydroelastic impacts [147, 150, 151, 152, 153, 154, 155].

The numerical solutions show that there is a limit in the maximum deformation of the board that will never be overreached even for very high impact energies. The maximum deformation is found to be determined by the board's undeformed geometry. Starting from this considerations, classic sandwich theory is used to investigate the stresses in the structure. As result of this research, useful guidelines on the effects of total mass, initial impact velocity, core and face strength and thickness are outlined to give reliable design rules.

It was found that the the structural optimization of the board should start

Table 4.1: List of formulas to use during the wakeboards' design phase.

Component Property	Formula
Core minimum compressive strength	$\sigma_c \geq \pi \rho V_0^2 R \frac{b}{A} K_g$ $K_g = 1 - e^{-\frac{\beta L_b}{2}} cos \frac{\beta L_b}{2}$ $\beta = \sqrt[4]{\frac{E_c}{4 D_f d}}$
Core min. shear strength	$\tau_c \geqslant \frac{G_c}{R} l$
Core max. thickness	$t_c \approx d < R \sqrt[3]{\frac{E_c G_c}{E_f^2}}$
Face min. thickness	$t_f \geq \sqrt{\frac{dL^2}{2R\pi^2}}$
Faces min. strength	$\sigma_f \geqslant \pm \frac{E_f d}{2R}$

b	Board width
ρ	Density of the water
A	Binding Area
l	Distance between the bindings
d	Distance between faces neutral axis
L_b	Binding longitudinal length
D_f	Face flexural modulus
L	Allowable delamination length
R	Radius of curvature
V_0	Impact velocity
E_c	Core compressive modulus
G_c	Core Shear modulus
E_f	Face Elastic modulus

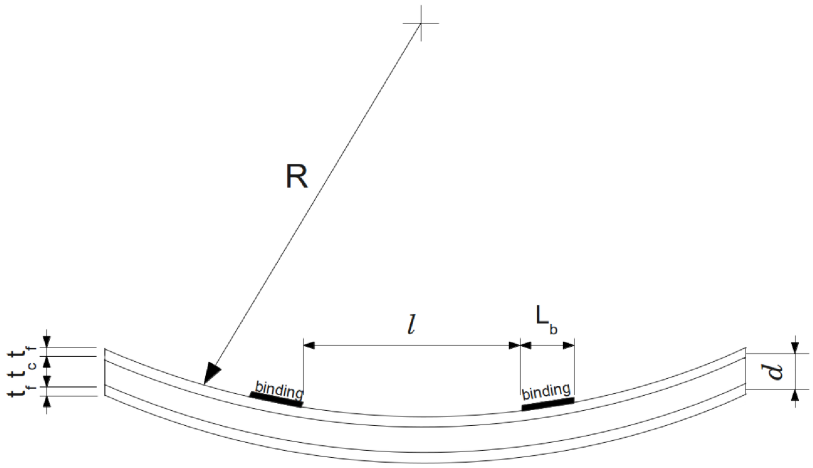

Figure 4.2: Sketch of the simplified model of the wakeboard used for the approximations of the analytical model

from the evaluation of its maximum curvature, since the radius of curvature R governs all the stresses in the structure. Knowing R, indications on the core and faces materials strength, stiffness and dimensions can be easily found applying the formulas presented in table 4.1. In the following sections we present the experimental, numerical and analytical studies that permitted to develop these criteria.

1.2 Failure Analysis

The first step of this work was to analyse a wakeboard that failed during normal use. According to the information provided by *Neptune*[1], the most common failure mechanisms are: *(i)* permanent deformation due to local indentation below the bindings and *(ii)* delamination at the core/face interface. From a first visual analysis of the failed board it was clear that the maximum damage was located below the lower face, between the center of the board and the rear binding. The board was sliced in the transversal direction into pieces to analyse the distribution of the damage. Figure 4.3 shows an extended crack in the core right below the lower face that extends for almost half of the board width. It was localized at 10 cm from the center of the

[1]Wakeboard manufacturing company with more than 15 year experience in the field.

board in the direction of the back binding.

Microscope analysis showed no fibre cracking, neither resin break. A thin

Figure 4.3: Section of the failed board and failed region

layer of polyurethane remained attached to the face matrix, while the rest of the foam looked undamaged. This reveals that the manufacturing production was accurate, and the skin/core delamination was not caused by a bad adhesive bond. This kind of failure could be related to face wrinkling. The core in a sandwich structure acts as a support for the faces preventing them to buckle independently of each other, but if the core is eventually unable to sustain this support it results in wrinkling. Another possible mechanism that would result in a similar failure could be a local buckling of the face loaded in compression. However, this phenomena can appear only if a core/skin delamination is already present (caused by a bad manufacturing process or a severe use of the board).

1.3 Experimental test

Three point bending (TPB) mechanical tests were performed on the specimens obtained from the original board. The mechanical properties of the specimens are listed in Table 4.2. The bottom surface of the board was not planar: it presented a curvature that allowed to get specimens of different thickness varying between 20 mm and 40 mm. All specimens were 55 mm width and 240 mm long. TPB fixture span was set to 122 mm and the load

was applied by a cylindrical punch with a diameter of 60 mm that was set to move at a constant speed of 0.02 mm/sec.

Two different kinds of failure were observed: *(i)* core breakage and *(ii)*

Table 4.2: Material properties. $\bar{\sigma_x}$ is the ultimate longitudinal strength, $\bar{\sigma_y}$ is the ultimate transversal strength and $\bar{\tau_{xy}}$ is the ultimate in-plane shear strength.

	Thickness [mm]	E_x [GPa]	E_y [GPa]	G_{xy} [GPa]	$\bar{\sigma_x}$ [MPa]	$\bar{\sigma_y}$ [MPa]	$\bar{\tau_{xy}}$ [MPA]
Upper layer[2]	1	19.5	19.5	1.9	331	97	159
Core[3]	30-40	0.06	0.06	0.022	1.5	1.5	0.76
Lower layer[4]	1	17.5	9.5	5.6	365	365	34.5

face wrinkling. In case of core breakage, the ultimate force ranged between 2.2 and 3.1 kN, depending on the core thickness.

Face wrinkling always started in the compressed face close to the punch. This is the characteristic failure mode of the thicker specimens, since the compressive stress in the faces is higher. Core breackage was characteristic of the thinner specimens. Figure 4.4 shows the characteristic Load-Displacement results of the two failure modes.

Figure 4.5 shows the two different failure modes described before: core breakage (left picture) and face wrinkling (right picture).

1.4 Numerical model

In this section it is presented the numerical model [5] used to investigate the impact-induced structural deformations during the water entry of wakeboards. For all the numerical simulations the explicit nonlinear commercial code Ls-Dyna was used. First, the model was tuned up by comparison with

[4]Properties are taken from the material data sheet: *Fiber Type: E-Glass,* $0°/+45°/-45°$ *Triaxial. Dry Weight: 668.0 g/m°*. Resin content 50 % in volume.

[4]Polyurethane foam H60.

[4]Properties are taken from the material data sheet: *Fiber Type: E-Glass,* $0°/90°$ *Biaxial. Dry Weight: 607.7 g/m°*. Resin content 50 % in volume.

[5]Numerical model courtesy of Riccardo Panciroli

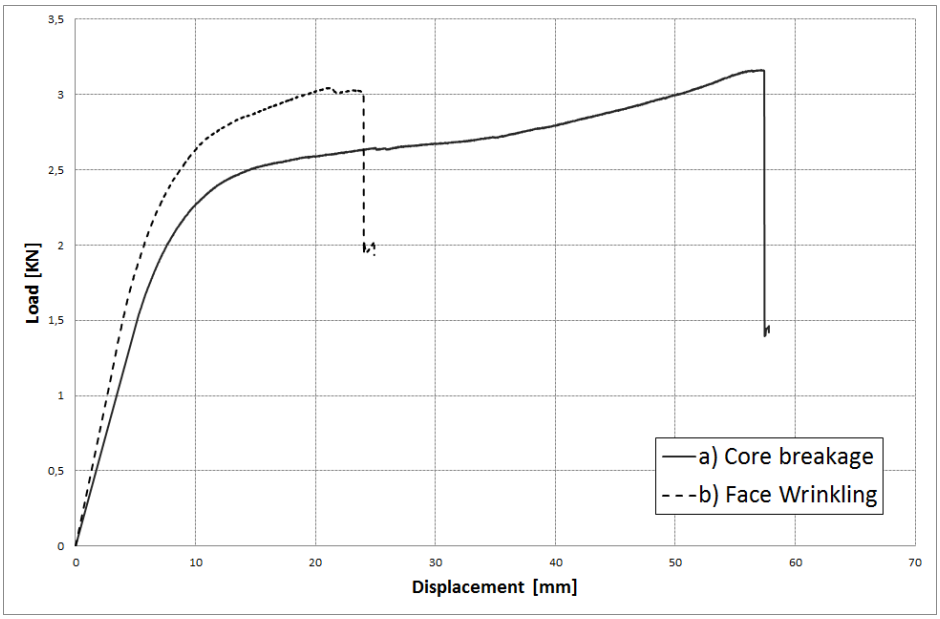

Figure 4.4: Experimental results (a: core breakage, b: delamination and face wrinkling)

Figure 4.5: Failure mechanisms obtained during experimental tests: core breakage (left) and face wrinkling (right)

the TPB experiments showed in section 3. Second, the entire system water-wakeboard was implemented. Results about a parametric study varying the impact velocity are presented in this section. The numerical model used to simulate the slamming event was simplified to a 2D problem, where the central section of the board is considered. Figure 4.6 shows a sketch of the model used for the simulations.

During the real slamming event, the water is forced to flow away from the impact zone in every direction. However, since the curvature of the wakeboard along its width is negligible compared to the curvature along its length, the water escaping from the sides is negligible compared to the water flowing on the fore-side and the backside. Thus, the boundary effects neglected by treating the water impact as a two-dimensional problem are considered negligible. This is a common approach used in water entry problems.

The Smoothed Particle Hydrodynamics method with particles of constant

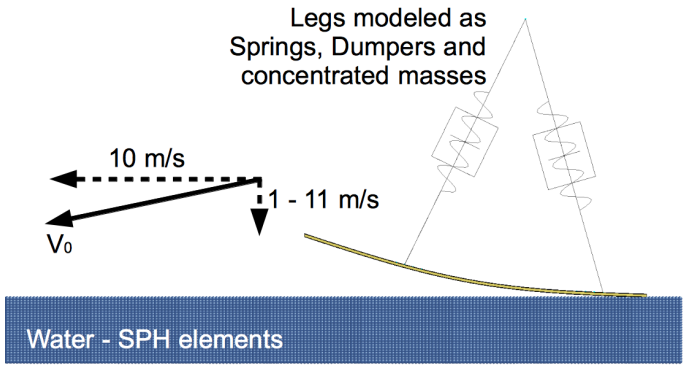

Figure 4.6: Sketch of the model used for simulations

diameter of 5 mm was used to model the water. A Water domain 3 m long, 1 m depth and unit width was modelled. The total number of particles was 120000. Water was modelled as an incompressible medium. To model the fluid, an equation of state (EOS) needs to be defined in LS-Dyna. In the literature the most used EOS is the Gruneisen model, which follows the formula:

$$p = \frac{\rho C^2 \mu \left[1 + \left(1 - \frac{\gamma_0}{2}\right)\mu - \frac{a}{2}\mu^2\right]}{\left[1 - (S_1 - 1)\mu - S_2 \frac{\mu^2}{\mu+1} - S_3 \frac{\mu^3}{(\mu+1)^2}\right]^2} + (\gamma_0 + a\mu)E \tag{4.1}$$

Where $\mu = \eta - 1$ (η is the ratio between initial an final density), C is the bulk speed of sound, ρ is the density of the fluid. In the literature there are many EOS and relative constants sets that are capable of correctly modelling the water behaviour (see e.g. [156, 157, 158]). In this work we used the values presented in table 4.3, taken from [158].

Table 4.3: Gruneisen EOS constants used for the water.

C $[m/s]$	S_1	S_2	S_3	ρ $[kg/m^3]$	γ	a	E
1480	2.56	1.986	1.2268	1000	0.5	0	0

Parabolic Solid elements of unit width were used to model the sandwich board. Faces and core elements were rigidly connected since they shared the boundary nodes. The sandwich structure was considered to have constant thickness along its length; faces were 1 mm thick and the core was 20 mm thick. Faces and core properties used are presented in Table 4.2.
The human body was simplified as three concentrated masses: two masses of 3 kg each (representing an equivalent mass for foot and binding) were rigidly jointed to the upper facesheet; the third 70 kg mass (representing the body) was located 900 mm above the board on the middle span and was connected to each of the other two masses by a spring and a dumper to simulate the human legs. The two springs were of the same stiffness of 22 N/mm and the two dumpers were also equal with viscous coefficient value of 0.2. With these values a body of 70 Kg falling at the velocity of 10m/s stopped in 60 ms, while the center of mass maximum vertical displacement was 350 mm.
Figure 4.7 shows the comparison between the numerical simulation result and a real sequence taken from the Wakeboard DVD called 'The truth' [159], where slow motion scenes were filmed using a Phantom hi-speed camera. Observing the structural deformation during slamming it is possible to see that the board, originally presenting a curved shape, bend up to a completely flat configuration. On this configuration the upper layer is tensioned while the bottom one is compressed.

A parametric study varying the water-entry (vertical) velocity has been carried out. Figure 4.8 shows the comparison of the stresses over time at the middle span of the bottom face sheet of the board. The results can be better analysed in Figure 4.9, where the stresses are presented over the equivalent wetting time.

A summary of the maximum compressive stress as function of the impact velocity is shown in Figure 4.10; here, results of another simulation done with a second board design with three times higher bending stiffness are also presented. The results are presented as the maximum stress for a given

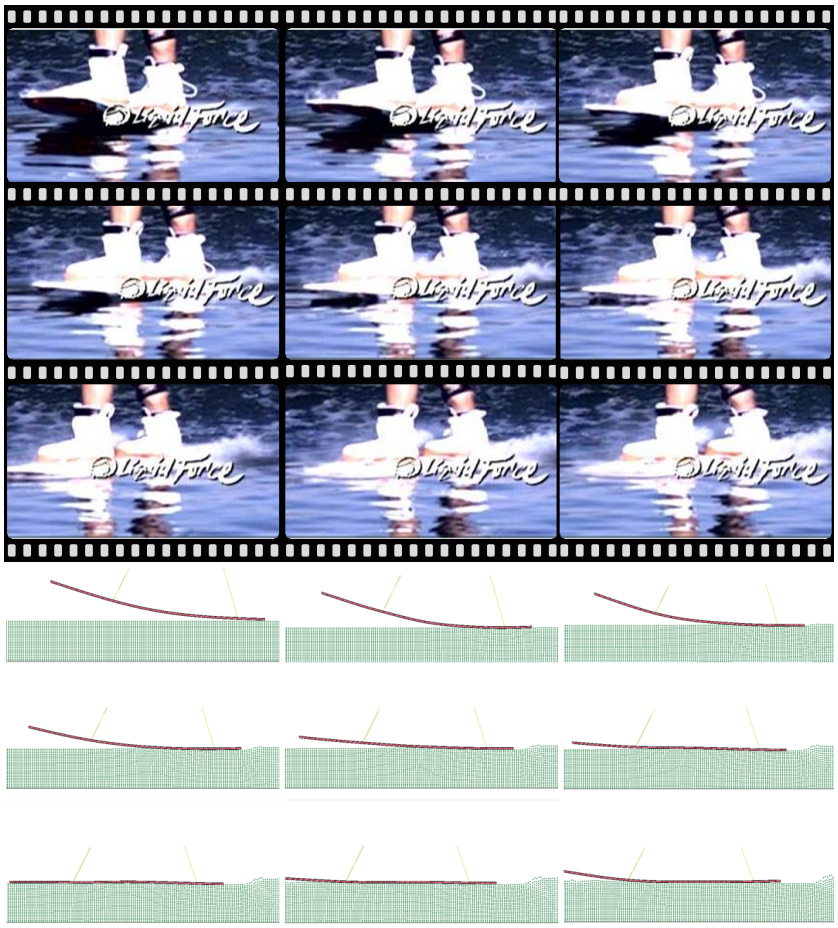

Figure 4.7: Comparison between recorded wakeboard slamming event and numerical simulation

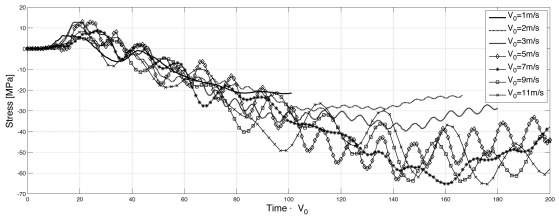

Figure 4.8: Stresses over time at the middle span of the bottom face sheet

impact velocity over the higher stress obtained for a given bending stiffness. Note that the maximum compression in the faces initially increases with the square root of the vertical impact velocity (proportional to the impact energy), up to a value beyond which the maximum compressive stress remains

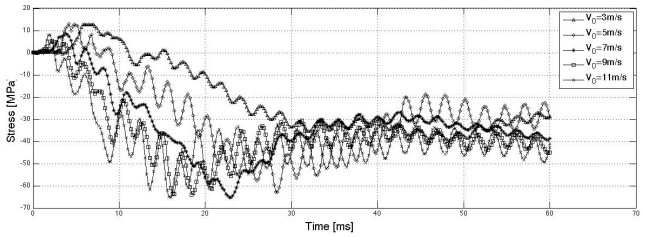

Figure 4.9: Stresses vs. equivalent wetting time at the middle span of the bottom face sheet

constant. This behaviour is caused by fluid and structure interactions that do not allow the board to deform exceeding the flat configuration. It results that there is an impact velocity threshold for each board design, beyond it the board always reach the flat geometry, but will never deform to a negative curvature. Switching from a weaker board to a stiffer board we observed an increase in the threshold impact velocity that resulted into the complete flattening of the board but, still, this maximum deformation could not be overreached.

A different response was found in the core: an increase in the impact velocity

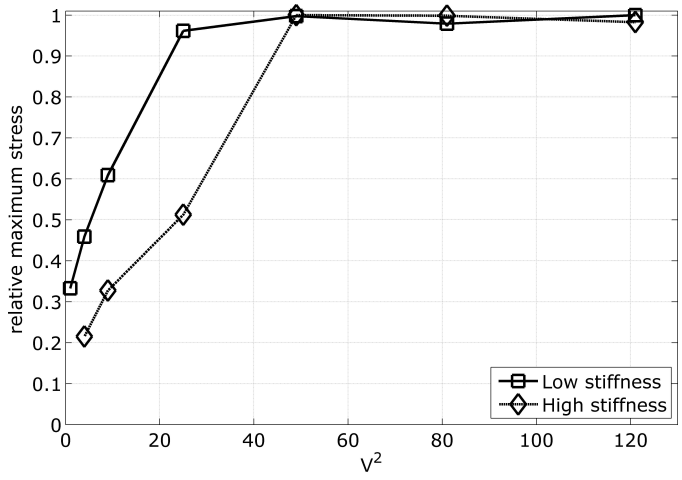

Figure 4.10: Summary of the relative maximum stress in the bottom face over the square of the vertical impact velocity

was always leading to an increase of the compressive stresses in the core. Figure 4.11 shows results of the maximum compressive stress in the core

under the rear binding for the original simulation. It has to be pointed out that the numerical results showed that the maximum compressive stress in the core was not reached when the board was at its maximum deformation (flat configuration in the worst cases), but close to the beginning of the impact. The maximum stress was located right below the rear binding: it increased with the vertical impact velocity and its maximum was reached right after the beginning of the impact, when the impact load was mostly carried by the rear foot and the hydrodynamic force was at its maximum, as better explained in the next section.

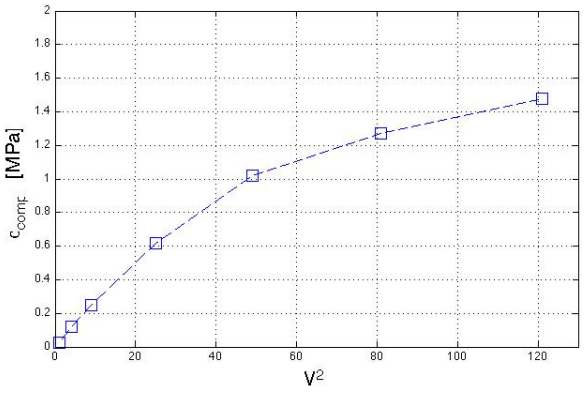

Figure 4.11: Maximum compressive stress in the core below the rear binding

1.5 Design criteria

From the numerical simulations it was found that the maximum curvature of the board is the only parameter affecting the maximum strain of the faces, since the maximum deflection that can be reached during the impact on the water is the completely flat configuration.
In the next sections it will be described how, knowing the maximum curvature of the board, it is possible to know the maximum stresses in the core and in the faces to be used in the design process.

Core compressive minimum strength

Assuming that the wakeboard presents a uniform curvature, it is possible to evaluate the hydrodynamic force the board is subjected during the water entry using Von Karman's formula for cylinders [160]. Von Karman considered a cylinder of unit thickness, density ρ_s, and radius of curvature R entering the water (with density ρ) with initial velocity V_0. Von Karman model is based on some simplification, i.e.: *(i)* inviscid and irrotational flow, *(ii)* surface tension, gravity and structural elasticity effect neglected. In this method, as the body hits the water it is assumed that the mass of a half disk of water of radius r is moving with the cylinder, resulting in an added mass $m = \frac{\pi}{2}\rho r^2 = \frac{\pi}{2}\rho\left(2\xi R - \xi^2\right)$, where ξ is the penetration depth and R the Radius of the cylinder. Then, velocity and acceleration of the body can be evaluated by:

$$\dot{\xi} = \frac{V_0}{1 + \frac{\rho}{\rho_s}\left(\xi/R - \frac{\left(\frac{\xi}{R}\right)^2}{2}\right)} \tag{4.2}$$

$$\cdot\xi = -\frac{\left(MV_0\right)^2}{\left(M+m\right)^3}\frac{\pi}{2}\rho\left(2R - 2\xi\right) \tag{4.3}$$

The motion of the cylinder and the hydrodynamic force are defined by Eqs. 4.2 and 4.3. The maximum force is reached as soon as the cylinder makes contact with the surface of the water ($\xi = 0$, so $m = 0$), and its value is:

$$F = \pi\rho V_0^2 R \tag{4.4}$$

Eq. 4.4 shows that the maximum force increases with the square of the velocity and the radius of curvature, and it becomes infinite as the radius of curvature tends to infinite (flat structure). It has to be noticed that the maximum force is independent from the mass of the cylinder. Furthermore, as previously said, the maximum impact force acts at the beginning of the impact, when the board is still undeformed. Thus, to evaluate the maximum hydrodynamic force acting on the board it is possible to consider the board as a rigid body without introducing any approximation, since its eventual deformation does not affect the maximum impact force.

Considering that at the beginning of the impact only one foot is carrying the entire load ($q = F\frac{b}{A}$), the core compressive strength should satisfy the following equation:

$$\sigma_c = q \cdot K_g = \pi \rho V_0^2 R \frac{b}{A} K_g \tag{4.5}$$

where, σ_c is the minimum compressive strength of the core, b is the width of the board, A is the area below the binding where the load is distributed, and K_g is a constant that depends on the geometry and materials of both the core and the top face. It has to be remarked that the mass of the user and the length of the board do not have any effect on the maximum compressive strain in the core during the initial stage of the impact.

As an example, Figure 4.12 shows the corresponding distributed load q on

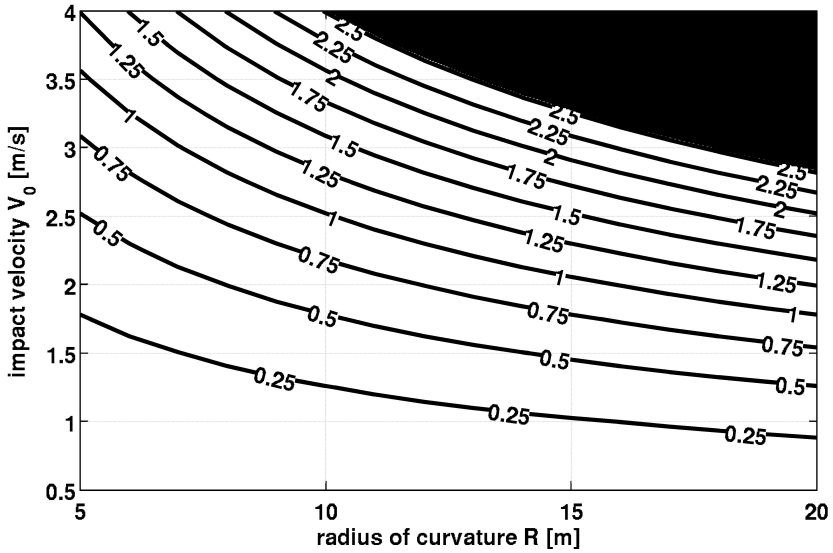

Figure 4.12: Example of maximum compressive stress q in the core varying the radius of curvature and impact velocity. Values are in MPa

the top face for a wakeboard 0.45 m width and a binding that distributes a uniform pressure over an area of 0.08 m^2. The pressures are expressed in MPa. The maximum compressive stresses q assume relatively high values, which most classic foam cores might not sustain. However, these values need

to be corrected by a factor K_g that takes into account the redistribution of the loading in the core. The effective area where the load is spread is wider than the area covered by the binding itself that was used for the calculation of q.

As previously done in the literature, it was possible to evaluate K_g considering the top face as a beam on an elastic foundation (see e.g. [161, 162, 163, 164, 165]). In this model we considered the binding to transmit a distributed load ($F = \int_0^{L_b} q dx$) over the upper face that was considered as an infinite beam laying over an elastic foundation i.e. the core. Figure 4.13 shows a representation diagram of the model. The solution of this model was provided by Timoshenko [166].

$$\Delta w = \frac{q}{k}\left(1 - e^{\left(-\frac{\beta L_b}{2}\right)}\cos\left(\frac{\beta L_b}{2}\right)\right) \tag{4.6}$$

Where $\beta = \sqrt[4]{\frac{k}{4E_f I_f}}$, L_b is the effective length of the binding that transmits the pressure to the board, q is the pressure on the top face and $k = \frac{E_c}{t_c}$ is the elastic constant of the core.

The maximum displacement of the face is located at the center of the binding and corresponds to the maximum deformation of the core. Rearranging Eq. 4.6 we obtain:

$$\Delta w \frac{k}{q} = \frac{\Delta w}{t_c}\frac{E_c}{q} = \frac{\sigma_c}{q} = \left(1 - e^{\left(-\frac{\beta L_b}{2}\right)}\cos\left(\frac{\beta L_b}{2}\right)\right) = K_g \tag{4.7}$$

As title of example of design procedure, here and in the next sections two different face materials will be used: Carbon Fibre Reinforced Plastics (CFRP, $E_1 = E_2 = 60\ GPa$) and Glass Fibre Reinforced Plastics (GFRP, $E_1 = E_2 = 20\ GPa$).

Figure 4.14 shows a map of the coefficient K_g as a function of the elastic modulus and thickness of the core and the thickness of a CFRP layer ($E_f = 60GPa$), analogously Figure 4.15 shows the values of K_g for a top face made of GFRP ($E_f = 20GPa$). Values from Figure 4.12 should be corrected with the value of K_g to get the effective maximum stress in the core.

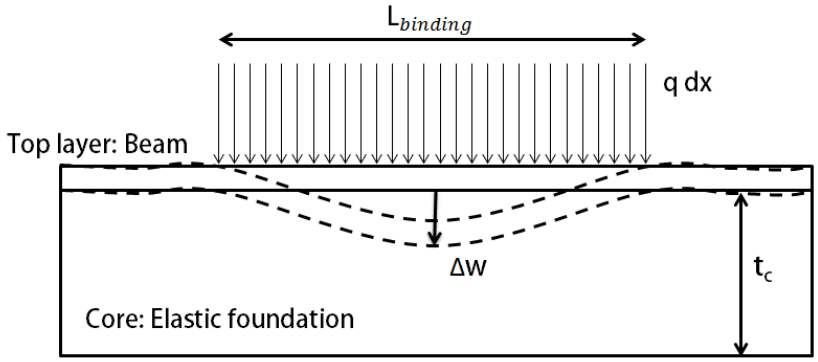

Figure 4.13: Elastic foundation model. The binding is transmitting a pressure to the upper layer (beam), which is bending on top of the core (elastic foundation)

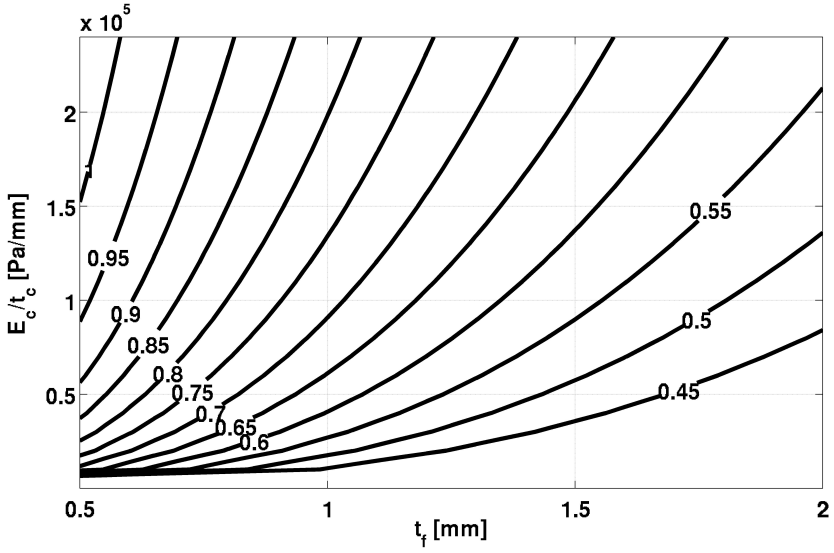

Figure 4.14: K_g coefficient for CFRP faces

It has to be noted that for a given entry velocity and radius of curvature, the maximum compressive stress in the core lowers as the core compressive elastic modulus lowers and as the face and core thickness and the elastic modulus of the faces increase.

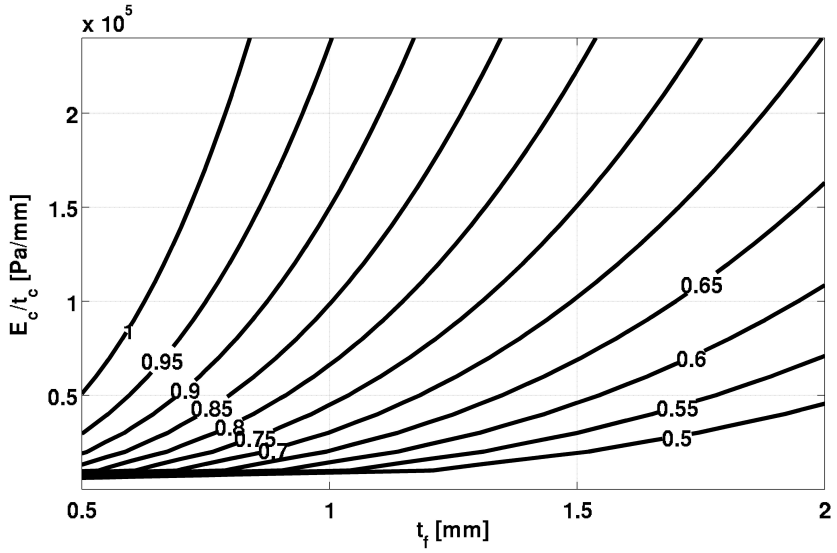

Figure 4.15: K_g coefficient for GFRP faces

Effect of the curvature on the maximum stresses

In this section the following approximations are assumed: the core elasticity modulus is much lower than the face elasticity modulus ($E_c << E_f$) and the faces thickness is much lower than the core thickness ($t_f << t_c$). This is justified by the fact that in the current design of wakeboards the faces are usually made of GFRP about 1 to 2 mm thick and a foam core between 20 and 40 mm thick. In this case, the stresses in the core and in the faces can be approximated as:

$$\sigma_c(z) = 0 \qquad \sigma_f(z) = \pm \frac{M_x}{t_f d} \tag{4.8}$$

$$\tau_c(z) = \frac{T_x}{d} \qquad \tau_f(z) = 0 \tag{4.9}$$

where z is the distance from the neutral axis, d is the distance between the two neutral axis of the faces, T_x and M_x are the shear force and the momentum in the longitudinal direction of the board.
The shear stiffness S is given by:

$$S = \frac{G_c d^2}{t_c} \tag{4.10}$$

and the flexural stiffness is approximated as:

$$D = \frac{E_f t_f d^2}{2} \tag{4.11}$$

Since the maximum change in curvature is known ($\frac{d^2w}{dx^2} = \frac{1}{R} - \frac{1}{\inf} = \frac{1}{R}$), using the simplified formula $\frac{d^2w}{dx^2} = \frac{M_x}{D} - \frac{1}{S}\frac{dT_x}{dx}$, on the hypothesis that there should be at least one point were $\frac{dT_x}{dx} = 0$ and combining it with eq. 4.8 and eq. 4.11, the maximum stress in the faces is given by:

$$\sigma_f = \pm\frac{E_f d}{2R} \tag{4.12}$$

while the shear stress in the core can be found under the hypothesis that the curvature change is entirely due to the shear component ($\frac{d^2w}{dx^2} = \frac{1}{R} = -\frac{1}{S}\frac{dT_x}{dx}$), thus:

$$\tau_c = \int_0^x \frac{1}{R} G_c dx \quad \rightarrow \quad \tau_{c_{max}} = \frac{l/2}{R} G_c \tag{4.13}$$

where l is the distance between the centreline of the two bindings. The shear stress in the core is zero at the middle of the board and is maximum at the location of the bindings.
From Eq. 4.12 and 4.13 it is evident that the thickness of the faces do not have any influence on the maximum shear stress in the core, while the core thickness is affecting the stress in the faces. In both cases the maximum stresses are inversely proportional to the radius of curvature: the maximum shear stress in the core increases with the curvature and the distance between the bindings, while the stress in the faces increases with the curvature and the core thickness.

Local buckling strength

Due to defects during the manufacturing process or by local damage caused by improper or hard use of the boards, local delaminations at the interface

between the faces and the core might happen. The delaminated zone could buckle while loaded on compression, causing a total collapse of the board. This section deals with a damage tolerance limit for the delamination length, this limit is defined as the maximum delamination allowed by the board and can be taken as an additional design variable.
The local buckling load of the delaminated face (considering a free/free boundary condition to underestimate the critical load) can be evaluated by Euler's formula:

$$F = \frac{\pi^2 E_f I}{L^2} \tag{4.14}$$

where L is the length of the delamination and $E_f I$ is the flexural stiffness of the beam.
Or, in terms of critical stresses, in order not to have buckling phenomena, the face compressive stress σ_f should be lower than:

$$\sigma_f \leq \frac{\pi^2 E_f}{L^2} t_f^2 \tag{4.15}$$

From eq. 4.12 we know that the maximum stress in the fibres is related to the radius of curvature and the core thickness. Substituting in eq. 4.15 we obtain:

$$\sigma_f = \frac{E_f d}{2R} \leq \frac{\pi^2 E_f}{L^2} t_f^2 \tag{4.16}$$

simplifying,

$$t_f^2 \geq \frac{d}{2R} \frac{L^2}{\pi^2} \tag{4.17}$$

For a given maximum acceptable delamination L (to be defined as a damage-tolerant parameter), the minimum face thickness t_f can be easily found as

function of the core thickness d and radius of curvature R, as shown in Figure 4.16.

Designer could think that fabricating the faces with a stronger material al-

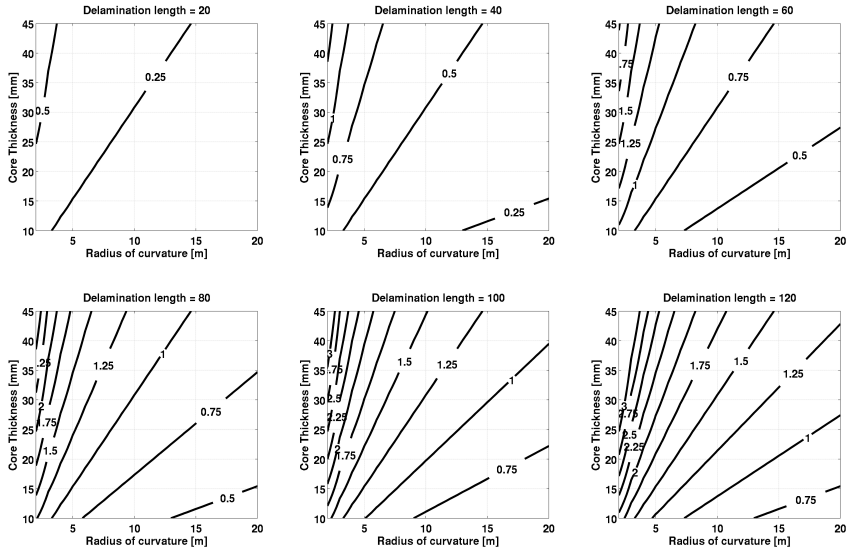

Figure 4.16: Minimum face thickness in function of: radius of curvature R, core thickness d and maximum acceptable delamination length L.

lows to reduce its thickness. This is not the case, since the minimum face thickness necessary to prevent buckling phenomena is not influenced by the elasticity modulus of the face but only by its thickness together with the radius of curvature of the board, the thickness of the core and the delamination length.

Wrinkling failure criteria

In case no delamination is present in the structure, the maximum compressive stress that can be sustained by the faces is limited by the critical wrinkling load, which can be evaluated as [167, 168]:

$$\sigma_c = 0.5\sqrt[3]{E_f E_c G_c} \tag{4.18}$$

For the materials currently used in wakeboards design the wrinkling stress is in the range of $120 \div 650\ MPa$. This means that the allowable compressive stress in the faces should always be lower than the wrinkling stress.
Combining equation 4.12 and 4.18 we obtain the maximum core thickness allowable to prevent wrinkling:

$$\frac{E_f d}{2R} < 0.5\sqrt[3]{E_f E_c G_c} \Longrightarrow t_c \approx d < R\sqrt[3]{\frac{E_c G_c}{E_f^2}} \tag{4.19}$$

Figure 4.17 shows the maximum core thickness that can be used for a given

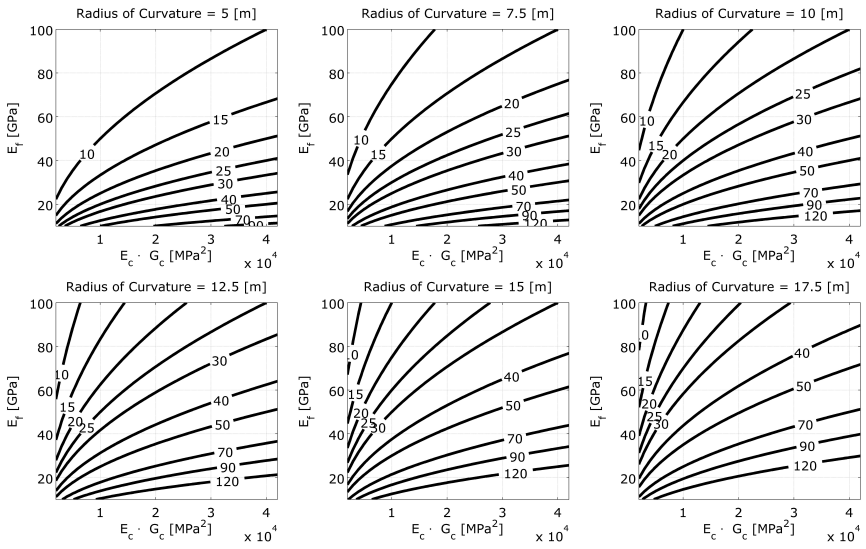

Figure 4.17: Maximum core thickness for a given radius of curvature varying the elastic properties of the faces (E_f) and of the core (E_c and G_c). Values are expressed in mm.

radius of curvature R and elastic properties of the faces and the core E_f, G_c and E_c. Using thicker cores than the one suggested in the graphs will cause a failure due to wrinkling as soon as the impact energy is sufficient to flatten the board. Note that the maximum allowable core thickness increases with the stiffness of the core material while it decreases with the stiffness of the

faces material.

1.6 Conclusions

In this work some practical formulas for the correct design of wakeboards are presented. These formulas were developed by the analysis of experimental results, numerical solutions and analytical formulations. The experimental results showed that the major damage mechanisms encountered in wakeboards are *(i)* core breakage and *(ii)* face wrinkling. The numerical simulations showed that the maximum deformation that could be reached by the board is the completely "flat" configuration, showing that the maximum stresses reached in the core and in the faces were strictly related to the maximum curvature of the undeformed board. Starting from these data, basing on the classical sandwich theory, some practical formulas were derived for the design of core and faces material strength and dimensions.
In particular, it was found that:

- The maximum compressive stress in the core increases with the square of the impact velocity and decreases with the curvature of the board.
- The mass of the user and the length of the board do not influence the maximum compressive stress in the core.
- The face thickness affects the maximum compressive stress in the core below the binding due to the impact force, since a thicker face better redistribute the load over the core.
- The maximum shear stress in the core increases with the curvature of the board and with the distance between the bindings.
- The maximum in-plane stresses in the faces increase with the curvature of the board and the elastic modulus of the faces material.
- If the core thickness increases, the compressive stress in the core (due to the maximum impact force) decreases, but it allows higher stresses in the faces.
- The face thickness has no influence on the onset of wrinkling phenomena, since it is influenced only by the board geometry (R and d) and by the elasticity modulus of the face. On the contrary the face minimum

thickness is limited by the local buckling phenomena that might appear due to local face/core delaminations.

- It is possible to design damage-tolerant boards where the structure is capable of withstanding a core/face delamination (whose extension is defined as a design parameter).

These considerations can be simplified into a practical table, as the one shown in Table 4.4, which shows the effect of the variation of each single parameter on the minimum strength of faces and core materials and its effect on wrinkling and buckling critical load.

Where σ_f is the minimum compressive strength of the laminated faces, σ_c is the minimum compressive strength of the core, τ_c is the minimum shear strength of the core. With the notation Wri and $Buck$ a positive (+) or negative (−) effect is denoted on the wrinkling and local buckling onset of the faces. In these two cases a positive (+) effect means that the variation of the parameter on interest (leaving all the other parameters constant) results in higher wrinkling (or buckling) load. Blank cells mean that there is no relative effect.

Table 4.4: Effect of each single parameter on the minimum required strength of faces and core materials.

	σ_f	σ_c	τ_c	Wri	$Buck$
$t_c \uparrow$	$\uparrow$	$\downarrow$		−	−
$t_f \uparrow$		$\downarrow$			+
$E_f \uparrow$	$\uparrow$	$\downarrow$		−	
$E_c \uparrow$		$\uparrow$		+	
$G_c \uparrow$			$\uparrow$	+	
$R \uparrow$	$\downarrow$	$\uparrow$	$\downarrow$	+	+

As example, the table shows that an increase ($\uparrow$) of the face thickness has a positive effect on the buckling critical load and on the core, since a material with lower ($\downarrow$) compressive strength σ_c is needed.

Conclusions

The thesis has focused on composite materials, with works where advancements were found covering the the aspects mentioned during the introduction as limiting the growth of applications where composite materials are used, these being: *(i)* The limited information regarding their properties and long term behaviour; *(ii)* The low technical development of production technologies; and *(iii)* The increased difficulty during the design design and production stages.

Although the different sections can be read independently, they are all interlaced by composite material design and testing; for example in chapter one a characterization method to simplify the correct definition of the curing kinetics of thermosetting resin was presented, this was used during the chapters focusing on manufacturing, and it is a great advance in order to optimize the production rate of composite materials with thermosetting matrix; the characterization of the impact of salty water on the mechanical properties of GFRP can be used for a better design of any product that would be utilized in this environment; and the manufacturing studies presented in chapter two and three many times include mechanical characterization of the resulting products.

In particular the studies presented were;

- The first study presented on the first chapter focus on the understanding of long term environmental effects on composite materials. An investigation included 3PB Quasi-Static, vibration and 3PB fatigue tests performed on GFRP with Polyester and Vinylester resin systems to understand the changes suffered by contact with salt water environment was presented. Specimens were made using the VARI process, which is studied in particular during the third chapter. GFRP and VARI are the material and technology most frequently used in mod-

ern marine applications. The behaviour was found to be symmetric for each resin, results showed a decrease in ultimate strength in the first month and then remained fairly constant. The decrease was about 6% for Glass/Vinylester and 7% for Glass/Polyester specimens. Vibration tests were used to obtain the evolution of the flexural modulus, where no change was detected. In the case of fatigue analysis, the tests were performed before and after the water exposure, and in both cases tests were done in wet and dry environments. The specimens tested in water showed better fatigue resistance, probably because of the improved heat transfer provided by water environment. There was no appreciable difference between fatigue response of aged specimens with respect to the untreated ones, for both matrix systems tested. The results show very good resistance of this kind of material towards seawater.

- In the second section of the first chapter, a method to simplify the calculations of the polymerization modelling of any thermosetting matrix materials is presented, although this is still a material characterization study, it could also be part of the manufacturing chapters, and in fact it the method was used later on when studying the manufacturing technology. In this section a simple procedure developed to obtain the parameters of Kamal-Souror model of cure kinetics has been explained, and applied to one particular epoxy resin as an example. The new approach uses an algebraic substitution which allows the construction of a relation between reaction orders m(T) and p(T) from experimental data. Knowing this relation it is possible to use a linear regression as the main instrument to fit the model, instead of the usual multiple regression approach well reported by other researchers. This method was used to characterize the curing of some components studied in chapter two and three.

- The first study of the second chapter tackled directly to one common problem of any product development: the long time-to-market; in this particular case focusing on a solution to the case where the product is made of composite materials with the autoclave curing of prepreg

technology. The solution was found combining rapid prototyping techniques to develop a method and material which allowed to obtain mould in a short time. In this work an indirect rapid tooling technique was used and tested in a parametric experimental test. The tooling material was a filled epoxy resin. Results were analysed using a 3D scanner and comparing the successive point clouds. It was possible to see how the filler allowed the mould to keep its geometrical integrity, producing good quality parts. The results show that moulds produced using this technique and high filler content can withstand several autoclave cycles without changing their shape, producing good quality parts. The method was protected with a patent and the tools are being commercialized nowadays by JUNO DESIGN under the RJM brand.

- The second study presented in chapter two recalls the curing analysis of thermosetting resins, and the ageing of pre-impregnated materials during the production stage. The work presented the analysis of two different prepregs that were intended to be used together for the production of a thick composite object. Both prepregs were produced by the same supplier and composed of the same resin precursor in the same fibre/resin ratio, but unexpectedly showed quite differently behaviour. However, one was a unidirectional material, while the other a twill fabric, the difference was not only the fibre arrangement, but also the prepreg production technique: the twill was obtained via solvent impregnation while the UD by hot melt procedure.
  The two materials showed a different ageing trend, with PP-UD almost invariant with time, while PP-T2, when stored at RT showed a tendency to slowly react, thus lowering with time the T_g values reached in the final composite object after curing. Though raw materials are still well within their shelf life, the differences observed for the two commercial prepregs suggest that a good practice should imply verification of actual attainable features of materials in the applied work up conditions in order to reach the best possible performance when designing a curing cycle for such a complex part as the one investigated in the study.

Indeed, this is particularly important when the final object to be cured is made up of a sequence of layers where the prepregs alternate, and not necessarily with a regular pattern. The discrepancy in the heat evolution might indeed induce stresses and overheating ending in affecting the final mechanical properties. This work showed that the experimental verification of raw materials and curing conditions, though it may sound costly and time-consuming, might help identifying unforeseen critical situations and avoid the lack of performance in the final composite materials.

- Chapter three deals with LCM production techniques, the first section regards VARI process and a problematic very common in industry when manufacturing processes are based LCM techniques: the study of the resin flow. Trial and error is still today the most used approach for the definition of injection strategies, but the interest towards the application of FE analysis for processing optimization is of growing attention. In order to perform a valid simulation there is a need to characterise the laminates and to obtain reliable permeability data. A procedure able to obtain characteristic values with few experimental procedures was presented and applied with success to the production of a ship runway. The procedure starts with a classic characterization at constant V_f and then the acquisition of data to construct a $Pressure - V_f$ curve. These data is then used together with an infusion test to correlate the last with a simulation and finally obtain the $K - V_f$ curve for each laminate. The industrial case study of a lightweight ship runaway was provided as a conducting line during the study, it had a zone made with a sandwich structure (with perforated core), this kind of structures are not directly implemented in PAM-RTM process simulation sofware, the section provided a way of dealing with sandwich structures where perforated cores are used.

- The second section of the third chapter went on with the study of another LCM process, it presented the case of a con-rod beam, a thick CFRP part which was produced using the RTM process. For both injec-

tion and curing, results of simulations performed with PAM-RTM were presented and compared to real experiences. It was found that the resin flow during injection could be rather unpredictable, probably because of the fibre rearrangement and race tracking effects. An asymmetric solution on a symmetric problem was obtained. This effect could be reproduced using the software by manually applying asymmetries that emulated the effects mentioned above. Results from the experience also showed the improvements in terms of aesthetic aspect and porosity of the part that could be achieved by applying an end compression of the resin by means of compressed air.

Regarding the curing of the part, the simulation of a 75 minutes curing cycle was presented, the results were corroborated by means of DSC measurements. This cycle was designed to obtain a quick curing without causing and excessive exothermy, which would decrease the mechanical properties of the final component.

Results of mechanical tests were also presented, performed on specimens produced by RTM and compared to others produced with the prepreg and autoclave method. In particular, the impact of a process enhancer product normally used in industry has been studied, showing that it can have a substantial influence on the mechanical performance of the resulting product. On other tests i.e. tensile, RTM components showed comparable results with Prepreg ones in terms of maximum load before failure, proving RTM as a high end process with medium scale output.

- The last chapter tackle the product design directly, with a work presenting some practical formulas for the correct design of wakeboards, a particular product made of composite materials used to perform wakeboard sport. The objective of this section was to provide an example of how composite products should be designed. The formulas presented were developed by the analysis of experimental results, numerical solutions and analytical formulations. Experimental tests were also performed, the results showed that the major damage mechanisms encountered in wakeboards are *(i)* core breakage and *(ii)* face wrinkling.

The numerical simulations showed that the maximum deformation that could be reached by the board is the completely "flat" configuration, showing that the maximum stresses reached in the core and in the faces were strictly related to the maximum curvature of the undeformed board. Starting from these data, basing on the classical sandwich theory, some practical formulas were derived for the design of core and faces material strength and dimensions.

In particular, it was found that:

- The maximum compressive stress in the core increases with the square of the impact velocity and decreases with the curvature of the board.
- The mass of the user and the length of the board do not influence the maximum compressive stress in the core.
- The face thickness affects the maximum compressive stress in the core below the binding due to the impact force, since a thicker face better redistribute the load over the core.
- The maximum shear stress in the core increases with the curvature of the board and with the distance between the bindings.
- The maximum in-plane stresses in the faces increase with the curvature of the board and the elastic modulus of the faces material.
- If the core thickness increases, the compressive stress in the core (due to the maximum impact force) decreases, but it allows higher stresses in the faces.
- The face thickness has no influence on the onset of wrinkling phenomena, since it is influenced only by the board geometry (R and d) and by the elasticity modulus of the face. On the contrary the face minimum thickness is limited by the local buckling phenomena that might appear due to local face/core delaminations.
- It is possible to design damage-tolerant boards where the structure is capable of withstanding a core/face delamination (whose extension is defined as a design parameter).

Further investigations should continue with the research on composite materials. Each of the sections presented con be further extended, either by going on with the characterization on other than seawater environments, obtaining the curing parameters of other thermosetting resins, or the permeability on other fabrics, or a method to obtain the permeability of a laminate from

the values of the composing layers, or investigating more product structures and defining design rules. For the time being composite materials have already shown high present and potential use among many different industries, helping on the design of much more efficient products, the research activities should help the continuous growth of the industry of these materials.
This work was performed during the past three years of PhD studies, in cooperation with many colleges from university, research centres and in close contact with the industry, which will be specially thanked in the acknowledgements. The close contact with companies gives the thesis an evident focus on end-application rather than basic research, whih were used as a step forward for the production of the presented work.

Acknowledgements

Chapert 1, Section 1: DURABILITY OF COMPOSITES
Special thanks to Andrea Zucchelli and Giangiacomo Minak, co-authors of the article derived from this work. Also thanks to Stilplast s.r.l. for providing the specimens and Mariner s.r.l. for the support, and thanks to Francesco Pirisi and Tommaso Brugo for their valuable help. Finally thanks to technicians Dino Balduzzi and Wanda Roversi for their patience during the experimental campaign.

Chapert 1, Section 2: CHARACTERIZATION OF THE CURE KINETICS OF A THERMOSETTING MATRIX
Special thanks to ELANTAS and RIBA composites for the information and support given during the current investigation.
This work was part of "Pro.Ma.Tec. (Processi e Materiali Innovativi Tecnologicamente Avanzati per la Meccanica)" project, which is funded by Regione Emilia Romagna within the funding program "Dai distretti produttivi ai distretti tecnologici" DGR n. 1631/2009.

Chapert 2, Section 1: CHARACTERIZATION OF THE CURE KINETICS OF A THERMOSETTING MATRIX
Tanks to Gian Luca Monti and Cristiano Fragassa for their help, Studio Pedrini s.r.l. (www.sp-design.it) for the support in the research and MetalTIG (www.metaltig.it) in the testing.

Chapter 2, Section 2: THICK COMPOSITES CURED IN AUTOCLAVE
Financial support from ProMaTec project of Emilia Romagna is gratefully acknowledged. Special thanks the staff of RI-BA Composites srl for providing the industrial facilities and raw materials, as well as for the helpful discussions and valuable support offered during the current investigation.

Chapter 3, Section 1: VACUUM ASSISTED RESIN INFUSION PROCESS

Thanks to Emmanuele Semprini and the personal of Ri-Ba s.r.l. for the help and support during the work.

Chapter 3, Section 2: RESIN TRANFER MOULDING PROCESS

Thanks to Esi-Group, ELANTAS, and the personal of RIBA composites for the information and support given during the current investigation.
This work is part of "Pro.Ma.Tec. (Processi e Materiali In-novativi Tecnologicamente Avanzati per la Meccanica)" project, that is funded by Regione Emilia Romagna within the funding program "Dai distretti produttivi ai distretti tecnologici" DGR n. 1631/2009.

Chapter 4: DESIGN OF COMPOSITE STRUCTURES

Special thanks to Riccardo Panciroli for the numerical analysis and the help during this work. Riccardo focus his research studies on the slamming on water of viscoelastic structures, his help was invaluable during the study of the wakeboard.

References

[1] Ghydaa Alawsi, Saud Aldajah, and Safa Abdul Rahmaan. Impact of humidity on the durability of E-glass/polymer composites. *Materials & Design*, 30(7):2506–2512, August 2009.

[2] a. Kootsookos and A.P. Mouritz. Seawater durability of glass- and carbon-polymer composites. *Composites Science and Technology*, 64(10-11):1503–1511, August 2004.

[3] E.P. Gellert and D.M. Turley. Seawater immersion ageing of glass-fibre reinforced polymer laminates for marine applications. *Composites Part A: Applied Science and Manufacturing*, 30(11):1259–1265, November 1999.

[4] Y. Miyano. Accelerated Testing for Long-term Durability of FRP Laminates for Marine Use. *Journal of Composite Materials*, 39(1):5–20, January 2005.

[5] P.C. Varelidis, N.P. Kominos, and C.D. Papaspyrides. Polyamide coated glass fabric in polyester resin: interlaminar shear strength versus moisture absorption studies. *Composites Part A: Applied Science and Manufacturing*, 29(12):1489–1499, December 1998.

[6] VM Karbhari. E-glass/vinylester composites in aqueous environments?I: experimental results. *Applied Composite Materials*, pages 19–48, 2003.

[7] G Kotsikos, J Evans, A Gibson, and J Hale. Environmentally enhanced fatigue damage in glass fibre reinforced composites characterised by acoustic emission. *Composites Part A: Applied Science and Manufacturing*, 31(9):969–977, September 2000.

[8] J.R. Correia, S Cabral-Fonseca, and FA Branco. Durability of pultruded glass-fiber-reinforced polyester profiles for structural applications. *Mechanics of Composite Materials*, 42(4):463–474, 2006.

[9] J. I. Cauich-Cupul, E. Pérez-Pacheco, A. Valadez-González, and P. J.

Herrera-Franco. Effect of moisture absorption on the micromechanical behavior of carbon fiber/epoxy matrix composites. *Journal of Materials Science*, 46(20):6664–6672, May 2011.

[10] Huang Gu. Dynamic mechanical analysis of the seawater treated glass/polyester composites. *Materials & Design*, 30(7):2774–2777, August 2009.

[11] E. C. Botelho, M. L. Costa, L. C. Pardini, and M. C. Rezende. Processing and hygrothermal effects on viscoelastic behavior of glass fiber/epoxy composites. *Journal of Materials Science*, 40(14):3615–3623, July 2005.

[12] M Shimbo, M Yamabe, K Kubomura, I Kimpara, H Kikukawa, M Nakada, Sugimori T Kunio, and S W Tsai. Long-Term Durability and Damage Tolerance of Innovative Marine Composites. *Materials System Research Laboratory*, 25, 2007.

[13] Ivo Černý and Rayner M. Mayer. Evaluation of static and fatigue strength of long fiber GRP composite material considering moisture effects. *Composite Structures*, 92(9):2035–2038, August 2010.

[14] G. Czel and T. Czigany. A Study of Water Absorption and Mechanical Properties of Glass Fiber/Polyester Composite Pipes – Effects of Specimen Geometry and Preparation. *Journal of Composite Materials*, 42(26):2815–2827, December 2008.

[15] Beckry Abdel-Magid, Saeed Ziaee, Katrina Gass, and Marcus Schneider. The combined effects of load, moisture and temperature on the properties of E-glass/epoxy composites. *Composite Structures*, 71(3-4):320–326, December 2005.

[16] Abdel-Hamid I. Mourad, Beckry Mohamed Abdel-Magid, Tamer El-Maaddawy, and Maryam E. Grami. Effect of Seawater and Warm Environment on Glass/Epoxy and Glass/Polyurethane Composites. *Applied Composite Materials*, 17(5):557–573, April 2010.

[17] a. Naceri. An analysis of moisture diffusion according to Fick?s law and the tensile mechanical behavior of a glass-fabric-reinforced composite. *Mechanics of Composite Materials*, 45(3):331–336, July 2009.

[18] Fernand Ellyin and Christof Rohrbacher. The Influence of Aqueous Environment, Temperature and Cyclic Loading on Glass-Fibre/Epoxy Composite Laminates. *Journal of Reinforced Plastics and Composites*,

22(7):615–636, May 2003.

[19] R Adams. The dynamic properties of fibre-reinforced polymers exposed to hot, wet conditions. *Composites Science and Technology*, 56(8):977–997, 1996.

[20] SK Rege. Effect of salt water on mechanical properties of fibre reinforced plastics. *Fibre Science and Technology*, 19:317–324, 1983.

[21] A.G. Dickson and C. Goyet. Chapter 5 - Physical and thermodinamic data. In *Handbook of methods for the analysis of the various parameters of the carbon dioxide system in sea water*. 1997.

[22] G. Minak, A. Zucchelli Damage evaluation and residual strength prediction of CFRP laminates by means of acoustic emission techniques. *In: Durand LP, editor. Composite Materials Research Progress. Nova Science Publishers*, pages 165–207, 2008.

[23] G. Minak, P. Morelli, A. Zucchelli Fatigue residual strength of circular laminate graphite?epoxy composite plates damaged by transverse load. *Composites Science and Technology*, 69(9):1358–1363, 2009.

[24] a.a. Bakhtiary Davijani, M. Hajikhani, and M. Ahmadi. Acoustic Emission based on sentry function to monitor the initiation of delamination in composite materials. *Materials & Design*, 32(5):3059–3065, May 2011.

[25] Physical Acoustic Corporation DiSP users manual. Rev 1, August 2000

[26] A Refahi Oskouei, A Zucchelli, M Ahmadi, and G Minak. An integrated approach based on acoustic emission and mechanical information to evaluate the delamination fracture toughness at mode I in composite laminate. *Materials and Design*, 32(3):1444–1455, 2011.

[27] C Maggana. Water sorption and diffusion studies in an epoxy resin system. *Journal of Polymer Science Part B:*, pages 7–11, 1999.

[28] Joannie W. Chin, Tinh Nguyen, and Khaled Aouadi. Sorption and diffusion of water, salt water, and concrete pore solution in composite matrices. *Journal of Applied Polymer Science*, 71(3):483–492, January 1999.

[29] I Merdas, F Thominette, A Tcharkhtchi, and J Verdu. Factors governing water absorption by composite matrices. *Composites Science and Technology*, 62(4):487–492, March 2002.

[30] N Godin, S Huguet, and R Gaertner. Influence of hydrolytic ageing on

the acoustic emission signatures of damage mechanisms occurring during tensile tests on a polyester composite: Application of a Kohonen?s map. *Composite Structures*, 72(1):79–85, January 2006.

[31] K Liao, C R Schultheisz, D L Hunston, and L C Brinson. THE EFFECT OF WATER ON THE FATIGUE BEHAVIOR FOR A PULTRUDED GLASS-REINFORCED COMPOSITE. *Plastics in Building Construction*, 23(5):7–12, 1999.

[32] a.M. Visco, N. Campo, and P. Cianciafara. Comparison of seawater absorption properties of thermoset resins based composites. *Composites Part A: Applied Science and Manufacturing*, 42(2):123–130, February 2011.

[33] E Botelho, L Pardini, and M Rezende. Hygrothermal effects on damping behavior of metal/glass fiber/epoxy hybrid composites. *Materials Science and Engineering: A*, 399(1-2):190–198, June 2005.

[34] ASTM International. ASTM Standard E739, 2010, "Standard Practice for Statistical Analysis of Linear or Linearized Stress-Life (S-N) and Strain-Life ('-N) Fatigue Data", 2010.

[35] L Toubal, M Karama, and B Lorrain. Damage evolution and infrared thermography in woven composite laminates under fatigue loading. *International Journal of Fatigue*, 28(12):1867–1872, December 2006.

[36] G. Minak. On the Determination of the Fatigue Life of Laminated Graphite-Epoxy Composite by Means of Temperature Measurement. *Journal of Composite Materials*, 44(14):1739–1752, January 2010.

[37] Gian Luca Monti, Ezequiel Poodts, Giangiacomo Minak, and Cristiano Fragassa. Pat. Pending Nr. PS2010A000026, 2010.

[38] Ana Pilipović, Pero Raos, and Mladen Šercer. Experimental analysis of properties of materials for rapid prototyping. *The International Journal of Advanced Manufacturing Technology*, 40(1-2):105–115, December 2007.

[39] Rupinder Singh. Process capability study of polyjet printing for plastic components. *Journal of Mechanical Science and Technology*, 25(4):1011–1015, June 2011.

[40] Blake J Driscoll. Rapid Manufacturing and the Global Economy. Technical report, 2008.

[41] José Carvalho Ferreira, Eduardo Santos, Hugo Madureira, and João Castro. Integration of VP/RP/RT/RE/RM for rapid product and process development. *Rapid Prototyping Journal*, 12(1):18–25, 2006.

[42] SK Mazumdar. *Composites manufacturing: materials, product, and process engineering*. CRC Pr I Llc, 2002.

[43] Vivek Patel. Composite Tooling : Trend, Applications and Market. *FRP Today*, 1(May):23–26, 2010.

[44] Joel W. Barlow, Joseph J. Beaman, and Badrinarayan Balasubramanian. A rapid mould-making system: material properties and design considerations. *Rapid Prototyping Journal*, 2(3):4–15, 1996.

[45] S Masood and W Song. Development of new metal/polymer materials for rapid tooling using Fused deposition modelling. *Materials & Design*, 25(7):587–594, October 2004.

[46] Pedro V. Vasconcelos, F. Jorge Lino, Antonio Magalhães, and Rui J.L. Neto. Impact Fracture Study of Filled Epoxy Resins. 2004.

[47] Pedro V Vasconcelos, F Jorge Lino, R J Neto, and Ricardo Paiva. DESIGN EPOXY RESINS BASED COMPOSITES FOR RAPID. In *5th international conference on mechanics and materials in design*, pages 1–7, 2006.

[48] S. Ma, I. Gibson, G. Balaji, and Q.J. Hu. Development of epoxy matrix composites for rapid tooling applications. *Journal of Materials Processing Technology*, 192-193:75–82, October 2007.

[49] Dilip Sahebrao Ingole, Abhay Madhusudan Kuthe, Shashank B. Thakare, and Amol S. Talankar. Rapid prototyping - a technology transfer approach for development of rapid tooling, *Rapid Prototyping Journal*, 15(4):280–290, 2009.

[50] H.S. Ong, C.K. Chua, and C.M. Cheah. Rapid Moulding Using Epoxy Tooling Resin. *The International Journal of Advanced Manufacturing Technology*, 20(5):368–374, September 2002.

[51] C.Y. Hsu, C.K. Huang, and G.J. Tzou. Using metallic resin and aluminum alloy molds to manufacture propellers with RP/RT technique. *Rapid Prototyping Journal*, 14(2):102–107, 2008.

[52] JS Colton and Y Park. Sheet metal forming using polymer composite rapid prototype tooling. *Journal of Engineering Materials and Technol-*

ogy, 125(July):247–255, 2003.

[53] G J Gibbons, J J Segui-Garza, and R G Hansell. Low-cost resin infusion mould tooling for carbon fibre composites manufacture. *Proceedings of the Institution of Mechanical Engineers, Part G: Journal of Aerospace Engineering*, 224(4):511–518, January 2010.

[54] Terry T. Wohlers. *Wohlers report 2006: rapid prototyping, tooling & manufacturing state of the indusrty : annual worldwide progress report.* 2006.

[55] P Vasconcelos, F Lino, A Baptista, and R Neto. Tribological behaviour of epoxy based composites for rapid tooling. *Wear*, 260(1-2):30–39, January 2006.

[56] Eugene Guth. Theory of Filler Reinforcement. *Journal of Applied Physics*, 16(1):20, 1945.

[57] S Fu, X Feng, B Lauke, and Y Mai. Effects of particle size, particle-matrix interface adhesion and particle loading on mechanical properties of particulate-polymer composites. *Composites Part B: Engineering*, 39(6):933–961, September 2008.

[58] C. P. Wong and Raja S. Bollampally. Thermal conductivity, elastic modulus, and coefficient of thermal expansion of polymer composites filled with ceramic particles for electronic packaging. *Journal of Applied Polymer Science*, 74(14):3396–3403, December 1999.

[59] Oleg Dmitriev and Sergey Mischenko. Optimization of Curing Cycles for Thick-wall Products of the Polymeric Composite Materials. In *Advances in Composite Materials - Ecodesign and Analysis*, pages 141–160. 2011.

[60] Thomas W. Secord, Susan C. Mantell, and Kim a. Stelson. Scaling Analysis and a Critical Thickness Criterion for Thermosetting Composites. *Journal of Manufacturing Science and Engineering*, 133(1):011005, 2011.

[61] Vincenza Antonucci, Michele Giordano, Kuang-Ting Hsiao, and Suresh G. Advani. A methodology to reduce thermal gradients due to the exothermic reactions in composites processing. *International Journal of Heat and Mass Transfer*, 45(8):1675–1684, April 2002.

[62] D. W. RADFORD. Cure shrinkage induced warpage in flat uni-axial composites. *Journal of composites technology & research*, 15(4):290–296,

1993.

[63] Yingfeng Yu, Huihuang Su, and Wenjun Gan. Effects of Storage Aging on the Properties of Epoxy Prepregs. *Industrial & Engineering Chemistry Research*, 48(9):4340–4345, May 2009.

[64] Luca Sorrentino and Luca Tersigni. A Method for Cure Process Design of Thick Composite Components Manufactured by Closed Die Technology. *Applied Composite Materials*, 19(1):31–45, November 2010.

[65] C. Demaria, Edu Ruiz, and F Trochu. In-plane anisotropic permeability characterization of deformed woven fabrics by unidirectional injection. Part II: Prediction model and numerical simulations. *Polymer Composites*, 28(6):812–827, 2007.

[66] CA Griffis and RA Masumura. Thermal response of graphite epoxy composite subjected to rapid heating. *Material Science and Technology Division*, 1981.

[67] Andrew Johnston, Reza Vaziri, and Anoush Poursartip. A Plane Strain Model for Process-Induced Deformationof Laminated Composite Structures. *Journal of Composite Materials*, 35(16):1435–1469, January 2001.

[68] Jin Zhang, Bronwyn Fox, and Qipeng Guo. Consistent model predictions for isothermal cure kinetics investigation of high performance epoxy prepregs. *Journal of applied polymer science*, 2008.

[69] C Dispenza and JT Carter. Cure behaviour of epoxy resin matrices for carbon fibre composites. *Polymer International*, 1236(July):1229–1236, 1999.

[70] Christopher M Sahagun and Sarah E Morgan. Thermal control of nanostructure and molecular network development in epoxy-amine thermosets. *ACS applied materials & interfaces*, 4(2):564–72, February 2012.

[71] Karin Peter, Eva Gerhard-Abozari, and Hartwig Höcker. Der einflußvon faseroberflächen auf die matrixhärtung bei faserverbundwerkstoffen. *Angewandte Makromolekulare Chemie*, 228(1):139–150, June 1995.

[72] JJ Antón, MM Pradas, and JL Ribelles. The effect of kevlar fiber reinforcement on the curing, thermal, and dynamic-mechanical properties of an epoxy/anhydride system. *Polymer Engineering and Science*, 40(8):1725–1735, 2000.

[73] Jovan Mijović. Cure kinetics of neat versus reinforced epoxies. *Journal of Applied Polymer Science*, 31(5):1177–1187, April 1986.

[74] Jovan Mijović and H. T. Wang. Cure kinetics of neat and graphite-fiber-reinforced epoxy formulations. *Journal of Applied Polymer Science*, 37(9):2661–2673, May 1989.

[75] John M. Barton. The application of differential scanning calorimetry (DSC) to the study of epoxy resin curing reactions. *Advances in Polymer Science*, 72:111–154, 1985.

[76] Camille Alzina, Nicolas Sbirrazzuoli, and Alice Mija. Hybrid nanocomposites: advanced nonlinear method for calculating key kinetic parameters of complex cure kinetics. *The journal of physical chemistry. B*, 114(39):12480–7, October 2010.

[77] Kuang-Ting Hsiao, Rex Little, Omar Restrepo, and Bob Minaie. A study of direct cure kinetics characterization during liquid composite molding. *Composites Part A: Applied Science and Manufacturing*, 37(6):925–933, June 2006.

[78] SC Joshi, XL Liu, and YC Lam. A numerical approach to the modeling of polymer curing in fibre-reinforced composites. *Composites science and technology*, 59:1003–1013, 1999.

[79] Travis A. Bogetti and John W. Gillespie. Two-Dimensional Cure Simulation of Thick Thermosetting Composites. *Journal of Composite Materials*, 25(3):239–273, March 1991.

[80] K. Horie, H. Hiura, M. Sawada, I. Mita, and H. Kambe. Calorimetric investigation of polymerization reactions. III. Curing reaction of epoxides with amines. *Journal of Polymer Science Part A-1: Polymer Chemistry*, 8(6):1357–1372, June 1970.

[81] F.X. Perrin, Thi Minh Hanh Nguyen, and J.L. Vernet. Chemico-diffusion kinetics and TTT cure diagrams of DGEBA-DGEBF/amine resins cured with phenol catalysts. *European Polymer Journal*, 43(12):5107–5120, December 2007.

[82] LM Lopez. Modeling the vulcanization reaction of silicone rubber. *Polymer Engineering & Science*, 47(5):675–683, 2007.

[83] P.K. Mallick. *Fiber-Reinforced Composites: Materials, Manufacturing, and Design, Third Edition (Dekker Mechanical Engineering)*. CRC

Press, 2007.

[84] Sergey Vyazovkin, Alan K. Burnham, José M. Criado, Luis a. Pérez-Maqueda, Crisan Popescu, and Nicolas Sbirrazzuoli. ICTAC Kinetics Committee recommendations for performing kinetic computations on thermal analysis data. *Thermochimica Acta*, 520(1-2):1–19, June 2011.

[85] M Opalicki, J M Kenny, and L Nicolais. Cure Kinetics of Neat and Carbon-Fiber-Reinforced TCDDM/DDS Epoxy Systems. *Journal of Applied Polymer Science*, 61(6):1025–1037, 1998.

[86] François Trochu, Edu Ruiz, Vincent Achim, and Sofiane Soukane. Advanced numerical simulation of liquid composite molding for process analysis and optimization. *Composites Part A: Applied Science and Manufacturing*, 37(6):890–902, June 2006.

[87] W.D Brouwer, E.C.F.C van Herpt, and M Labordus. Vacuum injection moulding for large structural applications. *Composites Part A: Applied Science and Manufacturing*, 34(6):551–558, June 2003.

[88] Bekir Yenilmez and E. Murat Sozer. Compaction of e-glass fabric preforms in the Vacuum Infusion Process, A: Characterization experiments. *Composites Part A: Applied Science and Manufacturing*, 40(4):499–510, April 2009.

[89] C Williams, J Summerscales, and S Grove. Resin infusion under flexible tooling (RIFT): a review. *Composites Part A: Applied Science and Manufacturing*, 27A:517–524, 1996.

[90] G. Gardiner. The evolution of infusion. *Composites World*, 2012.

[91] Q. Govignon, S. Bickerton, J. Morris, and P.a. Kelly. Full field monitoring of the resin flow and laminate properties during the resin infusion process. *Composites Part A: Applied Science and Manufacturing*, 39(9):1412–1426, September 2008.

[92] a. Hammami and B. R. Gebart. Analysis of the vacuum infusion molding process. *Polymer Composites*, 21(1):28–40, February 2000.

[93] CL Lee and KH Wei. Effect of material and process variables on the performance of resin-transfer-molded epoxy fabric composites. *Journal of Applied Polymer Science*, 77:2149–2155, 2000.

[94] Xiudong Sun, Shoujie Li, and L. James Lee. Mold filling analysis in vacuum-assisted resin transfer molding. Part I: SCRIMP based on a

high-permeable medium. *Polymer Composites*, 19(6):807–817, December 1998.

[95] Ali Gokce, Mourad Chohra, Suresh G. Advani, and Shawn M. Walsh. Permeability estimation algorithm to simultaneously characterize the distribution media and the fabric preform in vacuum assisted resin transfer molding process. *Composites Science and Technology*, 65(14):2129–2139, November 2005.

[96] C. Demaria, Edu Ruiz, and F Trochu. In-plane anisotropic permeability characterization of deformed woven fabrics by unidirectional injection. Part II: Prediction model and numerical simulations. *Polymer Composites*, 28(6):812–827, 2007.

[97] N.C. Correia, F. Robitaille, A.C. Long, C.D. Rudd, P. Šimáček, and S.G. Advani. Analysis of the vacuum infusion moulding process: I. Analytical formulation. *Composites Part A: Applied Science and Manufacturing*, 36(12):1645–1656, December 2005.

[98] ESI-Group International Ltd. PAM-RTM 2010 User's Guide & tutorials, 2010.

[99] S. Drapier, J. Monatte, O. Elbouazzaoui, and P. Henrat. Characterization of transient through-thickness permeabilities of Non Crimp New Concept (NC2) multiaxial fabrics. *Composites Part A: Applied Science and Manufacturing*, 36(7):877–892, July 2005.

[100] M.V. Hosur, M. Abdullah, and S. Jeelani. Manufacturing and low-velocity impact characterization of hollow integrated core sandwich composites with hybrid face sheets. *Composite Structures*, 65(1):103–115, July 2004.

[101] Y. Ma and R. Shishoo. Permeability Characterization of Different Architectural Fabrics. *Journal of Composite Materials*, 33(8):729–750, April 1999.

[102] M. Nordlund. Numerical Study of the Local Permeability of Noncrimp Fabrics. *Journal of Composite Materials*, 39(10):929–947, May 2005.

[103] TS Lundström and R Stenberg. In-plane permeability measurements: a nordic round-robin study. *Composites Part A: Applied Science and Manufacturing*, 31:29–43, 2000.

[104] Richard S. Parnas, Kathleen M. Flynn, and Mary E. Dal-Favero. A per-

meability database for composites manufacturing. *Polymer Composites*, (9):623–633, 1997.

[105] M. Um and S. Lee. A study on the determination of in-plane permeability of fiber preforms. *Polymer composites*, 20(6), 1999.

[106] Pierre Ferland and D Guittard. Concurrent methods for permeability measurement in resin transfer molding. *Polymer composites*, 17(1):149–158, 1996.

[107] JR Weitzenböck, RA Shenoi, and PA Wilson. Radial flow permeability measurement. Part A: Theory. *Composites Part A: Applied Science and Manufacturing*, 30:781–796, 1999.

[108] JR Weitzenböck, RA Shenoi, and PA Wilson. Radial flow permeability measurement. Part B: application. *Composites Part A: Applied Science and Manufacturing*, 30:797–813, 1999.

[109] R Gauvin, F Trochu, Y Lemenn and L Diallo Permeability Measurement and Flow Simulation. *Polymer Composites*, 17(1), 34-42, 1996.

[110] Q Liu, RS Parnas and HS Giffard New set-up for in-plane permeability measurement. *Composites Part A: Applied Science and Manufacturing*, 38(3), 954-962, 2007.

[111] C. Demaria, Edu Ruiz, and F Trochu. In-plane anisotropic permeability characterization of deformed woven fabrics by unidirectional injection. Part I: Experimental results. *Polymer Composites*, 28(6):797–811, 2007.

[112] JR Weitzenböck, RA Shenoi, and PA Wilson. Measurement of three-dimensional permeability. *Composites Part A: Applied Science and Manufacturing*, 29(1-2):159–169, 1998.

[113] Laurent Joubaud, Vincent Achim, and François Trochu. Numerical simulation of resin infusion and reinforcement consolidation under flexible cover. *Polymer Composites*, 26(4):417–427, August 2005.

[114] D Yuexin, T Zhaoyuan, Z Yan and S Jing Compression Responses of Preform in Vacuum Infusion Process. *Chinese Journal of Aeronautics*, 21(4), 370-377, 2008.

[115] S Aranda, F Klunker, and G Ziegmann. COMPACTION RESPONSE OF FIBRE REINFORCEMENTS DEPENDING ON PROCESSING TEMPERATURE. ICCM 17 - 17th International Conference on Composite Materials, 2009.

[116] H M Andersson, T S Lundstrom, B R Gebaki, and P S Y Ergren. To Measure Thickness Variations in the Vacuum Infusion Process. *Polymer Composites*, 24(3):448–455, 2003.

[117] Andrew George Optimization of Resin Infusion Processing for Composite Materials: Simulation and Characterization Strategies. *Institute of Aircraft Design, University of Stuttgart*, 2011.

[118] AC Loos, BW Grimsley, RJ Cano, and Pascal Hubert. VARTM Processing of Tailored Composite Structures for Aerospace Applications. *SAMPE 2005, Long Beach, USA, May 1*, 2005.

[119] Y.-T. Jhan, Y.-J. Lee, and C.-H. Chung. Experimental and numerical investigation of the VARTM process with a sandwich structure. *Journal of Composite Materials*, 46(12):1417–1430, September 2011.

[120] Jun Ni, Shoujie Li, Xiudong Sun, and L. James Lee. Mold filling analysis in vacuum-assisted resin transfer molding. Part II: SCRIMP based on grooves. *Polymer Composites*, 19(6):818–829, December 1998.

[121] Vincent Achim and Edu Ruiz. Guiding selection for reduced process development time in RTM. *International Journal of Material Forming*, 3(S2):1277–1286, August 2009.

[122] D. Abraham, S. Matthews, and R. McIlhagger. A comparison of physical properties of glass fibre epoxy composites produced by wet lay-up with autoclave consolidation and resin transfer moulding. *Composites Part A: Applied Science and Manufacturing*, 29(7):795–801, July 1998.

[123] Y. Mahadik and S.R. Hallett. Finite element modelling of tow geometry in 3D woven fabrics. *Composites Part A: Applied Science and Manufacturing*, 41(9):1192–1200, September 2010.

[124] Shunliang Jiang, Chuck Zhang, and Ben Wang. Optimum arrangement of gate and vent locations for RTM process design using a mesh distance-based approach. *Composites Part A: Applied Science and Manufacturing*, 33(4):471–481, April 2002.

[125] C. Demaria, Edu Ruiz, and F Trochu. In-plane anisotropic permeability characterization of deformed woven fabrics by unidirectional injection. Part II: Prediction model and numerical simulations. *Polymer Composites*, 28(6):812–827, 2007.

[126] Pierre Ferland and D Guittard. Concurrent methods for permeability

measurement in resin transfer molding. *Polymer composites*, 17(1):149–158, 1996.

[127] I Verpoest and S Lomov. Virtual textile composites software : Integration with micro-mechanical, permeability and structural analysis. *Composites Science and Technology*, 65(15-16):2563–2574, December 2005.

[128] JR Weitzenböck, RA Shenoi, and PA Wilson. Radial flow permeability measurement. Part A: Theory. *... Part A: Applied Science and ...*, 30:781–796, 1999.

[129] JR Weitzenböck, RA Shenoi, and PA Wilson. Radial flow permeability measurement. Part B: application. *... Part A: Applied Science and ...*, 30:797–813, 1999.

[130] Qiang Liu, Richard S. Parnas, and Hermione S. Giffard. New set-up for in-plane permeability measurement. *Composites Part A: Applied Science and Manufacturing*, 38(3):954–962, March 2007.

[131] JR Weitzenböck, RA Shenoi, and PA Wilson. Measurement of three-dimensional permeability. *Composites Part A: Applied Science and Manufacturing*, 29(1-2):159–169, 1998.

[132] T. Stöven, F. Weyrauch, P. Mitschang, and M. Neitzel. Continuous monitoring of three-dimensional resin flow through a fibre preform. *Composites Part A: Applied Science and Manufacturing*, 34(6):475–480, June 2003.

[133] Junying Yang, Yuxi Jia, Yanyu Ding, and Haidong He. Edge effect in RTM processes under constant pressure injection conditions. *Journal ofAppliedPolymer Science*, 118:1014–1019, 2010.

[134] Mathieu Devillard, Kuang-Ting Hsiao, and Suresh G. Advani. Flow sensing and control strategies to address race-tracking disturbances in resin transfer molding-part II: automation and validation. *Composites Part A: Applied Science and Manufacturing*, 36(11):1581–1589, November 2005.

[135] C. Demaria, Edu Ruiz, and F Trochu. In-plane anisotropic permeability characterization of deformed woven fabrics by unidirectional injection. Part I: Experimental results. *Polymer Composites*, 28(6):797–811, 2007.

[136] S.R. White and Y.K. Kim. Staged curing of composite materials. *Composites Part A: Applied Science and Manufacturing*, 27(3):219–227, Jan-

uary 1996.

[137] M. R. Kamal and S. Sourour. Kinetics and thermal characterization of thermoset cure. *Polymer Engineering and Science*, 13(1):59–64, January 1973.

[138] CA Griffis and RA Masumura. Thermal response of graphite epoxy composite subjected to rapid heating. *Material Science and Technology Division*, 1981.

[139] ASTM. ASTM D-2344 Standard Test Method for Short-Beam Strength of Polymer Matrix Composite Materials, 2006.

[140] Shigehiro Kawai, H Otani, and Toshiyuki Sakata. Coupled Motion of Ski and Elastic Foundation Under Ski Control. *JSME Int Journal. Ser C. Mech Systems, Mach Elem Manuf*, 46(2):614–621, 2003.

[141] Kenji Hosokawa, Shigehiro Kawai, and Toshiyuki Sakata. Improvement of damping property of skis. *Sports Engineering*, 5(2):107–112, May 2002.

[142] Keith W. Buffinton, Steven B. Shooter, Ira J. Thorpe, and Jason J. Krywicki. Laboratory, computational and field studies of snowboard dynamics. *Sports Engineering*, 6(3):129–137, September 2003.

[143] S. M. Brennan, L. P. Kollár, and G. S. Springer. Modelling the mechanical characteristics and on-snow performance of snowboards. *Sports Engineering*, 6(4):193–206, December 2003.

[144] N. Scott, T. Yoneyama, H. Kagawa, and K. Osada. Measurement of ski snow-pressure profiles. *Sports Engineering*, 10(3):145–156, September 2007.

[145] N. Tada and Y. Hirano. In search of the mechanics of a turning alpine ski using snow cutting force measurements. *Sports Engineering*, 5(1):15–22, February 2002.

[146] N. Tada and Y. Hirano. In search of the mechanics of a turning alpine ski using snow cutting force measurements. *Sports Engineering*, 5(1):15–22, February 2002.

[147] R. Panciroli, S. Abrate, G. Minak, and A. Zucchelli. hydroelasticity in Water-entry Problems: Comparison between Experimental and SPH Results. *Composite Structures*, 94(2):532–539, August 2011.

[148] Odd M. Faltinsen. Hydroelastic slamming. *Journal of Marine Science*

and Technology, 5(2):49–65, January 2001.

[149] Z Qin and R.C. Batra. Local slamming impact of sandwich composite hulls. *International Journal of Solids and Structures*, 46(10):2011–2035, 2011.

[150] X Chen, Y Wu, W Cui, and J Jensen. Review of hydroelasticity theories for global response of marine structures. *Ocean Engineering*, 33(3-4):439–457, March 2006.

[151] Kevin J. Maki, Donghee Lee, Armin W. Troesch, and Nickolas Vlahopoulos. Hydroelastic impact of a wedge-shaped body. *Ocean Engineering*, 38(4):621–629, March 2011.

[152] Ivan Stenius. Finite Element Modelling of Hydroelasticity in Hull-Water Impacts. 2006.

[153] Kaushik Das and Romesh C. Batra. Local water slamming impact on sandwich composite hulls. *Journal of Fluids and Structures*, 27(4):523–551, May 2011.

[154] B Peseux, L Gornet, and B Donguy. Hydrodynamic impact: Numerical and experimental investigations. *Journal of Fluids and Structures*, 21(3):277–303, November 2005.

[155] A Iafrati and A. Korobkin. Hydrodynamic loads during early stage of flat plate impact onto water surface. *Physics of Fluids*, 20(8):082104, 2008.

[156] G Yupu, Z Zhenhua, C Wei, and G Deping. Foreign Object Damage to Fan Rotor Blades of Aeroengine Part II: Numerical Simulation of Bird Impact. *Chinese Journal of Aeronautics*, 21(4):328–334, August 2008.

[157] John Brett. Numerical modeling of shock wave and pressure pulse generation by underwater explosion. Technical report, Department of Defence, 1998.

[158] M.B. Liu, G.R. Liu, and K.Y. Lam. Investigations into water mitigation using a meshless particle method. *Shock Waves*, 12(3):181–195, November 2002.

[159] Justin Stephens. The Truth, 2009.

[160] TH Von Karman. The impact on seaplane floats, during landing. *NACA-TN-321*, 1929.

[161] Serge Abrate. Dynamics of impact on composite structures. *Key En-*

gineering Materials, 141-1432(Pt 2):671–694, 1998.

[162] D Zenkert. Static indentation and unloading response of sandwich beams. *Composites Part B: Engineering*, 35(6-8):511–522, December 2004.

[163] Shaw M Lee and Thomas K Tsotsis. Indentation failure behavior of honeycomb sandwich panels. *Composites Science and Technology*, 60(January):1147–1159, 2000.

[164] Mijia Yang, Pizhong Qiao, and F Asce. Quasi-Static Indentation Behavior of Honeycomb Sandwich Materials and Its Application in Impact Simulations. *October*, (October), 2008.

[165] M Saadati and M Sadighi. Indentation in lightweight composite sandwich beams. *Proceedings of the Institution of Mechanical Engineers, Part G: Journal of Aerospace Engineering*, 223(6):825–835, September 2009.

[166] Stephen P. Timoshenko. Strength of materials : advanced theory and problems. March 1941.

[167] M. Mahendran and D. McAndrew. Flexural Wrinkling Strength of Lightly Profiled Sandwich Panels with Transverse Joints in the Foam Core. *Advances in Structural Engineering*, 6(4):325–337, October 2003.

[168] N Pokharel. *Behaviour and Design of Sandwich Panels Subject to Local Buckling and Flexural Wrinkling Effects*. PhD thesis, Queensland University of Technology, 2003.


KOHLENIA
MATERIALES COMPUESTOS